Radio Frequency Tomography Based Electromagnetic Inverse Scattering For Reinforced Concrete Structures

BY

TADAHIRO NEGISHI
B.Sc. Nippon Institute of Technology, Japan, 2007
M.Sc. University of Illinois at Chicago, USA, 2011

THESIS

Submitted as partial fulfillment of the requirements
for the degree of Doctor of Philosophy in Electrical and Computer Engineering
in the Graduate College of the
University of Illinois at Chicago, 2018

Chicago, Illinois

Defense Committee:

Danilo Erricolo, Chair and Advisor
Piergiorgio L. E. Uslenghi
Wolfgang-Martin Boerner
Farhad Ansari, Civil and Materials Engineering
Hiroaki Miyashita, Mitsubishi Electric Corporation
Francesco Soldovieri, IREA-CNR
Michael C. Wicks, University of Dayton Research Institute

親愛なる私の家族と友人たちへ

ACKNOWLEDGMENTS

I would like to express my gratitude to my academic father, Prof. Erricolo. I am deeply grateful for him guiding me on research activities and introducing me to all experts in my Ph.D. study. I also appreciate that he has found the opportunity to interact with people in the industry to extend connections to those experts. I feel honored to have all the members of my defense committee who recognize me as a Ph.D scholar and sincerely thank them for their efforts. I am also proud of being the coauthor in many articles with Dr. Vittorio Picco, Dr. Gianluca Gennarelli, Dr. Lorenzo Lo Monte, Prof. Natasha Devroye, Dr. Pawan Setlur, Dr. Giorgio Carluccio and Dr. Matteo Albani. The collaborated works with those experts are priceless treasures that I will carry with me for the rest of my life.

I am indebted and thankful to all the staff members of the ECE department for having their academic and financial support. I would also like to thank my lab mates and the undergraduate research assistants. Finally, I must share news with my great mentors in Japan, Dr. Yasuo Watanabe, Mr. Masao Nakajima and Dr. Tatsuo Nakajima who gave advice and support to get me into the Ph.D study and I express sincere gratitude to Dr. Wolfgang-Martin Boerner who motivated me to complete the study.

TN

CONTRIBUTION OF AUTHORS

Contents in chapter 4 contains a similar analysis as in the Ph.D thesis of Dr. Vittorio Picco (1), and articles (2; 3; 4; 5) when all analyses are performed in a homogeneous background medium. New material is the extension of the studies for a reinforced concrete structures by using the analytical solution of a dielectric cylinder.

Experimental results shown in Chapter 5 are partially published in (6). Prof. Danilo Erricolo is my adviser and lead investigator. I was responsible for conducting many of the ideas such as preforming the experiments, analyzing the data and producing the reconstructed results. Dr. Vittorio Picco and Ms. Yangqing Liu assisted in performing the experiments and analysis of the data, as well as Prof. Danilo Erricolo, Dr. Gianlcuca Gennarelli, Dr. Francesco Soldovieri and Prof. Piergiorgio L.E. Uslenghi. I produced the reconstructed images used in the conference article. The RF Tomography measuring system was initially built by Dr. Vittorio Picco (1). I upgraded the system to the use of a wooden box.

TABLE OF CONTENTS

TABLE OF CONTENTS (Continued)

CHAPTER **PAGE**

LIST OF TABLES

LIST OF FIGURES

LIST OF FIGURES (Continued)

FIGURE **PAGE**

LIST OF FIGURES (Continued)

FIGURE **PAGE**

LIST OF FIGURES (Continued)

FIGURE **PAGE**

LIST OF FIGURES (Continued)

FIGURE **PAGE**

LIST OF ABBREVIATIONS

AWGN	Additive White Gaussian Noise
ART	Algebraic Reconstruction Technique
CG	Conjugate Gradient
DoI	Domain of Investigation
GPR	Ground Penetrating Radar
PEC	Perfect electric conductor
PSF	Point Spread Function
RF	Radio Frequency
RX	Receiving antenna
SAR	Synthetic Aperture Radar
SNR	Signal to Noise Ratio
TSVD	Truncated Singular Value Decomposition
TX	Transmitting antenna
UIC	University of Illinois at Chicago

SUMMARY

Radio Frequency (RF) Tomography is proposed to inspect reinforced concrete structures by providing tomographic images of the internal structure. Radio Frequency Tomography has been studied for underground imaging, in particular deeply buried objects such as tunnels or underground facilities. RF Tomography utilizes multi-static measurements which are processed to obtain images of complex dielectric permittivity distribution. RF Tomography is known to have advantages on resolution by use of spatial diversity of sensors contrary to limitation of mono-static configuration which has nominal range resolution criteria and bandwidth. Also, the forward models of RF Tomography are based on volume integral equations that are derived from Maxwell's equations, which leads to the possibility to obtain unique information on material property.

Ground Penetrating Radar is widely used to examine the structural health of reinforced concrete structure. This thesis aims to convince one to utilize RF Tomography as inspection and rehabilitation program for reinforced concrete structure. During the discussion, resolution analysis and tomographic examples are provided to show the advantages of RF Tomography.

RF Tomography is well studied for simple choices of background medium such as freespace and half-space medium. In order to extend the idea of RF Tomography to reinforced concrete structure, effect of bounded medium must be considered. A forward model for a circular dielectric cylinder is constructed as a numerical example of the supporting pillar structure of a

bridge. The forward model uses Born approximation, however the scatter field and propagation due to the dielectric cylinder are included in the forward model.

In the chapter on resolution analysis, this thesis focuses on studying achievable resolutions of mono-static and multi-static configurations. In order to achieve the purpose, the level of complexity was reduced in the analysis. A scattered field is found from forward calculation of the forward model instead of actual electromagnetic scattered field. This consideration allow us to analyze only ill-conditioning and achievable resolution of a system matrix. The analysis uses L-curve to determine optimum regularization parameter for Truncated Singular Value Decomposition (TSVD) scheme, and the optimum regularization parameter is used to provide resolution analysis of point spread function (PSF) and Spectral Content.

The Chapter on tomographic reconstruction demonstrates the reconstruction of images by RF Tomography. Scattered fields are provided by the Method of Moment numerically and measured experimentally in the Andrew Electromagnetics Laboratory, University of Illinois at Chicago. Tomographic reconstructions of mono-static and multi-static configurations are compared to confirm that multi-static configurations have the advantage on image quality. In addition to TSVD, iterative regularization methods such as Conjugate Gradient method (CG) and Algebraic Reconstruction Technique (ART) are used. The iterative regularization methods allow us to introduce constraints during the inversion process, which ensure the physical meaning of the permittivity.

CHAPTER 1

INTRODUCTION

Structurally deficient bridges are a cause for concern nowadays. In fact, The Federal Highway Administration, a subdivision of the U.S. Department of Transportation, has reported a vast amount of structurally deficient bridges (8). The concern of a bridge becoming structurally deficient starts to arise approximately 30 years after it was built. Normally once a bridge reaches the age of 30, continuous monitoring is required. In practice, civil engineers must evaluate the inspection of a bridge to determine any possible risk, depending on the degree, if any, they will decide how to reinforce or rehabilitate the bridge. There are many techniques used to evaluate the structural health of a bridge. Each technique has its advantages and disadvantages, thus civil engineers choose a technique depending on the situation. A regular routine for a bridge inspection starts with a visual inspection. After simple inspections, they assign appropriate techniques for more detailed inspections. These inspections include acoustic and radar imaging techniques, which play an important role when investigating the internal structure of a bridge and to localize hollow cavities or cracks. RF Tomography is an advanced radar imaging technique, which will enhance the accuracy and the resolution of a reinforced concrete structures internal image by using multi-static measurements. To make the best decision on the priority of a rehabilitation program, the development of precise diagnostic tools is very important.

In the U.S., many bridges were constructed during the 1960's. During the 1980's the U.S. started to encounter the risks and devastation that is caused by a structurally deficient bridge.

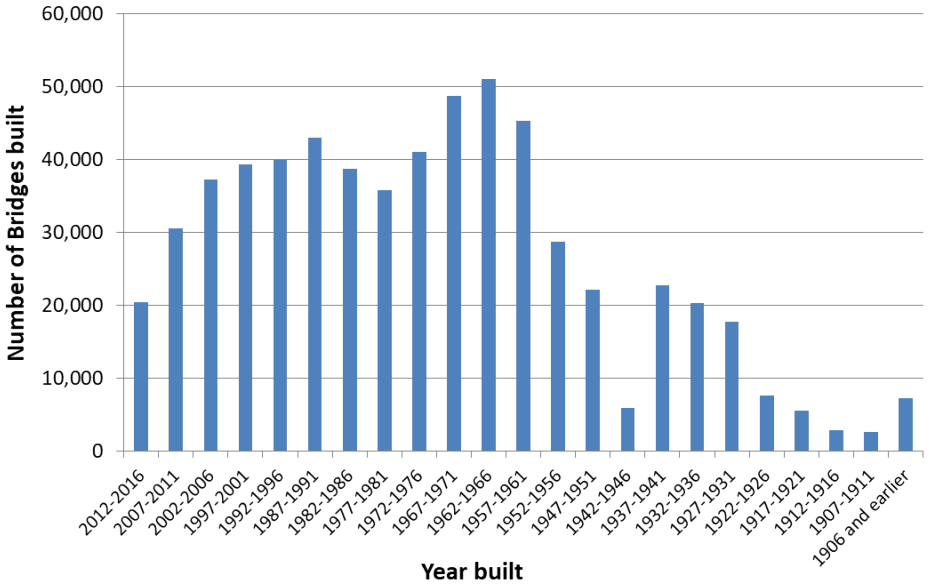

Figure 1: Number of bridges built by year, produced from the roport of the U.S. Department of Transportation, The Federal Highway Administration (7).

For example, the Mianus River Bridge was opened in 1958 and collapsed in 1983 (9). This accident was caused by the undetected displacement of a bearing pin, and corrosion due to an excessive amount of force on the bridge hangers. This accident gave the incentive for the govenment to start evaluating bridges for rehabilitation programs. The number of bridges built over the years in the U.S. is summarized in Figure 1 (7). You may notice that there are a large number of bridges that were built during the 1960's and the 1990's. Therefore, it is straight forward to realize that the current decade around 2020 is potentially at risk of accidents due to structurally deficient bridges. In fact, there are a number of reports in recent years such as the

collapse of the I-35W Mississippi River bridge in 2007 (10) and the collapse of the Brooklyn Bridge in 2014 (11).

The corrosion of reinforcing bars (rebar) caused the accident in the collapse of the Brooklyn Bridge (11). That accident became big news since five pedestrians were injured by pieces of concrete which fell from the bridge; and there have been similar accidents. The report on the Brooklyn Bridge accident states that falling pieces of concrete were detached due to corrosion of a girder. A girder is the main steel support of the superstructure. In addition, the rebar contributes to tensile strength and ductility to reinforced concrete structures, and corrosion of the rebar causes loss in strength. The corrosion process normally occurs due to aging, however the process is faster if penetration of water and chloride occurs. For example, chloride composites are spread over the deck of a brigde to accelerate meting of snow, however chloride composites cause corrosion. Once the corrosion starts, the oxidation causes the metal to expand which causes an internal crack and eventually the metal will spall as shown in Figure 2. Therefore, finding corrosion and cracks is very important and it requires Non-Destructive Testing (NDT).

While extreme weather conditions, disastrous car accidents or wear and tear due to old age contribute to a bridge becoming structurally deficient, and another component that can occur without notice are earthquakes. The Federal Highway Administration has reports on the damage to bridges due to the May 12, 2008 Wenchuan Earthquake in China (12). While it is easy for one to realize the damage done to a bridge from a external visual inspection, what about the internal damage done to the structure?

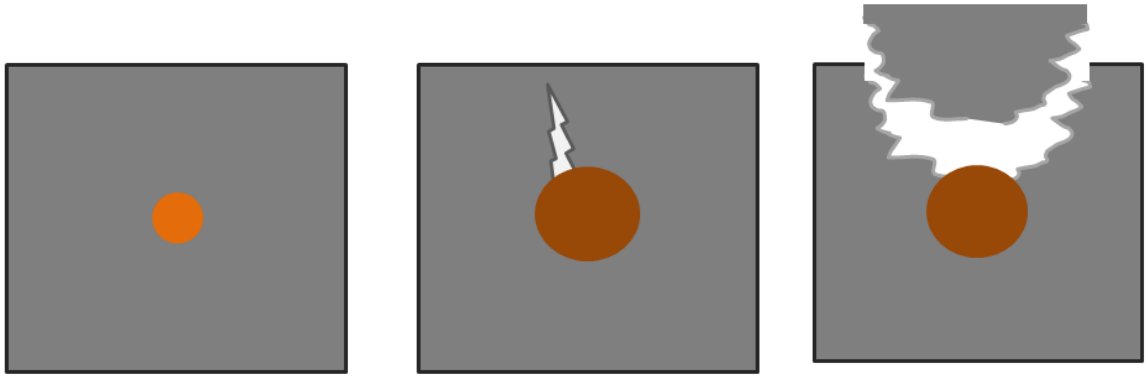

(a) (b) (c)

Figure 2: Problem in aging reinforced concrete, (a) Healthy concrete, (b) Corrosion and (c) Spalling.

1.1 Non-Destructive Testing methods

An inspection of bridges normaly requires Non-Destructive Testing (NDT). Civil engineers usually prepare multiple methods and choose the most appropiate for the specific demand of an investigation. Advantages and disadvantages of commonly used methods are well summarized in (13; 14).

1. **Visual inspection**: Skilled civil engineers investigate the surface conditions of bridges visually. Visual inspections are used on a regular basis and are part of any regular inspection routine for a bridge. Decisions for further investigations are made based on the test. Cracks or any changes in color on the surface of the concrete can be identified by this inspection. Further investigations are determined based on this initial inspection. Hammer sounding and the chain dragging are also part of a visual inspection (14). A

delaminated area can be identified by resulting sound from the hammer sounding and chain dragging tests. The advantage of visual inspection is its low cost of operation while its disadvantage is the method relys on skilled civil engineers.

2. **Proof loading test**: A Proof loading test usually uses heavily loaded trucks that are stationed on top of the bridge so that deflections can be measured. A proof loading test concludes the definitive rating of a bridges strength; however the operation is very slow and possibly dangerous. Typical proof loading level is about twice the maximum legal load. A more accurate description on proof loading may be found in the guideline (15). In (16), deflections in the girders were measured for two bridges. Several loads were placed on the deck and compared with the expected deflection. Rating of both bridges increased after the evaluation because the proof loading test provided a decisive measure of the structural health.

3. **Sonic/ultrasonic methods**: The sonic/ultrasonic methods have been well studied and successfully used to evaluate the structural health of reinforced concrete structures. Although there are many sonic/ultrasonic methods used, three of the most popular are mentioned, ultrasonic pulse velocity, impact echo and acoustic emission testing.

   Ultrasonic pulse velocity is used to evaluate material uniformity by estimating an average local velocity along a path. Transmission of an acoustic wave is initiated by an impact hammer. The wave is then received by an accelerometer. Propagation time is measured, and the velocity is estimated along the path. A simple however useful configuration of the test is direct transmission. An impact hammer and an accelerometer are placed on

a opposite side of reinforced concrete. In this configuration, the elastic wave initiated by the hammer might be detected among multiple elastic waves by the accelerometer due to multiple paths, however the first arrival wave is used to estimate material homogeneity. Ultrasonic pulse velocity testing in direct transmission configuration has been successfully used to identify cracks and delamination by detecting air cavities which are obstacles against propagation along the direct path of the acoustic wave transmitted within the reinforced concrete structure. Furthermore, multipath sonic transmission can be analyzed to compute tomographic reconstruction of velocity distributions which may be correlated with the internal structure. Sonic/ultrasonic pulse velocity methods are reliable methods, but they require a great amount of attention to detail while recording the data, and the preparation process can be painstaking since one must be very careful and precise (17).

In recent development a sonic method was introduced which involves the analysis in the frequency domain, known as the impact echo testing. In the impact echo testing method, an impulse transducer and a recording accelerometer are located adjacent to each other, and data acquisition systems are used to measure the reflections of the waves. Multiple reflections produce a resonating behavior due to an anomaly, and the corresponding resonance appears as a peak in frequency domain (18). By applying the Fast Fourier Transform of the recorded signals to transfer from the time domain to the frequency domain one can analyze the peak frequencies of the frequency spectrum. This allows one to monitor any change in the condition of a reinforced concrete structure. The main application for the impact echo testing method is to identify delamination and cracks or

air cavities within a reinforced concrete structure. Therefore, there is limited research on the effectiveness for using this method to detect the corrosion of rebar or steel within a reinforced concrete structure (19).

Acoustic emission is a passive technique which monitors the elastic waves generated from a reinforced concrete structure over a long period of time(19). Accelerometers are placed to monitor a reinforced concrete structure for a period of months and record the elastic waves generated by rapid energy which are released due to the internal cracking or corrosion of a reinforced concrete structure. The method is very cost effective for long-term monitoring. It provides convincing observations by recording the number of hits and events of an acoustic emission signal. The acoustic emission method uses the roughness value (RA) and the average frequency of a source as its two parameters. A crack type can be shown as the relationship between the roughness value and the average frequency. This allows to distinguish between shear cracks or tensile cracks. A hit is the detection of an acoustic emission signal and an event is the local material change, while an event can be classified as the number of hits recorded. In (19), the sudden rise of hits and the signal strength of recorded elastic waves are observed in their experiment and the corrosion level was quantified.

4. **Electrochemical methods**: The corrosion of reinforcing bars is often caused by oxidation. In the electrochemical method (20), Open Circuit Potential measurement is used to determine the corrosion in a reinforced concrete structure. The Linear Polarization Resistance Measurement is commonly used to measure the corrosion rate of the reinforc-

ing steel within a concrete structure. The Galvanostatic Pulse Method is an improved method of the Linear Polarization Resistance measurement for the reinforcing steel within a concrete structure. The resistivity measurement can evaluate the corrosion risk near the surface of a concrete structure.

The Open Circuit Potential measurement such as the half-cell potential measurement is suitable to plot the probability of corrosion in a reinforced concrete structure, often this is used for severely exfoliated reinforced concrete (21; 20). The procedure of half-cell potential measurements is well described in (21). A working electrode is directly connected to the reinforcing bar while a reference electrode and the concrete are properly connected by wetting the concrete surface. The voltage between those electrodes is measured. The reference electrode attached to the concrete surface scans over different points which can be used to provide a contour plot to map the probability of corrosion. Because of the simplicity of this method it is widely used. The authors of (20) pointed out some of the disadvantages, such as time consumption for taking a measurement, and lack of accuracy due to the requirement of knowledge needed for the type of the concrete and the sensitivity of the equipment. This technique is not suitable for evaluating the corrosion rate of rebar and typically one will incorporate other techniques for further evaluation. In fact, there are many variables that can affect the voltage reading such as moisture levels and the level of chloride concentration. Therefore, the voltage reading sometimes will not provide a decisive reading of the amount of corrosion. However, this method is complementary when used with other methods for improving decision making (22).

The Linear Polarization Resistance Measurement is commonly used for measuring the corrosion rate of a reinforcing steel bar. A pair of electrodes are attached to the reinforcing bar and to the surface of the concrete. This is similar the Open Circuit Potential method. In the Linear Polarization Resistance Measurement, potentiostatic controls are used to apply a linear voltage sweep to the reinforcing bar to measure the current response. Polarization resistance is calculated by the slope of the measured IV-curve using the Stern-Geary equation (20). The polarization resistance indicates the corrosion rate. The term polarization is used because Polarization Resistance is calculated from amount of change in voltage and current, in contrast Ohm's law uses stationary voltage and current. In (20), it is mentioned that errors in the surface area of the steel lead to inaccurate measurements. While setting up for the linear polarization resistance measurement, the surface area of the rebar is assumed to be lying directly beneath the electrode. However, research suggests that the current flowing from electrode can spread over a larger area. When the corrosion current density is calculated, since surface area of steel are the unknown, the measurement can be misleading.

The Galvanostatic Pulse Method is an improved method of the Linear Polarization Resistance measurement. This method uses a guard ring which is placed outside of the electrode that improves the confinement of the current flow. This reduces the limitation of the Linear Polarization Resistance method. Therefore, it provides more accurate values for the surface area of rebar and the corrosion rate of the reinforcing steel. Also, this method uses a potentiostatic device which can choose a range of potential fall and

analyzed the linear range of the IV-curve. By choosing a linear region, the risk of the inaccuracy due to the Galvano-static perturbation can be avoided. However, the confinement of current flow is still problematic when the covering concrete layer is too thick.

Resistivity measurements can evaluate the corrosion risk near the surface of a concrete structure(20). Electrodes are attached to the surface of the concrete structure. They apply a constant electric field and measure currents between two node pairs. Resistivity is calculated by Ohm's law and the distance between the two nodes. High resistivity indicates that the corrosion risk is low while low resistivity implies the corrosion risk is high. The Wenner four probe method is generally applied when using the resistivity method(19). The Wenner four probe method applies an impressed current between the two outer electrodes and measures the voltage drop between two inner electrodes. The resistivity measurement provides a reliable estimate of the corrosion risk of the concrete structure being evaluated.

5. **Infrared Thermography**: Infrared Thermography provides image of temperature distribution over reinforced concrete (23). All objects above absolute temperature (0K) radiate infrared rays. The simplest method use an infrared camera to record the radiation and to plot the temperature distribution. For reinforced concrete, the thermal conductivity of a metal is higher than concrete, therefore reinforcing bars can be mapped by identifying the higher temperature and temparature rises over time such as demonstrated in (24). Structural health can be evaluated by finding abnormal temperature distribution.

More advanced Infrared Tomography techniques involve combination with heat induction. In (23), several methods are mentioned such as pulsed thermography, Lock-in thermography and Pulsed phase thermography. Pulsed thermography uses short duration heat pulse to analyze transient response while Lock-in thermography analyzes temperature with stationary heat stimulation. Pulsed phase thermography is the combined method of those two, but also phase analysis is provided by Fourier transforming time domain data. In (25), heat diffusion is monitored when heat induction is applied. Since corroded metal have very low conductivity, Infrared Tomography can be used to estimate level of corrosion by measuring the heat transfer over reinforcing bars.

6. **Ground Penetrating Radar:** Ground Penetrating Radar (GPR) is commonly used to detect underground objects. For civil engineering purpose, GPR is a very common method to scan the deck of a bridge to monitor the surface condition and the internal structure near the surface (24; 26; 27). Also, small GPR units are available to inspect other parts of concrete. For example, GSSI Geophysical Survey Systems Inc produces handheld and stroller types (28). For their product, the GPR unit can scan deck of bridge for up to a depth of 0.6 m. The penetration depth is limited due to the attenuation of concrete. The penetration can go deeper by using lower frequency in theory, however, this sacrifices the resolution which is not suitable for inspection of bridge structure.

   This method is described well in (29). The GPR unit sends pulsed electromagnetic waves into the concrete structure and records returned signals due to objects which have different permittivity or conductivity (see Figure 1 of (29)). The returned signals have time delay

due to the propagation within the concrete, and peaks of strength in time of arrival indicates the location of objects (see Figure 2 of (29)). Raw data contains signal strength in time, and it is expressd in terms of distance by assuming the permittivity of the concrete. The GPR unit scans over a area of surface, it provides contour plot (see Figure 4 of (29)) and it is possible to identify the thickness of pavement, and locate the depth of rebars using mobile GPR system.

1.2 Historical background of RF Tomography

Theoritical works of Diffraction Tomography and Microwave Tomography were researched by Dr. Karl J. Langenberg, Dr. Weng Cho Chew, Dr. Anthony J. Devaney and Dr. Norbert N. Bojarski (30; 31; 32; 33; 34; 35) . From the theoritical work, Dr. Michael Wicks developed initial work of RF Tomography (36) as an alternative method to Ground Penetrating Radar (GPR) for underground imaging. On the one hand, RF Tomography was initially developed for tomographic imaging of deep underground cavities, such as tunnels. RF Tomography is superior to Ground Penetrating Radar for this purpose. The next few paragraphs will provide a brief list of the advantages of RF tomography.

The first advantage of RF tomography is its wide area monitoring capability. Existing Ground Penetrating Radar systems collect only mono-static signal returns, and the device being used, must be physically scanned along the site of interest. On the other hand, RFT uses sensors which act like transmitters and/or receivers. These sensors are distributed around the area of interest. All the data is collected at once and synthesized in a post-process. The distributed sensors allow us to monitor a wide area of interest at once. This capability is very useful when monitoring activities in a tunnel over a long period of time.

The second advantage is the feasibility of tomographic imaging by narrow band frequencies. For Ground Penetrating Radar, the selection of operating frequencies is a compromise between resolution and the penetration of electromagnetic waves. In GPR, a higher frequency is preferred to achieve high resolution while a lower frequency is preferred to ensure enough penetration due to the Signal to Noise Ratio (SNR) and the dynamic range of the equipment being used.

However, RF Tomography takes full advantage of the spatial diversity in the tomographic process, therefore even monochromatic signals can achieve clear images. When a measurement configuration is limited to only mono-static configuration like the GPR, an achievable resolution is also limited by the nominal range resolution (down range resolution) and the bandwidth of the operating frequency, while the resolution of a multi-static configuration like RF Tomography can be much higher due to the cross range resolution, which only depends on the frequency (37).

The third advantage is that the image provided by RF tomography will display property information of the materials being tested. GPR and also Synthetic Aperture Radar (SAR) reconstruct an image based on the travelling time between transmitter and receiver. While reconstructing object parameters can be achieved using correlation techniques, (38; 39) in GPR and SAR, RF Tomography produces permittivity distribution in reconstruction. The forward model of RF Tomography is derived from the volume integral equation using the permittivity as the unknown quantity to be reconstructed. In general, a wave-front reconstruction technique like the one used in GPR and SAR is suitable for mapping objects in a far-field (Fraunhofer) region while RF Tomography is suitable to reconstruct the near-field (Fresnel) region. Wave-front reconstruction techniques usually assume plane wave propagation, which can make it difficult to handle multiple scattering. Analysis on multiple scattering is also challenging in RF Tomography. The exact forward model accounts for multiple scattering, however advanced inverse techniques are required to avoid a problem of local minimum solution. The local minimum solution satisfies the forward model, however it provides unrealistic and undisired solutions.

A quadratic forward model has been reasearched to consider double scattering phenomenon. Corresponding articles for the quadratic forward model can be found in (40; 41; 42; 43; 44; 1).

The advantages of RF Tomography make it appropriate to investigate reinforced concrete. As mentioned in the previous section, Ground Penetrating Radar is currently used to examine the structural health of reinforced concrete. RF tomography can provide additional information to help assess the priority of a rehabilitation program since the multi-static configuration will provide a higher resolution. Therefore, it is easier to identify the real problems and defects inside a reinforced concrete structure. Another advantage of using RF tomography is that it can be used to identify the difference between a hollow cavity and rebar inside a concrete structure by looking at the reconstructed contrast.

1.3 Summary of chapters

The goal of this thesis is to provide a fair comparison of multi-monostatic measurement configurations for Ground Penetrating Radar and multi-static measurement configurations for the inspection of reinforced concrete structures. Structure of thesis is as follows.

Chapter 2 reviews the theoretical background of RF Tomography. Derivation of forward models and inversion techniques are introduced to have clear idea of RF Tomography.

In chapter 3, a forward model for reinforced concrete structure is constructed. A supporting pile structure is modeled as a dielectric cylinder with a circular cross section. Derivation of analytical solutions are provided and used to develop the forward model. The forward model and association Green's functions were formulated by relating the analytical solution with the Green's function.

In chapter 4, resolution analysis for the forward model for reinforced concrete structure found in chapter 3. The goal of this resolution analysis was to compare achievable resolution of three configurations which are associated with configurations of Grround Penetrating Radar or RF Tomography. In order to focus only on achievable resolution of configurations, level of complexity due to electromagnetic scattering and diffraction are removed by producing scattered electric field from forward calculation for an ideal image.

In chapter 5, examples of tomographic reconstructions are provided. Unlike in chapter 4, scattered electric fields are produced from Method of Moment simulations and experiments. First set of examples uses Method of Moment simulations to produce numerical scattered electric field. Second set of examples contains experiments conducted at Andrew Electromagnetics Laboratory, University of Illinois at Chicago.

Chapter 6 summarizes the results obtained in this thesis, and concludes with a discussion on future investigations.

CHAPTER 2

REVIEW OF RADIO FREQUENCY TOMOGRAPHY

This chapter provides a review of RF Tomography limited to the concepts that are needed to understand the application of RF Tomography to the investigation of reinforced concrete structures in the following chapters. For a thorough review of RF Tomography, one should read thesises and book chapeters of (1; 45; 46), and articles of (36; 47; 48; 49; 50; 51; 52; 53; 54; 55; 56; 57; 58; 59; 60; 61; 62; 63; 64; 65; 66; 67; 68; 69; 70; 71; 72; 73; 74; 75; 76; 77; 78; 79; 80; 81; 42; 43; 44; 82; 83; 84; 6; 85; 86; 87).

2.1 Equivalent theorem

The derivation of a volume integral equation can found in (88; 89), and it provides forward models of RF Tomography.

Consider electric and magnetic current sources $\mathbf{J}_{\mathrm{i}}$ and $\mathbf{M}_{\mathrm{i}}$ which create total fields $\mathbf{E}^{\mathrm{t}}$ and $\mathbf{H}^{\mathrm{t}}$ in a scene with the present of an object. Maxwell's equations can be written as

$$\nabla \times \mathbf{E}^{\mathrm{t}} = -\mathbf{M}_{\mathrm{i}} - j\omega\mu(\mathbf{r}')\mathbf{H}^{\mathrm{t}}, \tag{2.1}$$

$$\nabla \times \mathbf{H}^{\mathrm{t}} = \mathbf{J}_{\mathrm{i}} + j\omega\varepsilon(\mathbf{r}')\mathbf{E}^{\mathrm{t}}, \tag{2.2}$$

where $\mu(\mathbf{r}')$ and $\varepsilon(\mathbf{r}')$ are the local permeability and permittivity, respectively.

Next, the same current sources $\mathbf{J}_{\mathrm{i}}$ and $\mathbf{M}_{\mathrm{i}}$ in absence of objects create incident fields $\mathbf{E}^{\mathrm{i}}$ and $\mathbf{H}^{\mathrm{i}}$,

$$\nabla \times \mathbf{E}^{\mathrm{i}} = -\mathbf{M}_{\mathrm{i}} - j\omega\mu_b \mathbf{H}^{\mathrm{i}}, \tag{2.3}$$

$$\nabla \times \mathbf{H}^{\mathrm{i}} = \mathbf{J}_{\mathrm{i}} + j\omega\varepsilon_b \mathbf{E}^{\mathrm{i}}, \tag{2.4}$$

where subscript $_b$ indicates a background medium.

Subtraction of Equation 2.3 from Equation 2.1 and Equation 2.4 from Equation 2.2 gives

$$\nabla \times (\mathbf{E}^{\mathrm{t}} - \mathbf{E}^{\mathrm{i}}) = -j\omega(\mu(\mathbf{r}')\mathbf{H}^{\mathrm{t}} - \mu_b \mathbf{H}^{\mathrm{i}}), \tag{2.5}$$

$$\nabla \times (\mathbf{H}^{\mathrm{t}} - \mathbf{H}^{\mathrm{i}}) = j\omega(\varepsilon(\mathbf{r}')\mathbf{E}^{\mathrm{t}} - \mu_b \mathbf{E}^{\mathrm{i}}). \tag{2.6}$$

By definition, scattered fields are $\mathbf{E}^{\mathrm{s}} = \mathbf{E}^{\mathrm{t}} - \mathbf{E}^{\mathrm{i}}$, $\mathbf{H}^{\mathrm{s}} = \mathbf{H}^{\mathrm{t}} - \mathbf{H}^{\mathrm{i}}$, so that

$$\nabla \times \mathbf{E}^{\mathrm{s}} = -j\omega(\mu(\mathbf{r}') - \mu_b)\mathbf{H}^{\mathrm{t}} - j\omega\mu_b \mathbf{H}^{\mathrm{s}}, \tag{2.7}$$

$$\nabla \times \mathbf{H}^{\mathrm{s}} = j\omega(\varepsilon(\mathbf{r}') - \mu_b)\mathbf{E}^{\mathrm{t}} + j\omega\varepsilon_b \mathbf{E}^{\mathrm{s}}. \tag{2.8}$$

The volume equivalent electric and magnetic currents $\mathbf{J}_{\mathrm{eq}}$ and $\mathbf{M}_{\mathrm{eq}}$ are defined as

$$\mathbf{J}_{\mathrm{eq}}(\mathbf{r}') = j\omega(\varepsilon(\mathbf{r}') - \varepsilon_b)\mathbf{E}^{\mathrm{t}} \tag{2.9}$$

$$\mathbf{M}_{\mathrm{eq}}(\mathbf{r}') = j\omega(\mu(\mathbf{r}') - \mu_b)\mathbf{H}^{\mathrm{t}} \tag{2.10}$$

Therefore, the scattered field can be written as

$$\nabla \times \mathbf{E}^{\mathrm{s}} = -\mathbf{M}_{\mathrm{eq}}(\mathbf{r}') - j\omega\mu_b \mathbf{H}^{\mathrm{s}} \tag{2.11}$$

$$\nabla \times \mathbf{H}^{\mathrm{s}} = \mathbf{J}_{\mathrm{eq}}(\mathbf{r}') + j\omega\varepsilon_b \mathbf{E}^{\mathrm{s}} \tag{2.12}$$

which have the same form as equation as 2.1 and 2.2 by replacing $\mathbf{E}^{\mathrm{i}}$, $\mathbf{H}^{\mathrm{i}}$, $\mathbf{J}_{\mathrm{i}}$ and $\mathbf{M}_{\mathrm{i}}$ to $\mathbf{E}^{\mathrm{s}}$, $\mathbf{H}^{\mathrm{s}}$, $\mathbf{J}_{\mathrm{eq}}$ and $\mathbf{M}_{\mathrm{eq}}$.

2.2 Integral equation

Applying the curl operator to the previous equations yields

$$\nabla \times \nabla \times \mathbf{E}^{\mathrm{s}} - \omega^2 \varepsilon_b \mu_b \mathbf{E}^{\mathrm{s}} = -\nabla \times \mathbf{M}_{\mathrm{eq}}(\mathbf{r}') - j\omega\mu_b \mathbf{J}_{\mathrm{eq}}(\mathbf{r}'), \tag{2.13}$$

$$\nabla \times \nabla \times \mathbf{H}^{\mathrm{s}} - \omega^2 \varepsilon_b \mu_b \mathbf{E}^{\mathrm{s}} = \nabla \times \mathbf{J}_{\mathrm{eq}}(\mathbf{r}') - j\omega\varepsilon_b \mathbf{M}_{\mathrm{eq}}(\mathbf{r}'). \tag{2.14}$$

In the case of non-magnetic materials ($\mu = \mu_b$), the equivalent magnetic current is zero, $\mathbf{M}_{\mathrm{eq}} = 0$, and Equation 2.13 becomes

$$\nabla \times \nabla \times \mathbf{E}^{\mathrm{s}} - \omega^2 \varepsilon_b \mu_b \mathbf{E}^{\mathrm{s}} = -j\omega\mu_b \mathbf{J}_{\mathrm{eq}}(\mathbf{r}') \tag{2.15}$$

In order to formulate an integral equation, a dyadic Green's function is needed. The corresponding dyadic Green's function for the background medium must satisfy

$$\nabla \times \nabla \times \underline{\underline{\mathbf{G}}}(\mathbf{r}, \mathbf{r}'; k_b) - \omega^2 \epsilon_b \mu_b \underline{\underline{\mathbf{G}}}(\mathbf{r}, \mathbf{r}'; k_b) = \underline{\underline{\mathbf{I}}}\delta(\mathbf{r} - \mathbf{r}') \tag{2.16}$$

where k_b represents that Green's function of the background medium characterized by ε_b and μ_b

Performing the dot product of Equation 2.15 and $\underline{\underline{\mathbf{G}}}(\mathbf{r},\mathbf{r}')$, as well as the dot product of $\mathbf{E}^{\mathrm{s}}$ and Equation 2.16 provide

$$\nabla\times\nabla\times\mathbf{E}^{\mathrm{s}}\cdot\underline{\underline{\mathbf{G}}}(\mathbf{r},\mathbf{r}';k_b)-\omega^2\varepsilon_b\mu_b\mathbf{E}^{\mathrm{s}}\cdot\underline{\underline{\mathbf{G}}}(\mathbf{r},\mathbf{r}';k_b)=-j\omega\mu_b\mathbf{J}_{\mathrm{eq}}(\mathbf{r}')\cdot\underline{\underline{\mathbf{G}}}(\mathbf{r},\mathbf{r}';k_b) \tag{2.17}$$

$$\mathbf{E}^{\mathrm{s}}\cdot\nabla\times\nabla\times\underline{\underline{\mathbf{G}}}(\mathbf{r},\mathbf{r}';k_b)-\omega^2\epsilon_b\mu_b\mathbf{E}^{\mathrm{s}}\cdot\underline{\underline{\mathbf{G}}}(\mathbf{r},\mathbf{r}';k_b)=\mathbf{E}^{\mathrm{s}}\cdot\mathbf{I}\delta(\mathbf{r}-\mathbf{r}'). \tag{2.18}$$

Subtraction of 2.18 from 2.17 gives

$$\nabla\times\nabla\times\mathbf{E}^{\mathrm{s}}\cdot\underline{\underline{\mathbf{G}}}(\mathbf{r},\mathbf{r}';k_b)-\mathbf{E}^{\mathrm{s}}\cdot\nabla\times\nabla\times\underline{\underline{\mathbf{G}}}(\mathbf{r},\mathbf{r}';k_b)=-j\omega\mu_b\mathbf{J}_{\mathrm{eq}}(\mathbf{r}')\cdot\underline{\underline{\mathbf{G}}}(\mathbf{r},\mathbf{r}';k_b)-\mathbf{E}^{\mathrm{s}}\cdot\mathbf{I}\delta(\mathbf{r}-\mathbf{r}'). \tag{2.19}$$

The vector Green's theorem can be applied to the left hand side of the equation, and results in

$$\nabla\cdot[\nabla\times\mathbf{E}^{\mathrm{s}}\times\underline{\underline{\mathbf{G}}}(\mathbf{r},\mathbf{r}';k_b)-\nabla\times\underline{\underline{\mathbf{G}}}(\mathbf{r},\mathbf{r}';k_b)\times\mathbf{E}^{\mathrm{s}}]=-j\omega\mu_b\mathbf{J}_{\mathrm{eq}}(\mathbf{r}')\cdot\underline{\underline{\mathbf{G}}}(\mathbf{r},\mathbf{r}';k_b)-\mathbf{E}^{\mathrm{s}}\cdot\mathbf{I}\delta(\mathbf{r}-\mathbf{r}') \tag{2.20}$$

When the volume integral is evaluated for the equation above, its left hand side returns zero to satisfy the radiation condition for the Green's function. Finally, the reciprocity of Green's function $\underline{\underline{\mathbf{G}}}(\mathbf{r}', \mathbf{r}; k_b) = \underline{\underline{\mathbf{G}}}(\mathbf{r}, \mathbf{r}'; k_b)^t$ leads to the volume integral equation for the scattered field

$$\mathbf{E}^{\mathrm{s}}(\mathbf{r}) = -j\omega \iiint_V \mu_b \underline{\underline{\mathbf{G}}}(\mathbf{r}, \mathbf{r}'; k_b) \cdot \mathbf{J}_{\mathrm{eq}}(\mathbf{r}') d\mathbf{r}' \tag{2.21}$$

Similarly, an integral equation for the field without anomaly can be formulated from Equation 2.3 and Equation 2.4 yielding

$$\mathbf{E}^{\mathrm{i}}(\mathbf{r}) = -j\omega \iiint_V \mu_b \underline{\underline{\mathbf{G}}}(\mathbf{r}, \mathbf{r}'; k_b) \cdot \mathbf{J}_{\mathrm{i}}(\mathbf{r}') d\mathbf{r}' \tag{2.22}$$

2.3 Exact forward model

The exact forward model of RF Tomography can be found by substituting Equation 2.9 into Equation 2.21 and Equation 2.22 and assuming $\mu_b = \mu_0$,

$$\mathbf{E}^{\mathrm{t}}(\mathbf{r}) = -j\omega\mu_0 \iiint_V \underline{\underline{\mathbf{G}}}(\mathbf{r}, \mathbf{r}'; k_b) \cdot \mathbf{J}_{\mathrm{i}}(\mathbf{r}') d\mathbf{r}' + \iiint_V \omega^2 \mu_0 \varepsilon_0 \varepsilon_\delta(\mathbf{r}') \underline{\underline{\mathbf{G}}}(\mathbf{r}, \mathbf{r}'; k_b) \cdot \mathbf{E}^{\mathrm{t}}(\mathbf{r}') d\mathbf{r}' \tag{2.23}$$

$$= \mathbf{E}^{\mathrm{i}}(\mathbf{r}) + \mathbf{E}^{\mathrm{s}}(\mathbf{r}) \tag{2.24}$$

where the first term corresponds to incident field due to known background geometry while the second term corresponds to scattered field due to deviation from background geometry. The scattered fields exist due to anomaly distribution represented in terms of the variation of the

dielectric permittivity with respect to a background material, i.e. the contrast function defined by

$$\varepsilon_\delta(\mathbf{r}') = \varepsilon_r(\mathbf{r}') - \varepsilon_b - j\frac{(\sigma(\mathbf{r}') - \sigma_b)}{2\pi f \varepsilon_0} \tag{2.25}$$

where ε_r and ε_b are relative permitivities of local and background medium, and $\sigma(\mathbf{r}')$ and σ_b are conductivities of local and background media.

A more familiar notation using freespace background ($\varepsilon_b = 1$) in many articles (69; 77; 76; 77), is

$$\mathbf{E}^{\mathrm{t}}(\mathbf{r}) = -j\omega\mu_0 \iiint_V \underline{\underline{\mathbf{G}}}(\mathbf{r},\mathbf{r}') \cdot \mathbf{J}_{\mathrm{i}}(\mathbf{r}') d\mathbf{r}' + k_0^2 \iiint_V \underline{\underline{\mathbf{G}}}(\mathbf{r},\mathbf{r}') \cdot \varepsilon_\delta(\mathbf{r}') \mathbf{E}^{\mathrm{t}}(\mathbf{r}') d\mathbf{r}', \tag{2.26}$$

where wave-number has a relationship of $k = \omega^2\mu\varepsilon$. In this thesis, the notation of 2.23 is used because the focus is on inhomogeneous background medium in later chapters.

However, the problem of inverting the previous equation requires a non-linear inversion. We are interested in finding the distribution of $\varepsilon_\delta(\mathbf{r}')$ which changes $\mathbf{E}^{\mathrm{t}}(\mathbf{r}')$ and $\underline{\underline{\mathbf{G}}}(\mathbf{r},\mathbf{r}';k_b)$ as well.

Such an inverse problem is studied in (30; 31). The procedure decribed in (31) to solve the non-linear inversion is as follows.

1. implement the integral equation with Green's function for freespace.
2. solve the inverse problem to find permittivity distribution $\varepsilon_\delta(\mathbf{r}')$.

3. repeat step 1 and 2 by updating new integral equation with background permittivity found in step 2 until this process converges. When this procedure converges, Equation 2.23 will provide the first term.

However in reality, the inverse problem in step 2 is known to be ill posed, and regularization approaches must be used. There are many combinations of permittivity distribution $\varepsilon_r(\mathbf{r}')$ that can possibly satisfy 2.23, and the challenge is how to select the solution that converges to the preferred solution.

2.4 Born approximation model

In order to simplify exact forward model, the Born approximation is used. The Born approximation model usually assumes simple geometries such as freespace for which analytical Green's functions are available.

The Born approximation is the assumption that the difference of wave number is very small $k(\mathbf{r}')^2 \approx k_b^2$, and leads to a scattered field is very small compared to the incident field. The total electric field $\mathbf{E}^{\mathrm{t}}(\mathbf{r}')$ of 2.23 for freespace background geometry yields

$$\mathbf{E}^{\mathrm{t}}(\mathbf{r}') = \mathbf{E}^{\mathrm{i}}(\mathbf{r}') + \mathbf{E}^{\mathrm{s}}(\mathbf{r}') \approx \mathbf{E}^{\mathrm{i}}(\mathbf{r}'). \tag{2.27}$$

Therefore, 2.23 becomes

$$\mathbf{E}^{\mathrm{t}}(\mathbf{r}) = -j\omega\mu_0 \iiint_V \underline{\underline{\mathbf{G}}}(\mathbf{r},\mathbf{r}';k_b)\cdot\mathbf{J}_{\mathrm{i}}(\mathbf{r}')d\mathbf{r}' + k_0^2 \iiint_V \underline{\underline{\mathbf{G}}}(\mathbf{r},\mathbf{r}';k_b)\cdot\varepsilon_\delta(\mathbf{r}')\mathbf{E}^{\mathrm{i}}(\mathbf{r}')d\mathbf{r}'. \tag{2.28}$$

The advantage of the Born approximation is that the permittivity distribution ε_δ is the only unknown on the right hand side of equation. Therefore, the resulting forward model is linear, and relatively easy to deal with the inverse problem.

2.5 Quadratic model

The quadratic model is introduced to balance the complexity of inverse problem and the accuracy of forward model.

Let us start to derive the quadratic forward model by expanding the exact forward model of 2.23. The local total field $\mathbf{E}^{\mathrm{t}}(\mathbf{r}')$ can be substituted by itself, and the forward model is expanded into recursive form,

$$\begin{aligned}\mathbf{E}^{\mathrm{t}}(\mathbf{r}) = \mathbf{E}^{\mathrm{i}}(\mathbf{r}') &+ k_0^2 \iiint_V \underline{\underline{\mathbf{G}}}(\mathbf{r},\mathbf{r}';k_b)\cdot\varepsilon_\delta(\mathbf{r}')\mathbf{E}^{\mathrm{i}}(\mathbf{r}') \\ &+ k_0^2 \iiint_V \underline{\underline{\mathbf{G}}}(\mathbf{r},\mathbf{r}';k_b)\cdot\varepsilon_\delta(\mathbf{r}')\left[k_0^2 \iiint_V \underline{\underline{\mathbf{G}}}(\mathbf{r}',\mathbf{r}'';k_b)\cdot\varepsilon_\delta(\mathbf{r}')\mathbf{E}^{\mathrm{i}}(\mathbf{r}'')d\mathbf{r}''\right]d\mathbf{r}' \\ &+ k_0^2 \iiint_V \underline{\underline{\mathbf{G}}}(\mathbf{r},\mathbf{r}';k_b)\cdot\varepsilon_\delta(\mathbf{r}')\left[k_0^2 \iiint_V \underline{\underline{\mathbf{G}}}(\mathbf{r}',\mathbf{r}'';k_b)\cdot\varepsilon_\delta(\mathbf{r}')\mathbf{E}^{\mathrm{s}}(\mathbf{r}'')d\mathbf{r}''\right]d\mathbf{r}' \qquad (2.29)\end{aligned}$$

One may keep substituting total field to expand the equation with infinite terms. 2.29 contains the incident field (1st term), a single scattering term (2nd term), a double scattering term (3rd term) and further multi-scattering terms (4th term). Quadratic forward model is found by approximation of the multi-scattering that is more than double (4th term). Also, please notice that the Born approximation model is the same when 3rd and 4th term of the equation are ignored.

Articles (90; 40; 41; 1) provides further detail of the quadratic forward model and its implementation. Experimental validations in freespace are provided in (44; 42), and numerical result of inhomogeneous background geometry is provided in (43) as preliminary result for future work.

2.6 RF Tomography using infinitesimal dipoles

In this section, RF Tomography for infinitesimal dipoles is introduced. In previous sections, forward models are written in general form assuming that $\mathbf{J}_{\mathrm{i}}$ or $\mathbf{E}^{\mathrm{i}}$ are produced from an antenna. When RF Tomography is deployed, measurements are performed by a Vector Network Analyzer (VNA) which produces an electromagnetic wave from the transmitting antenna (TX) and receives the electromagnetic wave by the receiving antenna (RX). In this section, a pair of TX and RX infinitesimal dipoles antennas are used.

Let us consider TX and RX as infinitesimal dipoles are located at $\mathbf{r}^{\mathrm{t}}$ and $\mathbf{r}^{\mathrm{r}}$, and their polarization states are represented by unit vectors $\mathbf{a}^{\mathrm{t}}$ and $\mathbf{a}^{\mathrm{r}}$, respectively. The TX antenna produces the incident current distribution $\mathbf{J}_{\mathrm{i}}$ at $\mathbf{r}^{\mathrm{t}}$ and electric fields everywhere. The incident field produced by the TX antenna is found by substituting the incident current distribution $I_0\ell$ for a infinitesimal dipole into 2.22,

$$\begin{aligned}\mathbf{E}^{\mathrm{i}}(\mathbf{r}^{\mathrm{r}},\mathbf{r}^{\mathrm{t}}) &= -j\omega\mu_0 \iiint_V \underline{\underline{\mathbf{G}}}(\mathbf{r}^{\mathrm{r}},\mathbf{r}^{\mathrm{t}};k_b)\cdot[\mathbf{a}^{\mathrm{t}} I_0\ell\delta(\mathbf{r}^{\mathrm{r}}-\mathbf{r}^{\mathrm{t}})]d\mathbf{r}' \\ &= -j\omega\mu_0 I_0\ell \underline{\underline{\mathbf{G}}}(\mathbf{r}^{\mathrm{r}},\mathbf{r}^{\mathrm{t}};k_b)\cdot\mathbf{a}^{\mathrm{t}}. \end{aligned} \tag{2.30}$$

Therefore, the incident field received by the RX antenna is

$$E^i(\mathbf{r}^{\mathrm{r}}, \mathbf{r}^{\mathrm{t}}) = \mathbf{a}^{\mathrm{r}} \cdot \mathbf{E}^{\mathrm{i}} = Q\mathbf{a}^{\mathrm{r}} \cdot \underline{\underline{\mathbf{G}}}(\mathbf{r}^{\mathrm{r}}, \mathbf{r}^{\mathrm{t}}; k_b) \cdot \mathbf{a}^{\mathrm{t}}, \tag{2.31}$$

where $Q = -j\omega\mu_0 I_0 d\ell$ is a normalization constant. The constant is normally canceled by a reference measurement.

The incident fields at $\mathbf{r}'$ is also substituted for the Born approximation model of 2.28,

$$\begin{aligned} E^t(\mathbf{r}^{\mathrm{t}}, \mathbf{r}^{\mathrm{r}}) &= E^i(\mathbf{r}^{\mathrm{r}}, \mathbf{r}^{\mathrm{t}}) + E^s(\mathbf{r}^{\mathrm{r}}, \mathbf{r}^{\mathrm{t}}) \\ &= Q\left[\mathbf{a}^{\mathrm{r}} \cdot \underline{\underline{\mathbf{G}}}(\mathbf{r}^{\mathrm{r}}, \mathbf{r}^{\mathrm{t}}; k_b) \cdot \mathbf{a}^{\mathrm{t}} + k_0^2 \iiint_D \mathbf{a}^{\mathrm{r}} \cdot \underline{\underline{\mathbf{G}}}(\mathbf{r}^{\mathrm{r}}, \mathbf{r}'; k_b) \cdot \varepsilon_\delta(\mathbf{r}') \underline{\underline{\mathbf{G}}}(\mathbf{r}', \mathbf{r}^{\mathrm{t}}; k_b) \cdot \mathbf{a}^{\mathrm{t}} d\mathbf{r}'\right]. \end{aligned} \tag{2.32}$$

where the symbol D is used to indicate domain of investigation (DoI) as subspace of the whole region V. In an actual problem, we set DoI as the only region, where the contrast $\delta(\mathbf{r}')$ is not potentially zero.

Next step is to convert the continuous integral form into a matrix form by partitioning the integral. Imagine that the DoI is partitioned into small cubic voxels with lengths dx, dy and dz, and assume the material property and field distribution are uniform within the voxels. The scattered field for a specific measurement can be expressed as sum of small integrals,

$$E_m^s(\mathbf{r}^{\mathrm{r}}, \mathbf{r}^{\mathrm{t}}) \approx Qk_0^2 \sum_{n=1}^{N} \varepsilon_{\delta n} \iiint_{D_n} \mathbf{a}_m^{\mathrm{r}} \cdot \underline{\underline{\mathbf{G}}}(\mathbf{r}_m^{\mathrm{r}}, \mathbf{r}'; k_b) \cdot \underline{\underline{\mathbf{G}}}(\mathbf{r}', \mathbf{r}_m^{\mathrm{t}} : k_b) \cdot \mathbf{a}_m^{\mathrm{t}} d\mathbf{r}'. \tag{2.33}$$

where subscript n and m indicates the index of voxels and measurements, respectively.

2.33 produces linear equations,

$$\mathbf{E}^{\mathrm{s}} = \mathbf{L} \cdot \mathbf{v}, \tag{2.34}$$

where $\mathbf{E}^{\mathrm{s}}$ and $\mathbf{v}$ are measurement and unknown contrast arrays, respectively. The unknown contrast array $v(\mathbf{r}')$ is the same as the contrast function $\varepsilon_\delta(\mathbf{r}')$ when element of matrix L is

$$\begin{aligned} L_{mn} &= Qk_0^2 \iiint_{V_p} \mathbf{a}^{\mathrm{r}} \cdot \underline{\underline{\mathbf{G}}}(\mathbf{r}^{\mathrm{r}}, \mathbf{r}'; k_b) \cdot \underline{\underline{\mathbf{G}}}(\mathbf{r}', \mathbf{r}^{\mathrm{t}} : k_b) \cdot \mathbf{a}^{\mathrm{t}} d\mathbf{r}' \\ &\approx Qk_0^2 [\mathbf{a}^{\mathrm{r}} \cdot \underline{\underline{\mathbf{G}}}(\mathbf{r}^{\mathrm{r}}, \mathbf{r}'; k_b) \cdot \underline{\underline{\mathbf{G}}}(\mathbf{r}', \mathbf{r}^{\mathrm{t}} : k_b) \cdot \mathbf{a}^{\mathrm{t}}] dxdydz. \end{aligned} \tag{2.35}$$

In the 2.34, the dimension of $\mathbf{E}^{\mathrm{s}}$, $\mathbf{v}$ are total number of measurements $M \times 1$, total number of unknowns $N \times 1$ respectively, therefore the dimension of the matrix $\mathbf{L}$ is $M \times N$.

2.7 RF Tomography using infinite line source

Cylindrical pillar structures may be investigated using a two-dimensional model, so we now focus our attention to the two-dimensional case, which will be used in later chapters. The derivation of two dimensional model is very similar to general model in three dimension which is mentioned in previous section.

There are two key points that make a difference going from the the three-dimensional model to the two-dimensional model. The first point is the electric field is due to a line source. In a two dimensional model, electric line sources are used to excite electric fields. Therefore, only $\hat{z}$ polarized fields exists in the space. The second point is that the Green's functions represents point to point propagation. When an infinite line source is excited, the electromagnetic wave

propagate in the xy-plane and it is sufficient to only consider the z component of the electric field. Since analytical solution of the two dimensional problem fits well in the cylindrical coordinate (ρ, ϕ, z), locations in the xy-plane are represented by $\boldsymbol{\rho}$. The exact forward model of 2.23 becomes all scalar,

$$E_z^t(\boldsymbol{\rho}^{\mathrm{r}}, \boldsymbol{\rho}^{\mathrm{t}}) = E_z^i(\boldsymbol{\rho}^{\mathrm{r}}, \boldsymbol{\rho}^{\mathrm{t}}) + E_z^s(\boldsymbol{\rho}^{\mathrm{r}}, \boldsymbol{\rho}^{\mathrm{t}}) \tag{2.36}$$

$$= -j\omega\mu_0 \iint_D g_e(\boldsymbol{\rho}^{\mathrm{r}}, \boldsymbol{\rho}'; k_b) I(\boldsymbol{\rho}') d\boldsymbol{\rho}' + k_0^2 \iint_D g_e(\boldsymbol{\rho}^{\mathrm{r}}, \boldsymbol{\rho}'; k_b) \varepsilon_\delta(\boldsymbol{\rho}') E_z^t(\boldsymbol{\rho}', \boldsymbol{\rho}^{\mathrm{t}}) d\boldsymbol{\rho}' \tag{2.37}$$

where g_e and I represent Green's function and current distribution in two dimension.

In particular, a thin line source I_e in freespace produces incident electric field

$$E_z^i(\boldsymbol{\rho}^{\mathrm{r}}, \boldsymbol{\rho}^{\mathrm{t}}) = -\frac{k_0^2 I_e}{4\omega\varepsilon_0} H_0^{(2)}\left(k_0 \left|\boldsymbol{\rho}^{\mathrm{r}} - \boldsymbol{\rho}^{\mathrm{t}}\right|\right). \tag{2.38}$$

Also, Maxwell Equation and the corresponding equation for the Green's function are

$$\nabla \times \nabla \times E_z^i(\boldsymbol{\rho}) - \omega^2 \varepsilon_0 \mu_0 E_z^i(\boldsymbol{\rho}) = -j\omega\mu_0 I_e \delta(\boldsymbol{\rho} - \boldsymbol{\rho}') \tag{2.39}$$

$$\nabla \times \nabla \times g_e(\boldsymbol{\rho}, \boldsymbol{\rho}'; k_0) - \omega^2 \epsilon_0 \mu_0 g_e(\boldsymbol{\rho}, \boldsymbol{\rho}'; k_0) = \delta(\boldsymbol{\rho} - \boldsymbol{\rho}'), \tag{2.40}$$

therefore, Green's function g_e is given by

$$g_e(\boldsymbol{\rho}, \boldsymbol{\rho}') = \frac{j}{\omega\mu_0} E_z^i(\boldsymbol{\rho}, \boldsymbol{\rho}') = -\frac{j}{4} H_0^{(2)}\left(k_0 \left|\boldsymbol{\rho} - \boldsymbol{\rho}'\right|\right) \tag{2.41}$$

For the Born approximation model, the model equation is still linear and the matrix elements of 2.34 are

$$\begin{aligned} L_{mn} &= k_0^2 \iint_{D_p} g_e(\boldsymbol{\rho}^{\mathrm{r}}, \boldsymbol{\rho}'; k_b) E_z^i(\boldsymbol{\rho}') d\boldsymbol{\rho}' \\ &= k_0^2 \iint_{D_p} \left[\frac{-j}{4} H_0^{(2)} \left(k_0 \left| \boldsymbol{\rho}^{\mathrm{r}} - \boldsymbol{\rho}' \right| \right) \right] \left[-\frac{k_0^2 I_e}{4\omega\varepsilon_0} H_0^{(2)} \left(k_0 \left| \boldsymbol{\rho}' - \boldsymbol{\rho}^{\mathrm{t}} \right| \right) \right] d\boldsymbol{\rho}' \\ &\approx Q k_0^2 [g_e(\boldsymbol{\rho}^{\mathrm{r}}, \boldsymbol{\rho}'; k_0) g_e(\boldsymbol{\rho}', \boldsymbol{\rho}^{\mathrm{t}}; k_0)] dx dy. \end{aligned} \tag{2.42}$$

where $Q = -j\omega\mu_0 I_e$.

2.8 Inversion algorithms

Linear equations such as 2.34 were introduced in previous sections. We are interested in finding the unknown $\mathbf{v}$ from measurements $\mathbf{E}^{\mathrm{s}}$. However, the number of unknown N is usually larger than number of measurements M, and the matrix $\mathbf{L}$ is rectangular shape and under-determined which has fewer equations than unknowns. Therefore, many solutions of $\mathbf{v}$ satisfy 2.34.

In this section, some inversion algorithms are introduced. Since there are many solutions available, finding a preferred solution is important.

2.8.1 Pseudo inverse

Pseudo-inverse is the most famous inverse technique to solve an under-determined matrix (91). Pseudo inverse provides a solution of the linear equations with minimum euclidean norm of the solution as

$$\mathbf{L}^{H} \cdot \mathbf{E}^{\mathrm{s}} = \mathbf{L}^{H}\mathbf{L} \cdot \mathbf{v} \tag{2.43}$$

$$\mathbf{v} = \mathbf{L}^{\dagger}\mathbf{E}^{\mathrm{s}} \tag{2.44}$$

where the superscript notation of ^{H} is the Hermitian transpose. Therefore, Pseudo inverse $\mathbf{L}^{\dagger}$ is

$$\mathbf{L}^{\dagger} = \mathbf{L}^{H}\left(\mathbf{L}\mathbf{L}^{H}\right)^{-1}. \tag{2.45}$$

The Pseudo inverse provides a solution, however the inversion may face a problem of ill-conditioning. It is usally observed by a condition number (1), but can be also analyzed in Singular Value Decomposition.

The singular value decomposition of a matrix $\mathbf{L}$ for an under-determined matrix (number of measurements is smaller than number of unknowns $M < N$) yields

$$\mathbf{L} = \mathbf{U}\mathbf{S}\mathbf{V}^H, \tag{2.46}$$

$$= \begin{bmatrix} u_{11} & u_{12} & \dots & u_{1M} \\ u_{21} & u_{22} & \dots & u_{2M} \\ \vdots & \vdots & \ddots & \vdots \\ u_{M1} & u_{M2} & \dots & u_{MM} \end{bmatrix} \cdot \begin{bmatrix} \sigma_1 & 0 & \dots & 0 & \dots & 0 \\ 0 & \sigma_2 & \dots & 0 & \dots & 0 \\ \vdots & \vdots & \ddots & \ddots & \vdots & 0 \\ 0 & 0 & \dots & \sigma_M & \dots & 0 \end{bmatrix} \cdot \begin{bmatrix} v_{11} & v_{12} & \dots & v_{1N} \\ v_{21} & v_{22} & \dots & v_{2N} \\ \vdots & \vdots & \ddots & \vdots \\ v_{N1} & v_{N2} & \dots & v_{NN} \end{bmatrix}^H \tag{2.47}$$

where $\mathbf{U}$ and $\mathbf{V}$ are unitary matrices that satisfy $\mathbf{U}\mathbf{U}^H = \mathbf{I}$ and $\mathbf{V}\mathbf{V}^H = \mathbf{I}$, and $\mathbf{S}$ contains singular values σ_i in diagonal and zeros otherwise. Therefore, the Pseudo inverse of matrix $\mathbf{L}^\dagger$ is

$$\begin{aligned} \mathbf{L}^\dagger &= (\mathbf{U}\mathbf{S}\mathbf{V}^H)(\mathbf{U}\mathbf{S}\mathbf{V}^H\mathbf{V}\mathbf{S}\mathbf{U}^H)^{-1} \\ &= (\mathbf{U}\mathbf{S}\mathbf{V}^H)(\mathbf{U}\mathbf{S}^2\mathbf{U}^H)^{-1} \\ &= \mathbf{V}^H\mathbf{S}^\dagger\mathbf{U} \end{aligned} \tag{2.48}$$

where $\mathbf{S}^{\dagger}$ is pseudo inverse of the matrix $\mathbf{S}$,

$$\mathbf{S}^{\dagger} = \mathbf{S}^{H}\left(\mathbf{S}\mathbf{S}^{H}\right)^{-1}. \tag{2.49}$$

We can easily confirm that dot product of the matrix and Pseudo inverse is the identity matrix, $\mathbf{S}\cdot\mathbf{S}^{\dagger} = \mathbf{I}$ and also $\mathbf{L}\cdot\mathbf{L}^{\dagger} = \mathbf{I}$.

The important point needed to be mentioned is that 2.48 contains the inverse of singular values $\left(\mathbf{S}\mathbf{S}^{H}\right)^{-1}$. This means that small singular value component of matrix $\mathbf{L}$ contributes large amount to the solution of the inverse problem. Therefore, the solution often contains unrealistically large numbers.

2.8.2 Truncated Singular Value Decomposition

Truncated Singular Value Decomposition (TSVD) (92) is used in many articles to overcome the problem of Pseudo inverse. TSVD is categorized as a direct regularization method which attempts to stabilize a system of linear equations by using the Singular Value Decomposition as intermediate step. In TSVD, a regularization parameter is introduced by truncation of the small singular values.

Consider a matrix $\mathbf{L}$ and its singular value decomposition 2.8.1. TSVD removes small singular values by truncating matrices of $\mathbf{U}$, $\mathbf{S}$ and $\mathbf{V}$. The regularized matrix $\tilde{\mathbf{L}}$ contains truncated matrices of $\mathbf{U}$, $\mathbf{S}$ and $\mathbf{V}$.

$$\begin{aligned}\tilde{\mathbf{L}} &= \mathbf{U}_k \mathbf{S}_k \mathbf{V}_k^H \\ &= \begin{bmatrix} u_{11} & u_{12} & \dots & u_{1k} \\ u_{21} & u_{22} & \dots & u_{2k} \\ \vdots & \vdots & \ddots & \vdots \\ u_{M1} & u_{M2} & \dots & u_{Mk} \end{bmatrix} \cdot \begin{bmatrix} \sigma_1 & 0 & \dots & 0 \\ 0 & \sigma_2 & \dots & 0 \\ \vdots & \vdots & \ddots & \vdots \\ 0 & 0 & \dots & \sigma_k \end{bmatrix} \cdot \begin{bmatrix} v_{11} & v_{12} & \dots & v_{1k} \\ v_{21} & v_{22} & \dots & v_{2k} \\ \vdots & \vdots & \ddots & \vdots \\ v_{N1} & v_{N2} & \dots & v_{Nk} \end{bmatrix}^H \end{aligned} \tag{2.50}$$

where k is the number of singular values kept in TSVD inversion. The matrix $\mathbf{L}$ contains M or N numbers of singular values for under-determined or over-determined matrix $\mathbf{L}$. TSVD keeps the matrix component of the corresponding singular values from the largest to k-th, and removes the singular value component from $(k+1)$-th to smallest.

Similar to pseudo inverse, its inverse matrix can be achieved by

$$\tilde{\mathbf{L}}^\dagger = \mathbf{V}_k^H \mathbf{S}_k^{-1} \mathbf{U}_k \tag{2.51}$$

$$\tag{2.52}$$

Even though the matrix is approximated due to the truncation ($\tilde{\mathbf{L}} \approx \mathbf{L}$), the truncation has a big advantage in inverse problems. For Pseudo inverse, small singular value components such as σ_M have large contribution to the solution of inverse problem even though they are negligible

in forward calculation. For TSVD, the smallest singular value components in use is σ_k which is larger than σ_M.

L-curve

This regularization parameter can be obverved in the plot of the L-curve (93). An optimum truncation index N_t is found at a kink of the L curve. This approach provides a good compromise between euclidean norm of a solution $||\mathbf{x}||_2$ and a residual $||\mathbf{b}-\mathbf{A}\mathbf{x}||_2$ for an equation of $\mathbf{b}=\mathbf{A}\cdot\mathbf{x}$.

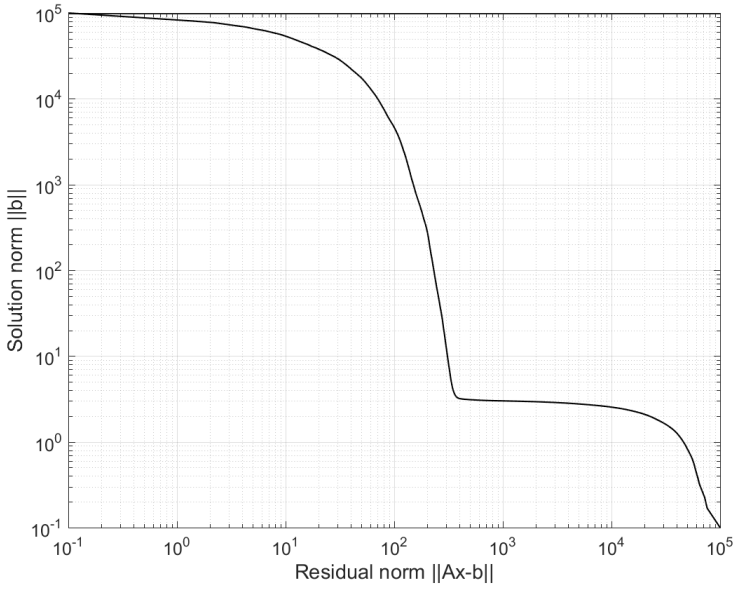

Figure 3: An example of L-curve.

In practice, the kink can be ambiguous when the kink is not sharp. This problem arises when the number of equations is not enough. It also means that the problem occurs when many equations are similar to each other. In the following chapters, entropy is also used to determine optimum regularization parameter in addition to the L-curve.

Spectral Content

The idea of spectral content has been used to observe achievable resolution. In articles (2; 3; 4), the spectral content is defined in term of the norm L^1; however, in this thesis the squared euclidean norm is used because it is easier to associate it with a physical meaning. The spectral content is defined as follow,

$$SC(k_x, k_y) = \sum_{n=1}^{Nt} |v_n(k_x, k_y)|^2, \tag{2.53}$$

$$v_n(k_x, k_y) = \iint_D v_n(x, y) \exp\left[-j(k_x x + k_y y)\right] dxdy, \tag{2.54}$$

where Nt is the number of terms used and v_n is n-th column vector of the decomposed matrix $\mathbf{V}$. A column vector v_n ($N \times 1$ array) is reshaped to the two dimensional image domain ($Nx \times Ny$) in this analysis.

There are several ways to decide Nt for analysis of spectral content. In this thesis, Nt is determined by optimum regularization parameter found by L-curve. In this way, the analysis of the L-curve connects directly to resulting reconstructed images and spectral content.

One reason to change the definition of the spectral content is that by using the euclidean norm, Parseval's theorem is preserved. In articles of (2; 3; 4), spectral content is obtained terms of the L^1 norm,

$$SC(k_x, k_y) = \sum_{n=1}^{Nt} |v_n(k_x, k_y)| . \tag{2.55}$$

On the other hand, because the matrix $\mathbf{V}$ is an unitary matrix, a selected column vector $\mathbf{v}_n$ always satisfies

$$||\mathbf{v}_n||^2 = 1. \tag{2.56}$$

also, recalling Parseval's theorem of one dimensional discrete Fourier transform (DFT) (94),

$$X[k] = \sum_{l=0}^{L-1} x[l] \exp\left[-j\frac{2\pi kn}{P}\right] \tag{2.57}$$

$$\sum_{l=0}^{L-1} |x[l]|^2 = \frac{1}{P} \sum_{k=0}^{P-1} |X[k]|^2 \tag{2.58}$$

where L and P are number of elements in real and Fourier domain, respectively.

For two dimensional problems like the case of spectral content, Parseval's theorem is satisfied according to

$$\sum_x \sum_y |\mathbf{v_n}(x, y)|^2 = \frac{1}{Nk_x \cdot Nk_y} \sum_{k_x} \sum_{k_y} |\mathbf{v}_n(k_x, k_y)|^2 = 1 \tag{2.59}$$

where Nk_x and Nk_y are the size of resulting two dimensional Fourier domain in k_x and k_y axis. In conclusion, the new definition of 2.54 preserve the relationship of

$$\frac{1}{Nt \cdot Nk_x \cdot Nk_y} \sum_{k_x} \sum_{k_y} |SC(k_x, k_y)|^2 = 1. \tag{2.60}$$

2.8.3 Conjugate gradient

The Conjugate Gradient method (95; 96) is a very common technique for inverse problems. This method is categorized as an iterative regularization method which uses the method of steepest descent algorithm. Method of steepest descent algorithm is well covered in (97)

Consider linear equations of $\mathbf{b} = \mathbf{Ax}$, and define a cost function C as

$$C = (\mathbf{b} - Ax)^H(\mathbf{b} - \mathbf{Ax}) = \mathbf{b}^H b - \mathbf{b}^H \mathbf{Ax} - (\mathbf{Ax})^H \mathbf{b} + (\mathbf{Ax})^H(\mathbf{Ax}). \tag{2.61}$$

Notice that the cost function is the squared euclidean norm of the residual and a scalar quantity. The solution can be found by minimizing the cost function.

The next step is to find the direction that has the steepest slope to minimize the cost function. The direction can be found by the gradient of the cost function,

$$\nabla C = 0 - 0 - 2A^H \mathbf{b} + 2\mathbf{A}^H \mathbf{Ax} = -2A^H(\mathbf{b} - \mathbf{Ax}) \tag{2.62}$$

$$\text{where} \quad \nabla \mathbf{x} = \frac{\partial \mathbf{x}}{\mathbf{x}^H} = 0, \quad \nabla \mathbf{x}^H = \frac{\partial \mathbf{x}^H}{\partial \mathbf{x}^H} = 2. \tag{2.63}$$

Therefore, the rule to update the solution according to the conjugate gradient method for RF Tomography $\mathbf{E}^{\mathrm{s}} = \mathbf{L} \cdot \mathbf{v}$ is

$$\mathbf{v}_{new} = \mathbf{v}_{old} - \frac{1}{2}\alpha \nabla C \tag{2.64}$$

$$= \mathbf{v}_{old} + \alpha \mathbf{L}^{H}(\mathbf{E}^{\mathrm{s}} - \mathbf{L} \cdot \mathbf{v}_{old}) \tag{2.65}$$

As long as the iteration step α is small, a solution of the next step $\mathbf{v}_{new}$ has smaller residual norm than the solution of previous step $\mathbf{v}_{old}$ has.

When the gradient ∇C is computed, the direction is found by the steepest descent slope from the previous solution $\mathbf{v}_{old}$. However, it often has the same or very similar direction as the direction of previous iteration had. In the conjugate gradient method, conjugate Gram-Schmidt orthonormalization for residual $\mathbf{E}^{\mathrm{s}} - \mathbf{L} \cdot \mathbf{v}$ is applied to all previous residuals (98; 96). The conjugate Gram-Schmidt orthonormalization process ensures finding orthogonal direction to previously found. More detail can be found in (96).

2.8.4 Algebraic reconstruction technique

Algebraic Reconstruction Technique (ART) (99) is also very popular iterative regularization method. ART can be derived from steepest descent algorithm for a selected equation.

The updating rule of Algebraic Reconstruction Technique is

$$\mathbf{v}_{new} = \mathbf{v}_{old} + \frac{\alpha}{||\mathbf{L}_i||_2^2}\mathbf{L}_i^{H}(E_i - \mathbf{L}_i \cdot \mathbf{v}_{old}). \tag{2.66}$$

where subscript i corresponds to i-th equation. According to stability condition of steepest descent, the iteration step must satisfy $\alpha < 1$ (97), however the algorithm tends to converge too fast and an undesired solution when $\alpha = 1$. In order to avoid such solution, smaller iteration step α must be used. In this thesis, the iteration step are $\alpha = 10^{-4}$ for simulations and $\alpha = 10^{-2}$ for experiments used in chapter 5.

2.8.5 Physical bounds and constraints for iterative regularization method

An advantage of iterative regularization method such as Conjugate Gradient method and Algebraic Reconstruction Technique is to easily introduce constrains for a resulting solution.

In an iterative regularization method, any initial guess of a solution can be used to start from. When the initial guess of solution is very close to the actual solution, the algorithm won't be trapped on undesired solution. Similarly, we may introduce an intermediate guess of solution during the iteration process. When a solution does not make sense for any reason, we can modify the solution to preferred solution as long as the solution converges.

In real world, dielectric permittivity and conductivity are always positive numbers. Recalling matrix of RF Tomography 2.34 and the unknown contrast array 2.25,

$$\mathbf{E}^{\mathrm{s}} = \mathbf{L} \cdot \mathbf{v} \tag{2.67}$$

$$v(\mathbf{r}') = \varepsilon_r(\mathbf{r}') - \varepsilon_b + j\frac{(\sigma(\mathbf{r}') - \sigma_b)}{2\pi f \varepsilon_0}, \tag{2.68}$$

$$\varepsilon_r(\mathbf{r}') \geq 1 \tag{2.69}$$

$$\sigma(\mathbf{r}') \geq 0 \tag{2.70}$$

When background medium is freespace ($\varepsilon_b = \varepsilon_0$), negative real part and real imaginary part of the contrast are unrealistic from physics point of view. In article of (1; 77), the constraints are introduced by enforcing the quantity as

$$\text{if} \quad \text{Re}(\mathbf{v}) < 0 \quad \rightarrow \quad \text{Re}(\mathbf{v}) = |\text{Re}(\mathbf{v})| \tag{2.71}$$

$$\text{if} \quad \text{Im}(\mathbf{v}) > 0 \quad \rightarrow \quad \text{Im}(\mathbf{v}) = -|\text{Im}(\mathbf{v})|. \tag{2.72}$$

This physical bound keeps the solution norm $||\mathbf{v}||_2$, however the residual norm is changed $||\mathbf{E}^{\text{s}} - \mathbf{L} \cdot \mathbf{v}||$ which violates the recursive rule and convergence stability. In conjugate gradient method, Gram-Schmidt process produces correct direction and scaling of projected subspace; therfore, it ensures the convergence (96; 1).

In this thesis a background medium is a concrete in simulations and sand or gravel in experiments, dielectric contrast of a cavity leads to negative real part of the contrast instead. Therefore, in this thesis, physical constraints are applied by the modifications of

$$\text{if} \quad \text{Re}(\mathbf{v}) > 0 \quad \rightarrow \quad \text{Re}(\mathbf{v}) = -|\text{Re}(\mathbf{v})| \tag{2.73}$$

$$\text{if} \quad \text{Im}(\mathbf{v}) > 0 \quad \rightarrow \quad \text{Im}(\mathbf{v}) = -|\text{Im}(\mathbf{v})|. \tag{2.74}$$

The constraints are rational way to reduce the number of possible solutions, and resulting less artifacts in most of cases. The reconstructed images with and without the modifications are shown in Chapter 5.

CHAPTER 3

FORWARD MODEL FOR REINFORCED CONCRETE STRUCTURE

In this chapter, a forward model for reinforced concrete which is made of a circular dielectric cylinder is constructed. A background medium of a circular dielectric cylinder is chosen to represent a supporting pile of a bridge. Inverse problem contains several issues which can affect reconstructed image quality. In order to understand the best achievable reconstructed image under perfect knowledge, exact analytical solutions in cylindrical objects are considered. The Green's functions of RF Tomography forward model will be evaluated exactly by replacing the analytical solutions with an appropriate constant. This test is aimed to identify the reason of artifact in a reconstructed image due to model error or an algorithm.

A forward model of two dimensional structure in 2.37 and its implementation using freespace Green's function are introduced in section 2.7 of the previous chapter. In order to construct a forward model for a circular dielectric cylinder, analytical solutions of a dielectric cylinder are used in this thesis. The analytical solutions are translated into Green's function of forward model, 2.37. This chapter starts with well-known derivation of scattering problems due to a line source two dimensional cylindrical coordinate (100; 101; 89).

3.1 Analytical Solutions

The aimed test geometry contains a Perfect Electric Conductor (PEC) cylinder covered with dielectric coating. Also, cases for only a dielectric cylinder is considered as a special case

of the geometry. Analytical solutions will be different when an incident electric line source is located outside or inside. Analytical solutions are provided for 4 case as shown in Figure 4. Geometry (a) contains a PEC cylinder with dielectric coating when an electric line source is located outside dielectric region. Geometry (b) is considered when a PEC cylinder is removed from geometry (a). Geometry (c) contains geometry of a PEC cylinder with dielectric coating when an electric line source located inside dielectric region. Geometry (d) is considered when a PEC cylinder is removed from geometry (c).

3.1.1 Analytical solution for a line source located at outside of a dielectric cylinder

Geometry (a)

An analytical solution of scattered electric fields from a PEC cylinder with dielectric coating when an electric line source located outside the dielectric region is provided (100; 101; 89). .

An electric line source is located at $(\rho = \rho_s,\ \phi = \phi_s)$, and its electric field in absence of objects in freespace is

$$E_z^i(\rho,\phi) = -\frac{k_0^2 I_e}{4\omega\varepsilon_0} H_0^{(2)}\left(k_0\left|\boldsymbol{\rho}-\boldsymbol{\rho}_s\right|\right), \tag{3.1}$$

or

$$E_z^i(\rho,\phi) = -\frac{k_0^2 I_e}{4\omega\varepsilon_0} \begin{cases} \sum_{n=-\infty}^{\infty} J_n\left(k_0\rho\right) H_n^{(2)}\left(k_0\rho_s\right) e^{jn(\phi-\phi_s)} & \rho \le \rho_s \\ \sum_{n=-\infty}^{\infty} J_n\left(k_0\rho_s\right) H_n^{(2)}\left(k_0\rho\right) e^{jn(\phi-\phi_s)} & \rho \ge \rho_s \end{cases} \tag{3.2}$$

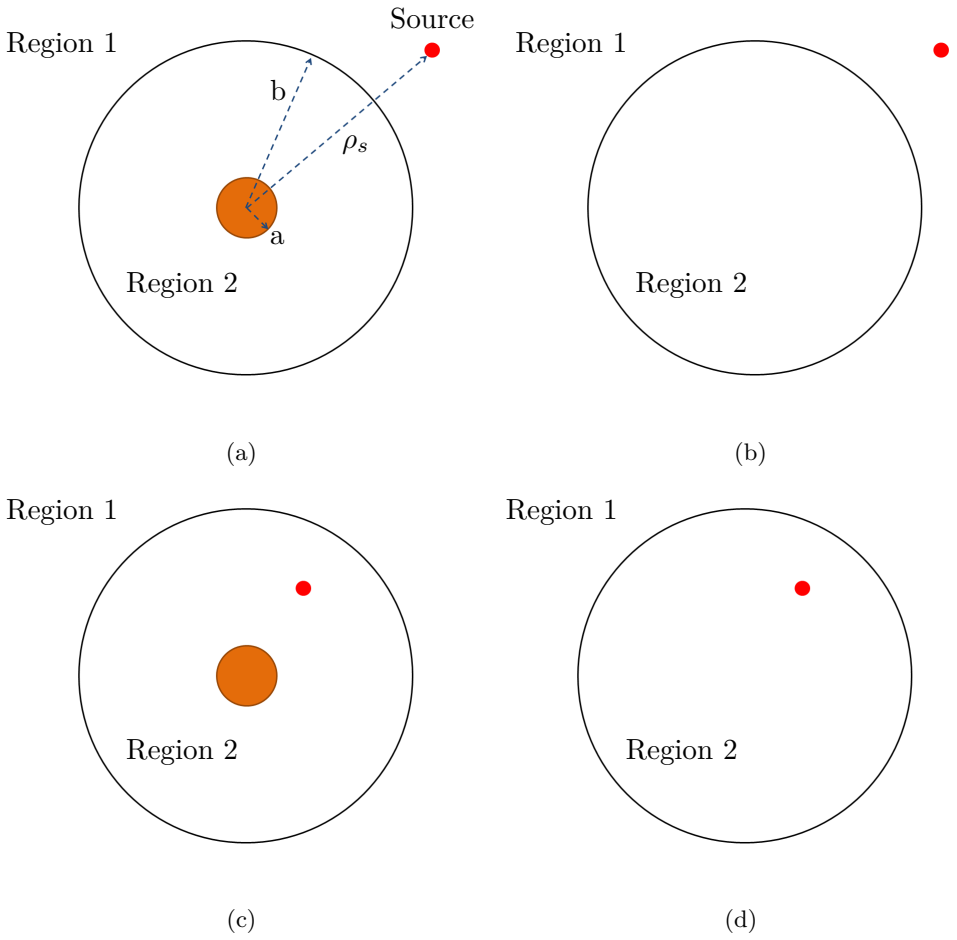

Figure 4: Geometries for analytical solution (a) and (b) geometory correspond to a line source at outside of a dielectric cylinder, and (c) and (d) correspond to a line source at inside of a dielectric cylinder.

where J_n and $H_n^{(2)}$ are Bessel function and Hankel function of 2nd kind.

Because of the presence of the dielectric structure, the scattered electric field is given by

$$E_z^s(\rho,\phi) = -\frac{k_0^2 I_e}{4\omega\varepsilon_0} \sum_{n=-\infty}^{\infty} a_n H_n^{(2)}(k_0\rho)\, e^{jn(\phi-\phi_s)} \quad \rho \geq b \tag{3.3}$$

so that the total electric field in region 1 is $E_z^i + E_z^s$. The electric field in region 2 is

$$E_z^d(\rho,\phi) = -\frac{k_1^2 I_e}{4\omega\varepsilon_1}\sum_{n=-\infty}^{\infty}\left[b_n J_n(k_1\rho) + c_n Y_n(k_1\rho)\right]e^{jn(\phi-\phi_s)} \quad a \le \rho \le b \tag{3.4}$$

where $\varepsilon_1 = \varepsilon_0\varepsilon_r$ and $k_1 = k_0\sqrt{\varepsilon_r\mu_r}$.

The corresponding magnetic field can be found by

$$\mathbf{H} = -\frac{1}{j\omega\mu}\nabla\times\mathbf{E} = -\frac{1}{j\omega\mu}\left(\hat{\rho}\frac{1}{\rho}\frac{\partial E_z}{\partial\phi} - \hat{\phi}\frac{\partial E_z}{\partial\rho}\right). \tag{3.5}$$

Hence the incident magnetic field is

$$H_z^i(\rho,\phi) = -j\frac{I_e}{4}\begin{cases}\displaystyle\sum_{n=-\infty}^{\infty} H_n^{(2)}(k_0\rho_s)\left[\hat{\rho}\frac{jn}{\rho}J_n(k_0\rho) - \hat{\phi}k_0 J_n'(k_0\rho)\right]e^{jn(\phi-\phi_s)} & \rho \le \rho_s \\ \displaystyle\sum_{n=-\infty}^{\infty} J_n(k_0\rho_s)\left[\hat{\rho}\frac{jn}{\rho}H_0^{(2)}(k_0\rho) - \hat{\phi}H_0^{(2)\prime}(k_0\rho)\right]e^{jn(\phi-\phi_s)} & \rho \ge \rho_s\end{cases}, \tag{3.6}$$

note $k^2/(\omega^2\varepsilon\mu) = 1$.

The scattered magnetic field in region 1 is

$$H_z^s(\rho,\phi) = -j\frac{I_e}{4}\sum_{n=-\infty}^{\infty} a_n\left[\hat{\rho}\frac{jn}{\rho}H_n^{(2)}(k_0\rho) - \hat{\phi}k_0 H_n^{(2)\prime}(k_0\rho)\right]e^{jn(\phi-\phi_s)} \quad \rho \ge b, \tag{3.7}$$

where the prime symbol means derivative with respect to the argument of the function.

The magnetic field inside the dielectric region is

$$H_z^d(\rho,\phi) = -j\frac{I_e}{4}\sum_{n=-\infty}^{\infty}\Big[\hat{\rho}\frac{jn}{\rho}\left[b_n J_n\left(k_1\rho\right)+c_n Y_n\left(k_1\rho\right)\right] \\ -\hat{\phi}k_1\left[b_n J_n'\left(k_1\rho\right)+c_n Y_n'\left(k_1\rho\right)\right]\Big]e^{jn(\phi-\phi_s)} \quad a\le\rho\le b. \tag{3.8}$$

There are three boundary conditions to find the modal coefficients a_n, b_n and c_n. The electric field must be zero at $\rho = a$

$$E_z^d\Big|_{\rho=a} = 0 \tag{3.9}$$

$$0 = -\frac{k_1^2 I_e}{4\omega\varepsilon_1}\sum_{n=-\infty}^{\infty}\left[b_n J_n\left(k_1 a\right)+c_n Y_n\left(k_1 a\right)\right]e^{jn(\phi-\phi_s)} \tag{3.10}$$

$$\boxed{b_n J_n\left(k_1 a\right)+c_n Y_n\left(k_1 a\right)=0} \tag{3.11}$$

The continuity of electric field at $\rho = b$ gives

$$\left(E_z^i+E_z^s\right)\Big|_{\rho=b} = E_z^d\Big|_{\rho=b} \tag{3.12}$$

$$-\frac{k_0^2 I_e}{4\omega\varepsilon_0}\sum_{n=-\infty}^{\infty}\left[J_n\left(k_0 b\right)H_n^{(2)}\left(k_0\rho_s\right)+a_n H_n^{(2)}\left(k_0 b\right)\right]e^{jn(\phi-\phi_s)} \\ = -\frac{k_1^2 I_e}{4\omega\varepsilon_1}\sum_{n=-\infty}^{\infty}\left[b_n J_n\left(k_1 b\right)+c_n Y_n\left(k_1 b\right)\right]e^{jn(\phi-\phi_s)} \tag{3.13}$$

$$\boxed{J_n\left(k_0 b\right)H_n^{(2)}\left(k_0\rho_s\right)+a_n H_n^{(2)}\left(k_0 b\right)=\mu_r\left[b_n J_n\left(k_1 b\right)+c_n Y_n\left(k_1 b\right)\right]} \tag{3.14}$$

The continuity of magnetic field at $\rho = b$ gives

$$\left(H_\phi^i + H_\phi^s\right)\Big|_{\rho=b} = H_\phi^d\Big|_{\rho=b} \tag{3.15}$$

$$-j\frac{k_0 I_e}{4}\sum_{n=-\infty}^{\infty}\left[J_n'(k_0 b)\,H_n^{(2)}(k_0\rho_s) + a_n H_n^{(2)\prime}(k_0 b)\right]e^{jn(\phi-\phi_s)}$$

$$= -j\frac{k_1 I_e}{4}\sum_{n=-\infty}^{\infty}\left[b_n J_n'(k_1 b) + c_n Y_n'(k_1 b)\right]e^{jn(\phi-\phi_s)} \tag{3.16}$$

$$\boxed{J_n'(k_0 b)\,H_n^{(2)}(k_0\rho_s) + a_n H_n^{(2)\prime}(k_0 b) = \sqrt{\varepsilon_r\mu_r}\left[b_n J_n'(k_1 b) + c_n Y_n'(k_1 b)\right]} \tag{3.17}$$

Those boundary conditions can be represented as matrix

$$\begin{pmatrix} 0 & J_n(k_1 a) & Y_n(k_1 a) \\ H_n^{(2)}(k_0 b) & -\mu_r J_n(k_1 b) & -\mu_r Y_n(k_1 b) \\ H_n^{(2)\prime}(k_0 b) & -\sqrt{\varepsilon_r\mu_r}J_n'(k_1 b) & -\sqrt{\varepsilon_r\mu_r}Y_n'(k_1 b) \end{pmatrix}\begin{pmatrix} a_n \\ b_n \\ c_n \end{pmatrix} = \begin{pmatrix} 0 \\ -J_n(k_0 b)\,H_n^{(2)}(k_0\rho_s) \\ -J_n'(k_0 b)\,H_n^{(2)}(k_0\rho_s) \end{pmatrix} \tag{3.18}$$

The modal coefficients must be found by inverting the matrix. The derivative of Bessel and Hankel functions is

$$\frac{\partial}{\partial(k\rho)}Z_n(k\rho) = -Z_{n+1}(k\rho) + \frac{n}{k\rho}Z_n(k\rho) \tag{3.19}$$

Geometry (b)

The scattered field from only the dielectric cylinder when an electric line source is located outside the dielectric region is considered. The solution can be found as simple case of previous case.

The boundary at $\rho = a$ does not exist, also coefficient the modal coefficient c_n must be zero due to singularity of Bessel function of second kind at $\rho = 0$. Therefore, the new modal coefficients must satisfy the matrix equations

$$\begin{pmatrix} H_n^{(2)}(k_0 b) & -\mu_r J_n(k_1 b) \\ H_n^{(2)\prime}(k_0 b) & -\sqrt{\varepsilon_r \mu_r} J_n'(k_1 b) \end{pmatrix} \begin{pmatrix} a_n \\ b_n \end{pmatrix} = \begin{pmatrix} -J_n(k_0 b) H_n^{(2)}(k_0 \rho_s) \\ -J_n'(k_0 b) H_n^{(2)}(k_0 \rho_s) \end{pmatrix}. \tag{3.20}$$

3.1.2 Analytical solution for a line source located at inside of a dielectric cylinder

Geometry (c)

An analytical solution of scattered electric field from a PEC cylinder with dielectric coating when an electric line source located inside the dielectric region is provided.

The field expressions are very similar to previous except parameter must be changed according to materials, $k_0 \to k_1$ and $\varepsilon_0 \to \varepsilon_1$. The total electric and magnetic fields are E_z^s and H_z^s outside the dielectric while $E_z^i + E_z^d$ and $H_z^i + H_z^d$ inside dielectric. Therefore, the modal coefficients must changed from the previous problem. Specifically, the electric field at $\rho = a$ must be zero,

$$E_z^i + E_z^d\Big|_{\rho=a} = 0 \tag{3.21}$$

$$0 = -\frac{k_1^2 I_e}{4\omega\varepsilon_1} \sum_{n=-\infty}^{\infty} \left[J_n(k_1 a) H_n^{(2)}(k_1\rho_s) + b_n J_n(k_1 a) + c_n Y_n(k_1 a) \right] e^{jn(\phi-\phi_s)} \tag{3.22}$$

$$\boxed{b_n J_n(k_1 a) + c_n Y_n(k_1 a) = -J_n(k_1 a) H_n^{(2)}(k_1\rho_s)} \tag{3.23}$$

The continuity of the tangential electric field at $\rho = b$ gives

$$E_z^i + E_z^d\Big|_{\rho=b} = E_z^s|_{\rho=b} \tag{3.24}$$

$$-\frac{k_1^2 I_e}{4\omega\varepsilon_1}\sum_{n=-\infty}^{\infty}\left[J_n(k_1\rho_s)H_n^{(2)}(k_1 b) + b_n J_n(k_1 b) + c_n Y_n(k_1 b)\right]e^{jn(\phi-\phi_s)}$$

$$= -\frac{k_0^2 I_e}{4\omega\varepsilon_0}\sum_{n=-\infty}^{\infty} a_n H_n^{(2)}(k_0 b)\, e^{jn(\phi-\phi_s)} \tag{3.25}$$

$$\boxed{-a_n H_n^{(2)}(k_0 b) + \mu_r\left[b_n J_n(k_1 b) + c_n Y_n(k_1 b)\right] = -\mu_r J_n(k_1\rho_s)H_n^{(2)}(k_1 b)} \tag{3.26}$$

The continuity of the tangential electric field at $\rho = b$ gives

$$H_z^i + H_z^d\Big|_{\rho=b} = H_z^s|_{\rho=b} \tag{3.27}$$

$$-j\frac{k_1 I_e}{4}\sum_{n=-\infty}^{\infty}\left[J_n(k_1\rho_s)H_n^{(2)\prime}(k_1 b) + b_n J_n'(k_1 b) + c_n Y_n'(k_1 b)\right]e^{jn(\phi-\phi_s)}$$

$$= -j\frac{k_0 I_e}{4}\sum_{n=-\infty}^{\infty} a_n H_n^{(2)\prime}(k_0 b)\, e^{jn(\phi-\phi_s)} \tag{3.28}$$

$$\boxed{-a_n H_n^{(2)\prime}(k_0 b) + \sqrt{\varepsilon_r\mu_r}\left[b_n J_n'(k_1 b) + c_n Y_n'(k_1 b)\right] = -\sqrt{\varepsilon_r\mu_r}J_n(k_1\rho_s)H_n^{(2)\prime}(k_1 b)} \tag{3.29}$$

These boundary conditions can be arranged as matrix

$$\begin{pmatrix} 0 & J_n(k_1 a) & Y_n(k_1 a) \\ -H_n^{(2)}(k_0 b) & \mu_r J_n(k_1 b) & \mu_r Y_n(k_1 b) \\ -H_n^{(2)\prime}(k_0 b) & \sqrt{\varepsilon_r\mu_r}J_n'(k_1 b) & \sqrt{\varepsilon_r\mu_r}Y_n'(k_1 b) \end{pmatrix}\begin{pmatrix} a_n \\ b_n \\ c_n \end{pmatrix} = \begin{pmatrix} -J_n(k_1 a)H_n^{(2)}(k_1\rho_s) \\ -\mu_r J_n(k_1\rho_s)H_n^{(2)}(k_1 b) \\ -\sqrt{\varepsilon_r\mu_r}J_n(k_1\rho_s)H_n^{(2)\prime}(k_1 b) \end{pmatrix} \tag{3.30}$$

Geometry (d)

Scattering from only the dielectric cylinder when an electric line source is located inside the dielectric region is considered. The solution can be found as simple case of previous case.

The boundary at $\rho = a$ does not exist, also the modal coefficient c_n must be zero due to singularity of Bessel function of second kind at $\rho = 0$. Therefore, the modal coefficients must satisfy the matrix equations

$$\begin{pmatrix} -H_n^{(2)}(k_0 b) & \mu_r J_n(k_1 b) \\ -H_n^{(2)\prime}(k_0 b) & \sqrt{\varepsilon_r \mu_r} J_n'(k_1 b)) \end{pmatrix} \begin{pmatrix} a_n \\ b_n \end{pmatrix} = \begin{pmatrix} -\mu_r J_n(k_1 \rho_s) H_n^{(2)}(k_1 b) \\ -\sqrt{\varepsilon_r \mu_r} J_n(k_1 \rho_s) H_n^{(2)\prime}(k_1 b) \end{pmatrix}. \tag{3.31}$$

3.2 Forward model for reinforced concrete

The forward model for reinforced concrete is constructed from the analytical solutions found in the previous section. Consider Equation 2.37 for a cylindrical background relative permittivity ε_b and k_b. The corresponding incident field $E_z^i(\boldsymbol{\rho}^{\mathrm{t}},\boldsymbol{\rho}^{\mathrm{r}})$ and Green's function $g_e(\boldsymbol{\rho}^{\mathrm{r}},\boldsymbol{\rho}';k_b)$ are found from the solution of geometry (b). Let us define the notation for the locations in cylindrical coordinates as $\boldsymbol{\rho}'(\rho',\phi')$, $\boldsymbol{\rho}^{\mathrm{t}}(\rho^t,\phi^t)$ and $\boldsymbol{\rho}^{\mathrm{r}}(\rho^r,\phi^r)$.

In the construction of forward model, the scattered field due to the dielectric cylinder is part of the incident field. The incident field of 2.37 is found by 3.3 when a source and observations are located at TX ($\boldsymbol{\rho}^{\mathrm{t}}$) and RX ($\boldsymbol{\rho}^{\mathrm{r}}$),

$$E_z^i(\boldsymbol{\rho}^{\mathrm{r}},\boldsymbol{\rho}^{\mathrm{t}}) = -\frac{k_0^2 I_e}{4\omega\varepsilon_0}\left[H_0^{(2)}\left(\beta_0\left|\boldsymbol{\rho}^{\mathrm{r}}-\boldsymbol{\rho}^{\mathrm{t}}\right|\right)+\sum_{n=-\infty}^{\infty} a_n H_n^{(2)}\left(k_0\rho^r\right)e^{jn\left(\phi^r-\phi^t\right)}\right]. \tag{3.32}$$

One may realize that the incident field defined here contains the incident field for freespace and scattered field due to the dielectric cylinder. By this consideration, the scattered field due to the dielectric cylinder is not a part of the anomaly which is expressed by ε_δ of Equation 2.37, and reconstructed as an image in RF Tomography.

Also, the Green's function $g_e(\boldsymbol{\rho}',\boldsymbol{\rho}^{\mathrm{t}};k_b)$ is found by

$$\begin{aligned} g_e(\boldsymbol{\rho}',\boldsymbol{\rho}^{\mathrm{t}};k_b) &= \frac{j}{\omega\mu I_e}E_z^d(\boldsymbol{\rho}',\boldsymbol{\rho}^{\mathrm{t}}) \\ &= -j\frac{k_1^2}{4\omega^2\varepsilon_1\mu_0}\sum_{n=-\infty}^{\infty} b_n J_n\left(k_1\rho'\right)e^{jn\left(\phi'-\phi^t\right)}, \end{aligned} \tag{3.33}$$

similarly, use of reciprocity provides Green's function of opposite direction,

$$\begin{aligned} g_e(\boldsymbol{\rho}^{\mathrm{r}},\boldsymbol{\rho}';k_b) &= \frac{j}{\omega\mu I_e} E_z^d(\boldsymbol{\rho}',\boldsymbol{\rho}^{\mathrm{r}}) \\ &= -j\frac{k_1^2}{4\omega^2\varepsilon_1\mu_0} \sum_{n=-\infty}^{\infty} b_n J_n\left(k_1\rho'\right) e^{jn(\phi'-\phi^r)}. \end{aligned} \tag{3.34}$$

Those Green's functions are used to implement the forward model Equation 2.37,

$$E_z^t(\boldsymbol{\rho}^{\mathrm{r}},\boldsymbol{\rho}^{\mathrm{t}}) = E_z^i(\boldsymbol{\rho}^{\mathrm{r}},\boldsymbol{\rho}^{\mathrm{t}}) + k_0^2 \iint_D g_e(\boldsymbol{\rho}^{\mathrm{r}},\boldsymbol{\rho}';k_b)\varepsilon_\delta(\boldsymbol{\rho}')E_z^i(\boldsymbol{\rho}',\boldsymbol{\rho}^{\mathrm{t}})d\boldsymbol{\rho}' \tag{3.35}$$

where the term $E_z^i(\boldsymbol{\rho}',\boldsymbol{\rho}^{\mathrm{t}})$ is still based on the Born approximation $E_z^t(\boldsymbol{\rho}',\boldsymbol{\rho}^{\mathrm{t}}) \approx E_z^i(\boldsymbol{\rho}',\boldsymbol{\rho}^{\mathrm{t}})$, and linear system matrix $\mathbf{L}$ is produced from 2.7. This forward model takes into account propagation of electromagnetic waves in homogeneity due to presence of the dielectric cylinder.

CHAPTER 4

RESOLUTION ANALYSIS

This chapter is dedicated to analyze resolutions of the three configurations, Case 1: Multi-Monostatic/Muti-frequency, Case 2:Multi-static/Single-frequency and Case 3: Multi-static/Multi-frequency configurations. The Case 1 corresponds to configuration of Ground Penetrating Radar while Cases 2 and 3 corresponds to configuration of RF Tomography. The system matrices **L** are produced from the forward model found in chapter 3 which use the Born approximation. The resolution analysis focuses only on the system matrices as mathematical point of view. In order to achieve the purpose, scattered field data is produced from the forward calculation of the system matrices rather than using actual electromagnetic scattered field manipulation. This consideration removes the level of complexity due to electromagnetics and Born approximation.

The background medium assumed in this thesis is a circular dielectric cylinder, which is different from the homogeneous background medium assumed in the analyses performed in many other articles, such as in (2; 3; 4; 5). RF Tomography for homogeneous background medium has better quality of reconstructed images in a higher operating frequency. On the other hand, when the background medium is inhomogeneous, the bounded medium produce unique electric field distributions depending on choice of operating frequencies. The consideration is very important because the reconstruction of RF Tomography sometimes fails when improper operating frequency is used for the system matrix **L**. In reality, it also depend on geometry such

as shape and size of background medium and its permittivity. This leads to the importance of implementing multiple frequencies in RF Tomography.

Figure 5 shows (a) a image of cross section and (b) and ideal image used in resolution analysis. The background dielectric cylinder has a 20 cm radius, and its material properties are given by $\varepsilon_r = 4$ and $\sigma = 0.005$ S/m. The dielectric cylinder represents a pile made of reinforced concrete. The black line indicates the background dielectric cylinder and an area under investigation which is partitioned with a square pixel of 1 cm. Total number of unknowns is 1681. Figure 5 (b) is the ideal image used in resolution analysis.

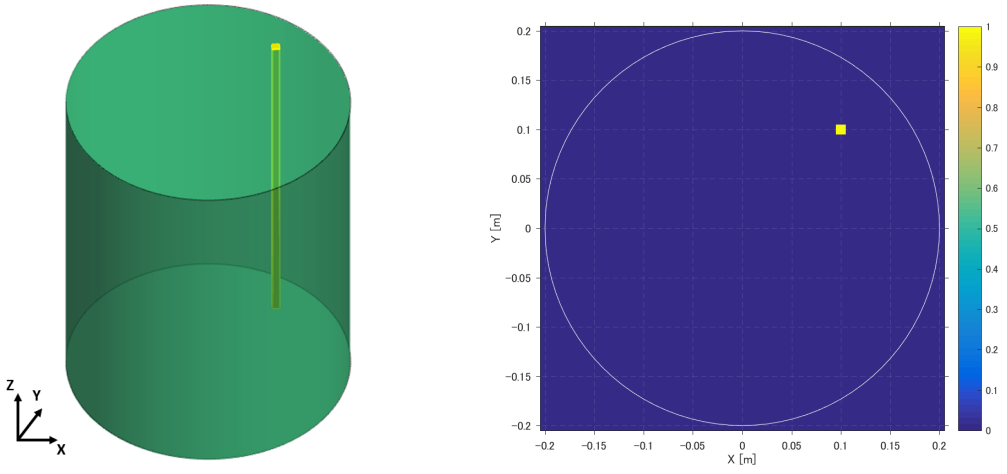

(a) (b)

Figure 5: Geometry of resolution analysis, (a) schematic cross section of the geometry (b) an ideal images used to produce scattered field $\mathbf{E}^s$ for resolution analysis.

The procedure of the resolution analysis is as follows.

1. Produce system matrix $\mathbf{L}$ for a forward model for reinforced concrete.
2. provide an ideal image $\mathbf{v_{ideal}}$ which contains a contrast of one at a pixel (10,10) cm and zeros otherwise.
3. Find $\mathbf{E}^{s}_{ideal}$ by forward calculation of $\mathbf{L} \cdot \mathbf{v_{ideal}}$
4. Add Additive White Gaussian Noise (AWGN) to the $\mathbf{E}^{s}_{ideal}$, where the Signal to Noise Ratio (SNR) is defined with respect to the power of the $\mathbf{E}^{s}_{ideal}$. The SNRs are chosen to be -10, 10 and 30 dB.
5. Plot L-curves and identify their corner of curves and determine optimum regularization parameter. In TSVD scheme, the optimum regularization parameter is the number of terms used to obtain reconstructed images and also Spectral content for this analysis. Therefore, Pont Spread Function and Spectral Content are directly related for later step.
6. Reconstruct point spread function (PSF) $\mathbf{v_{psf}}$ using TSVD for the optimum regularization parameter found from the L curve.
7. Normalize $\mathbf{v_{psf}}$ with its maximum and plot PSF image. Entropy is evaluated to compare quality of images quantitatively.
8. Plot spectral content for the number of terms found from L-curve.

4.1 Test 1: Same number of Tx, Rx and frequency values

There are 41 transmitting line sources (TX) and 41 observations (RX)located along the circumference of the dielectric cylinder at a radius of 21 cm and 20.9 cm respectively as shown

in Figure 6. In the figure, locations of transmitters and receivers are indicated as blue square and red star while the black line represents dielectric cylinder. Operating frequencies are from 1000 MHz to 3000 MHz with increment of 50 MHz. The frequency range is commonly used in Ground Penetrating Radar because it is good compromise between resolution and penetration. From the set of measurements, following three configurations are produced.

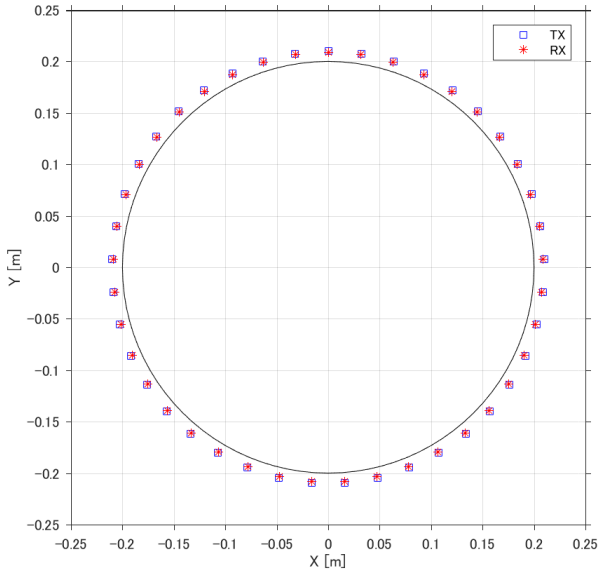

Figure 6: Locations of line source (TX) and observation (RX) for Tests 1 and 2 indicated as blue squares and red stars, respectively. The black circle indicates the Domain of Investigation (DoI).

Case 1: Multi-Monostatic/Muti-frequency configuration

This configuration corresponds to the typical configuration used for Ground Penetrating Radar. The measurements are limited to many mono-static measurements, which means TX and RX are collocated. All available frequencies are used in this configuration. In this, configuration, total number of measurements are 41 positions $\times$ 41 frequencies, 1681 measurements.

Case 2: Multi-static/Single-frequency configuration

This configuration use all combination of transmitters and receivers, however frequency is limited to a single frequency. In this, configuration, total number of measurements are $41 \times 41 = 1681$ measurements.

Case 3: Multi-static/Multi-frequency configuration

This configuration uses all available measurements. All combination of transmitters, receivers and frequencies are used.In this, configuration, total number of measurements are $41 \times 41 \times 41 = 68921$ measurements.

4.1.1 Pretest: Frequency choice for Multi-static/Single-frequency configuration

Best frequency choice for Case 2: Multi-static/Single-frequency configuration is discussed in this section. For analysis, ill condition number, incident electric field, L-curve and point spread function are compared for different frequencies.

Condition number

Condition number for Case 2 in different frequencies is shown in Figure 7. Highest frequency is normally best frequency choice when background medium is homogeneous, however not necessary true for an inhomogeneous background medium. Condition number shows how sensitive a solution is with respect changes or errors of the input. The matrix **L** is ill-conditioned when condition number is large while the matrix **L** is well-conditioned when condition number is small. The condition number is calculated for Pseudo Inverse sense using all singular values terms, and same behavior is expected when Truncated Singular Value Decomposition is used to improve the ill conditioning. When background is homogeneous, highest frequency 3 GHz has smallest condition number thus is the best choice of frequency. On the other hand, when background is inhomogeneous, highest frequency is not the best choice of frequency. Even though the tendency that higher frequency provides smaller condition number, the condition number is fluctuating over frequency. According to Figure 7, 2.9 GHz is best choice of frequency for this test.

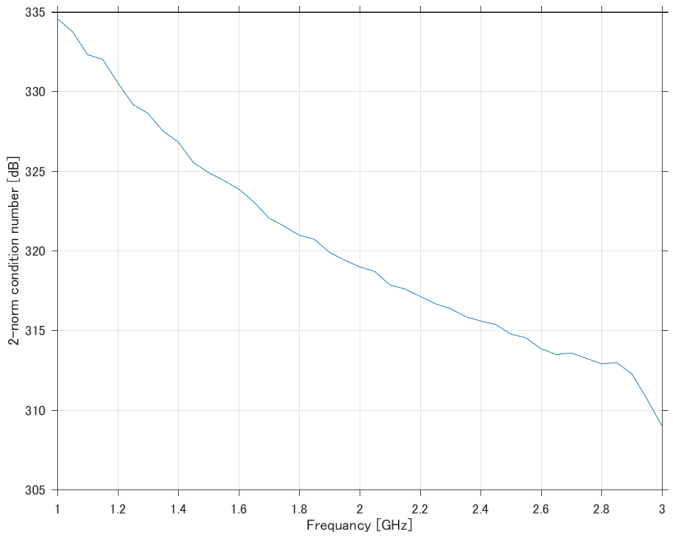

(a)

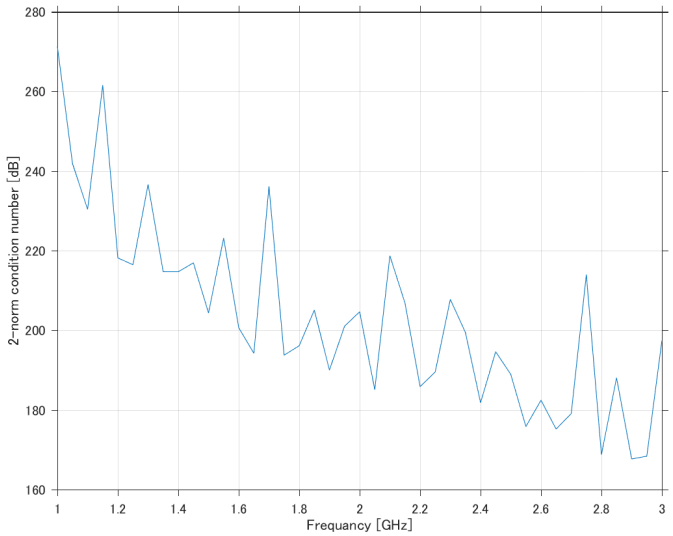

(b)

Figure 7: Condition number of matrix **L** for Case 2, Test 1 (a) when background is homogeneous (b) when background is inhomogeneous.

Electric field distribution

A electric field distribution in a homogeneous medium due to a source is simply a decaying behavior from a source while field distributions of bounded medium like the forward model of reinforced concrete must depend on frequencies. Electric field distribution for six highest frequencies are shown in Figure 8 where the transmitter is located at (0, 21) cm. The field distribution of bounded medium like the forward model of reinforced concrete must have standing wave behavior depending on frequency. The electric field distribution in 2750, 2850 and 3000 MHz have null inside the dielectric cylinder, and the null region is not observable. Also, those frequency with null field must be related to frequencies with high condition number observed in previous analysis. This suggests us to avoid the use of resonating frequencies for a geometry for tomographic purpose.

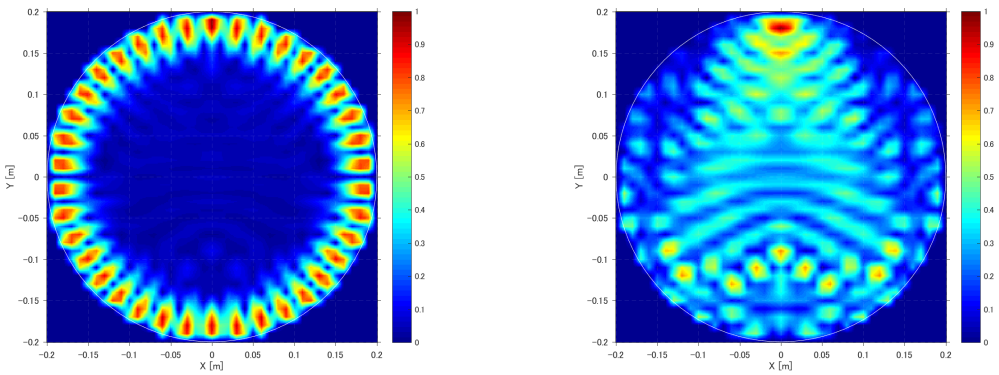

(a)

(b)

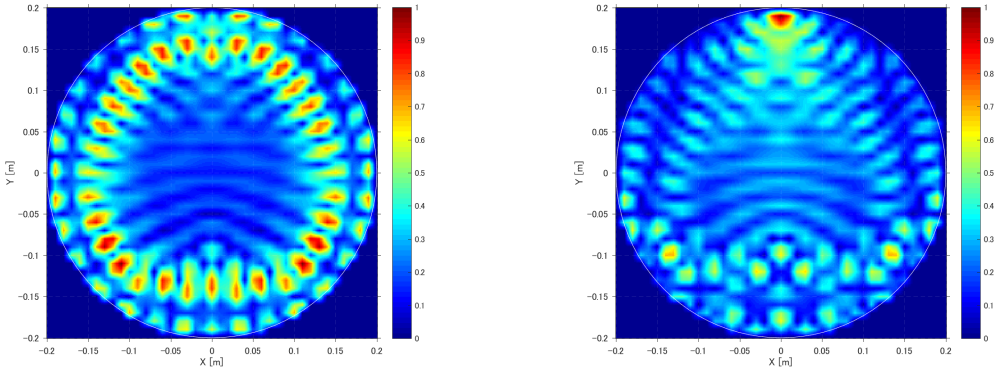

(c)

(d)

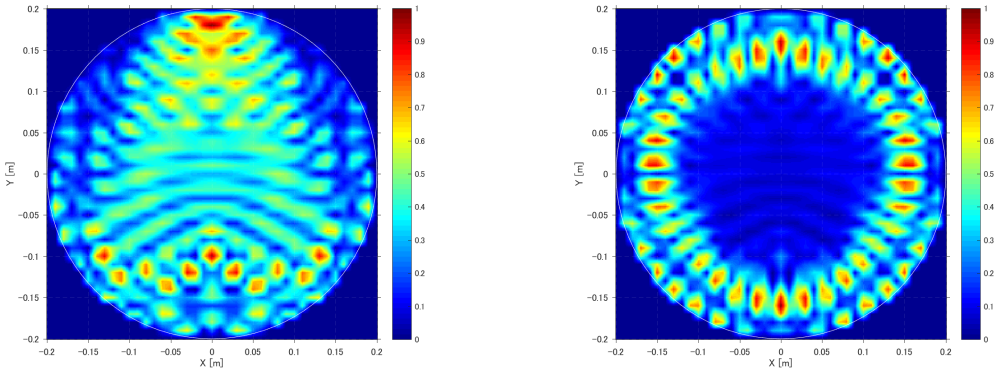

(e)

(f)

Figure 8: Electric field distribution due to first transmitter located at $(0, 21)$ cm for frequencies of (a) 2750MHz, (b) 2800MHz, (c) 2850MHz, (d) 2900MHz, (e) 2950MHz , (f) 3000MHz.

L-curve and singular values

L-curve and singular values are plotted for each frequency in Figure 9. The kink of L-curve indicates the optimum regularization parameter. The kinks are located at smaller residual norm $||\mathbf{Lv} - \mathbf{E}^s||$ for 2800, 2900 and 2950 MHz while the corners are located at large number of the residual norm for 2750, 2850 and 3000 MHz. The resulting residual norm at the kink is the error for TSVD scheme, and large residual norm means failure of reconstruction. The frequencies with large residual norm have large condition number as discussed before. On the other hand, frequencies with large residual norm have larger singular values for at first 200 than the other frequencies. This indicates only those first 200 singular values and associated equations are useful to represent full matrix $\mathbf{L}$, and following smaller singular values are negligible. This is exactly meaning of ill conditioning which has difficulty of inversion due to those small singular values.

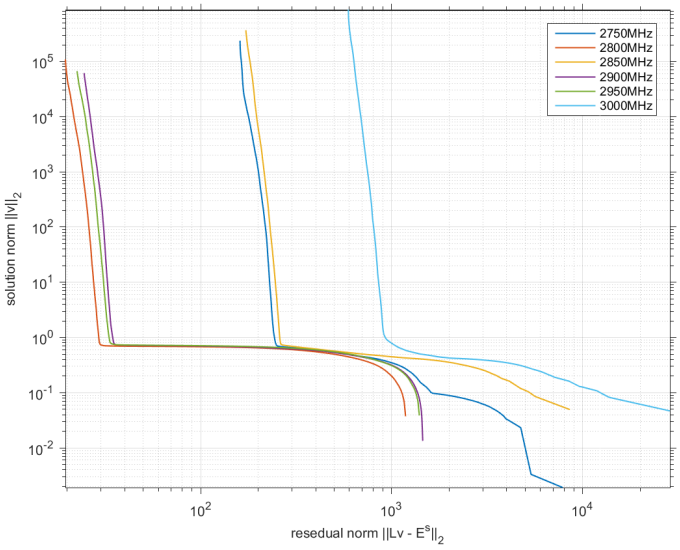

(a)

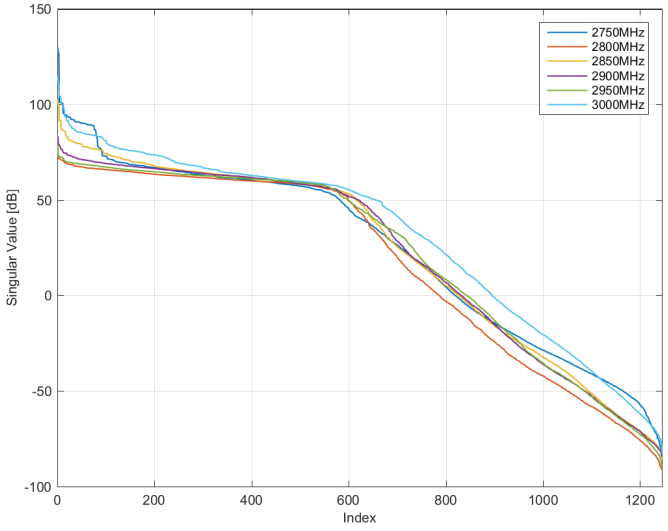

(b)

Figure 9: For Case 2 of Test 1 (a) L-curves when AWGN of SNR = 30dB is added, (b) Singular values .

Point spread function

The resulting point spread function for each frequency is shown in Figure 10 through Figure 12. The point spread function is found based on minimum Entropy.

$$E = -\sum_{n=1}^{N} ss(x_q, y_q) ln[ss(x_q, y_q)], \tag{4.1}$$

$$ss(x_n, y_n) = |\mathbf{x_{psf}}(x_q, y_q)|^2 / \sum_{n=1}^{N} |\mathbf{x_{psf}}(x_n, y_n)|^2. \tag{4.2}$$

Kink of L-curve is usually used to identify an optimum regularization parameter; however, they are often ambiguous when the kink are not sharp. On the other hand, entropy of point spread function is a deterministic number that can be easily minimized. In fact, when image reconstruction is successful, reconstructed images for minimum entropy scheme and the kink of L-curve scheme are very similar. As we found large condition number and residual norm at frequencies of 2750, 2850 and 3000 MHz, resulting point spread functions have a lot of artifacts. The resulting PSF at 2950 MHz looks better than PSF at 2900 MHz, however, I would expect the PSF will be changed if the target is located at different position.

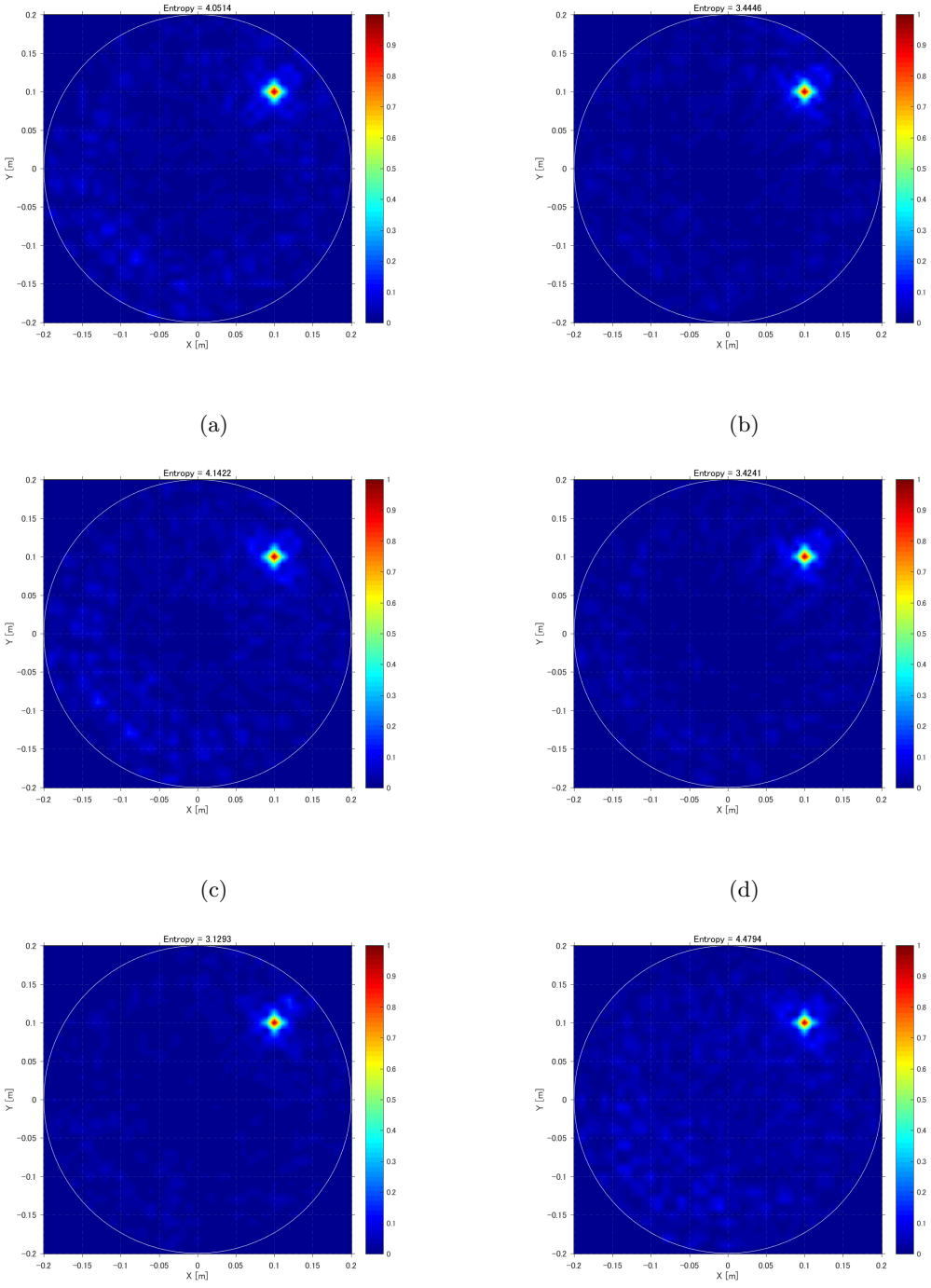

(a) (b) (c) (d) (e) (f)

Figure 10: Point spread functions of Case 2 for frequencies of (a) 2750MHz, (b) 2800MHz, (c) 2850MHz, (d) 2900MHz, (e) 2950MHz , (f) 3000MHz when AWGN of SNR = 30dB are added to $\mathbf{E}^{s}$.

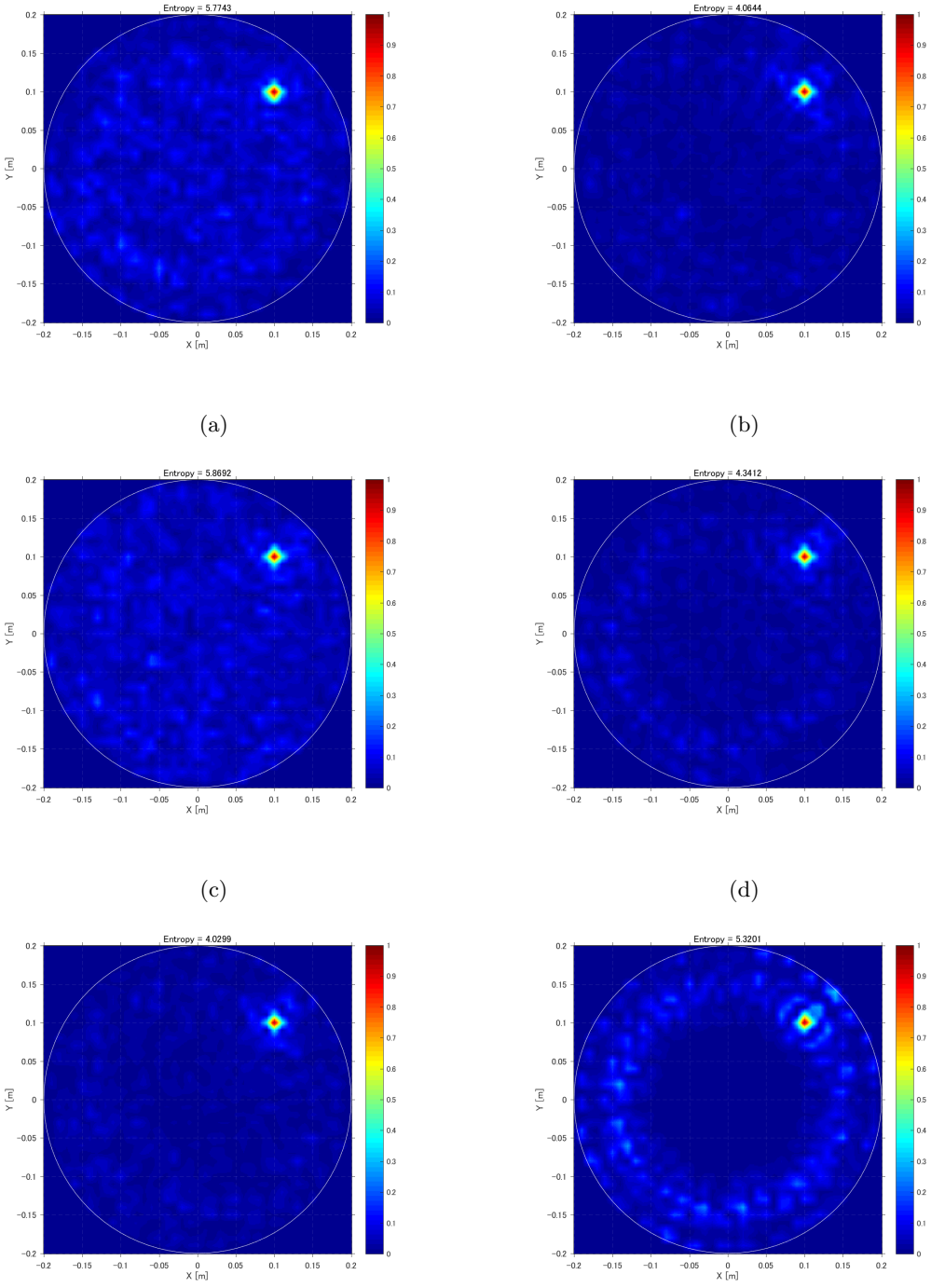

(a) (b)

(c) (d)

(e) (f)

Figure 11: Point spread functions of Case 2 for frequencies of (a) 2750MHz, (b) 2800MHz, (c) 2850MHz, (d) 2900MHz, (e) 2950MHz , (f) 3000MHz when AWGN of SNR = 10dB are added to $\mathbf{E}^{\mathrm{s}}$.

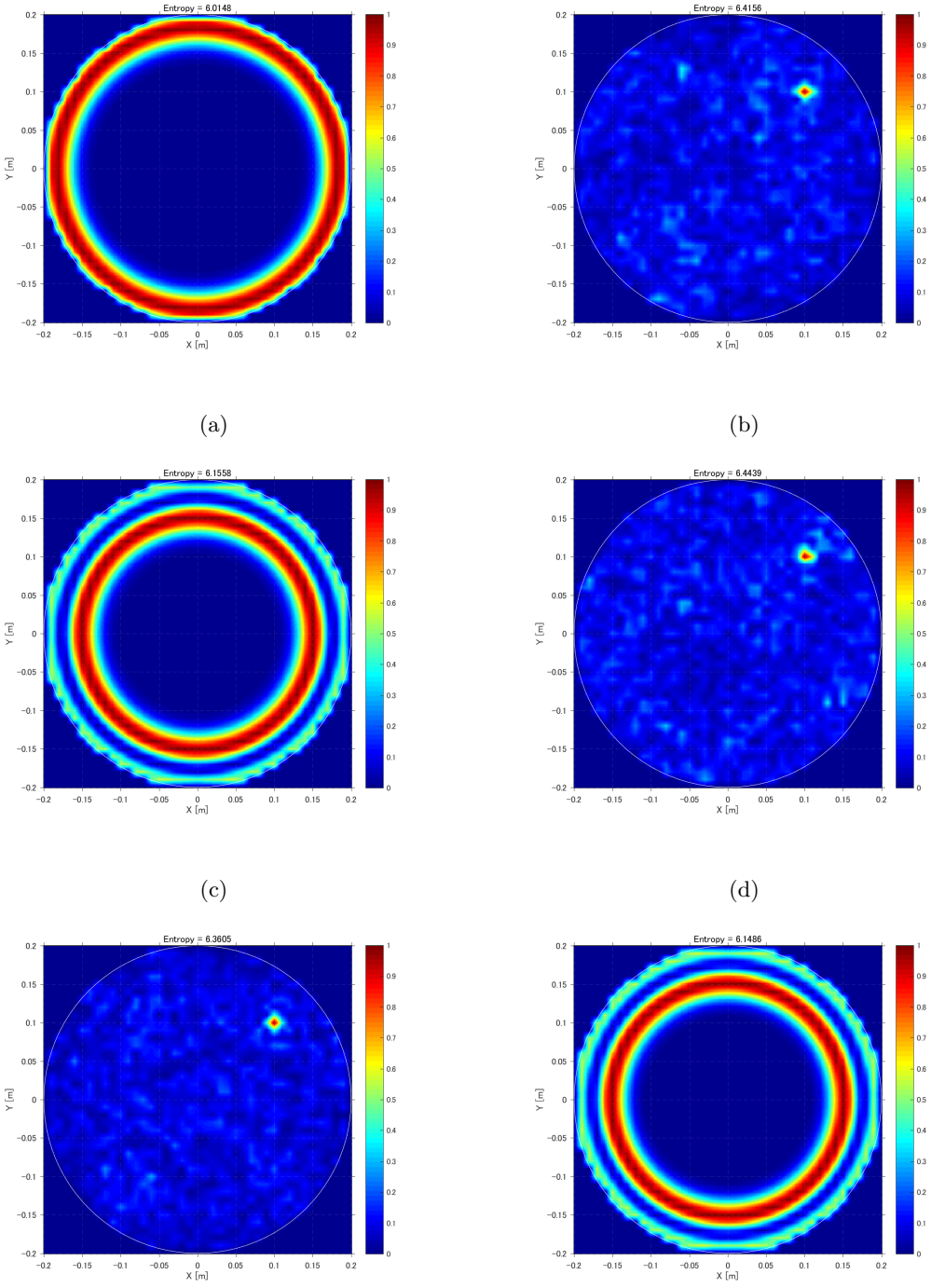

(a) (b)

(c) (d)

(e) (f)

Figure 12: Point spread functions of Case 2 for frequencies of (a) 2750MHz, (b) 2800MHz, (c) 2850MHz, (d) 2900MHz, (e) 2950MHz , (f) 3000MHz when AWGN of SNR = -10dB are added to $\mathbf{E}^{s}$.

From the analysis on the condition number, the electric field distribution, the L-curve and the point spread function, it was determined that 2900 MHz is the best choice of frequency. One might read the minimum residual norm at 2800 MHz from the L-curves, and the best result at 2950 MHz from point spread function, however they must depend on the ideal image one starts with. In other words for example, if a target pixel is located at $(10, 10)$ cm, the best frequency would change if the pixel is moved.

4.1.2 Comparison of the three configurations for Test 1

In this section, three configurations; (Case 1) Multi-Monostatic/Muti-frequency configuration, (Case 2) Multi-static/Single-frequency configuration and (Case 3) Multi-static/Multi-frequency configuration. In this test, number of transmitters, receivers and frequencies are the same 41 points. This allow us to compare Cases 1 and 2 directly because the dimensions of matrices **L** are the same. Case 3 always has larger number of measurements than the others have, so we can not compare it directly. It contains all equations used in Cases 1 and 2, and it produces best solution among the three configurations.

Condition number

Condition number for Pseudo inverse scheme is summarized in Table I. Size of matrix **L** is same for Cases 1 and 2 while Case 3 has larger matrix. We may compare condition numbers for Cases 1 and 2 directly while we may not compare condition number for Case 3 with others. Condition number for Case 2 is smaller than Case 1, it indicates that Case 2 has more stable reconstruction than Case 1 does. Case 3 has lager condition number than Case 2 has when inhomogeneous Green's function. It is probably due to some equations which have ill conditioning. For example, Figure 8 may suggest that we must avoid to use some frequencies such as 2750 MHz and 3000 MHz because objects are unobserved due to the null field distribution within the medium. By the nature of regularization, such equations are eliminated by regularized inversion. For example, when the field distributions is slanted like 2750 MHz of Figure 8, it produces many of similar equations in matrix **L** and has many of small singular

values. Regularization techniques such as Truncated Singular Value Decomposition eliminate and ignore the small singular values components.

TABLE I: CONDITION NUMBER OF TEST 1.

	Case 1	Case 2	Case 3
Homogeneous	326 dB	312 dB	288 dB
Inhomogeneous	198 dB	168 dB	180 dB

L-curve

L curves for 3 cases are plotted for SNR = 30, 10 and -10 dB as shown in Figure 13. There is a same issue of comparison for 3 different configurations. We may compare L-curves for Cases 1 and 2 because the size of the matrix **L** is the same, however, we may not compare Case 3 with others because residual norm has different dimension for the horizontal axis. Case 2 has less residual norm than Case 1 has at the kinks of L-curves. This indicates reconstructed point spread function has less error than Case 1 has. Also, Case 2 has smaller solution norm than Case 1 has. This indicates that point spread function for Case 2 has less artifacts than its Case 1 has. Case 3 also has smaller solution norm at the corner than other two cases.

Normalized L-curve is also provided in Figure 14. Horizontal and vertical axes are normalized in a range between 10^{-1} and 10^{5}. Top left and bottom right of curves are all aligned. The plot corresponds to actual view when we may identify the corner. Multi-static configurations (Cases 2 and 3) have sharper kinks than the mono-static configuration. The sharper kink provides less ambiguity on choosing a regularization parameter. Therefore, Case 3 has an advantage on deciding a regularization parameter and providing more stable result of reconstruction.

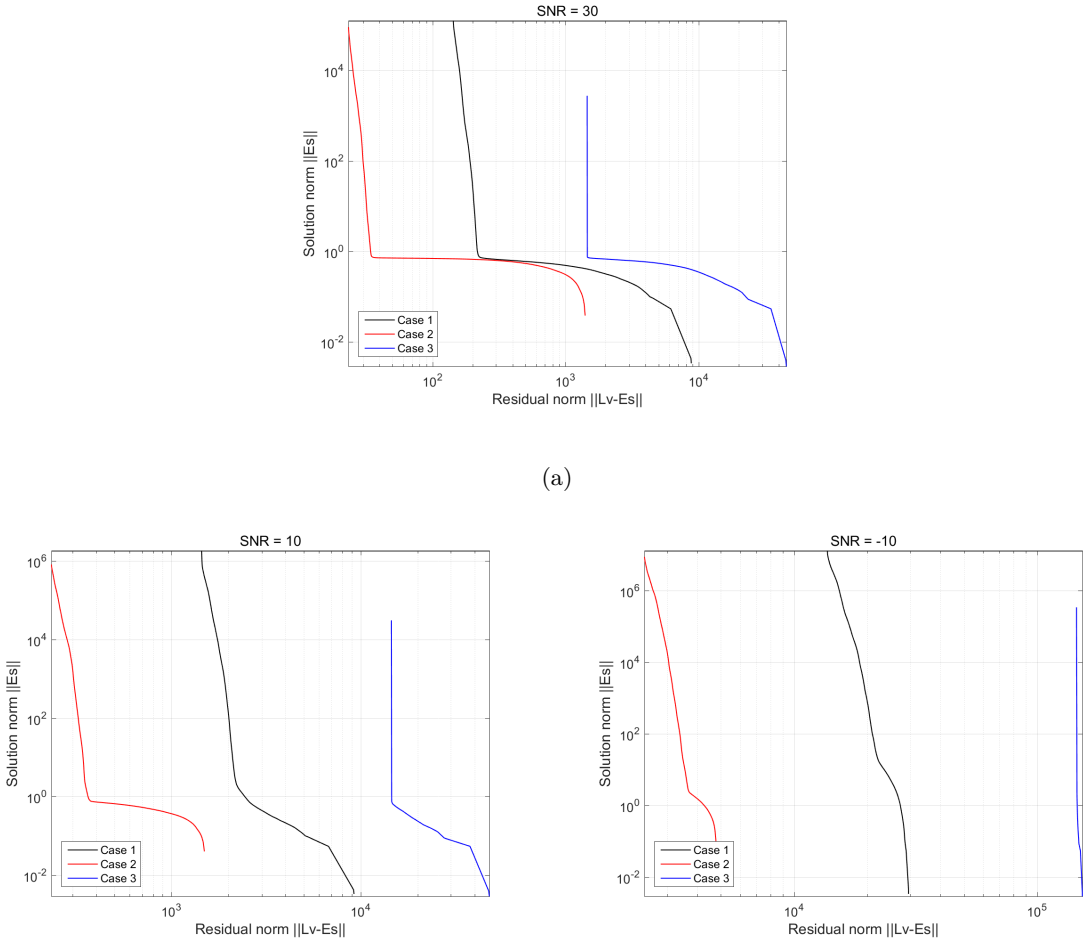

Figure 13: Comparison of unnormalized L-curves for Test 1 when AWGN are added to $\mathbf{E}^s$ with (a) SNR = 30 dB, (b) SNR = 10 dB, (c) SNR = -10 dB.

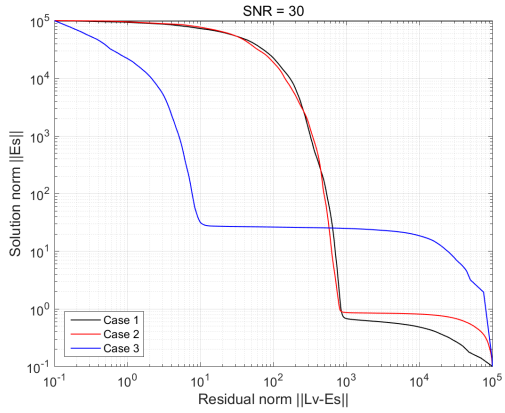

(a)

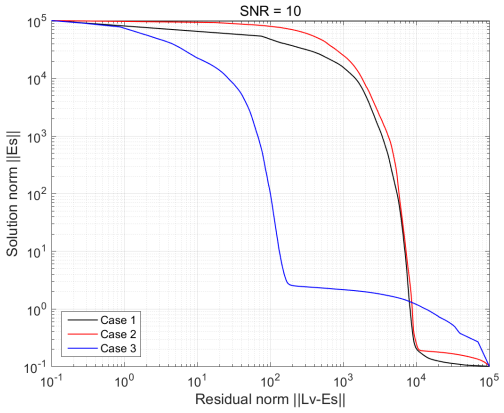

(b)

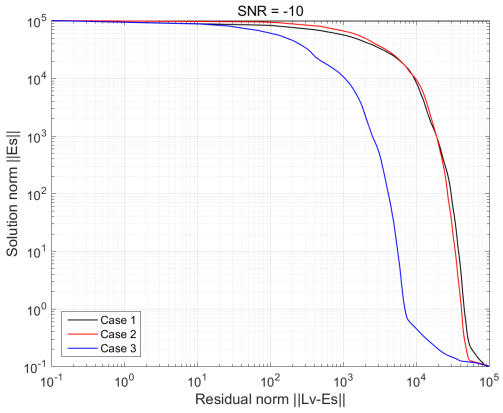

(c)

Figure 14: Comparison of normalized L-curves for Test 1 when AWGN are added to $\mathbf{E}^s$ with (a) SNR = 30 dB, (b) SNR = 10 dB, (c) SNR = -10 dB.

Singular values

Singular plot is shown in Figure 15. Case 2 has smaller slope of the singular value curve than Case 1 has. Remember small singular values are negligible for forward calculation while the small singular values contributes to unstable errors in inverse problem. Smaller slope of the curve indicates many equations are independent of each other and useful. L-curves for Cases 3 and 2 are almost parallel, but the region with small slope is longer. It indicates the reason why Case 3 has better results in following analyses.

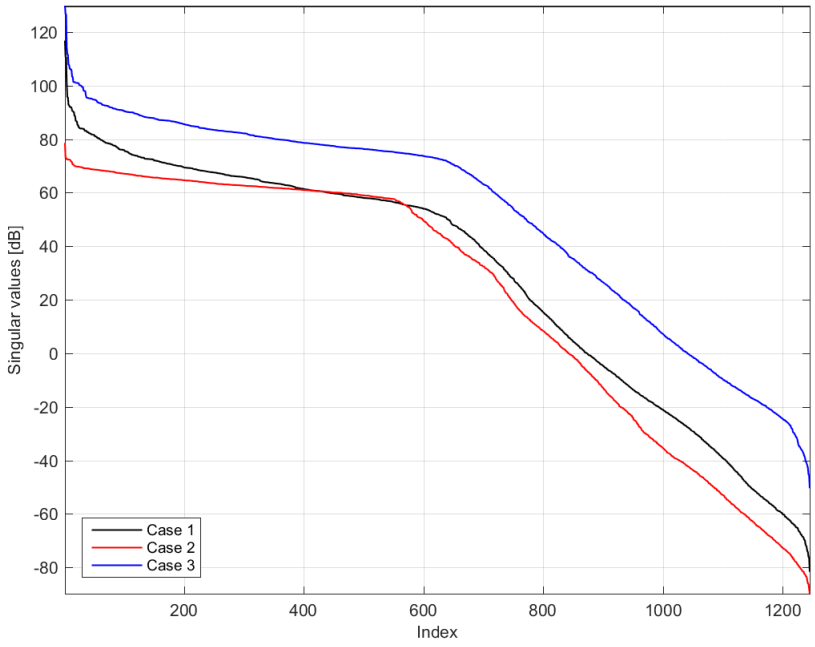

Figure 15: Singular values for Test 1.

Point spread function

The point spread function for three cases are shown in Figure 16, and corresponding entropy is summarized in II. The point spread function for SNR = 30, 10 and -10dB are analyzed to see how how sensitive to noise. This noise analysis imply ill conditioning of each three case configurations of measurements.

When SNR = 30, the resulting PSFs are very similar to each other. This is because the number of measurements are larger than the number of unknowns, and matrix **L** is over-determined. When SNR is decreased, we can see better results of Case 2 than Case 1, and of Case 3 than Case 2.

Figure 17 also shows the point spread function for the case when fundamental homogeneous Green's functions are used. The point spread function for homogeneous Green's functions has same conclusion as inhogeneous Green's function is used.

TABLE II: ENTROPY OF POINT SPREAD FUNCTION FOR TEST 1.

	Homogeneous			Inhomogeneous		
SNR [dB]	Case 1	Case 2	Case 3	Case 1	Case 2	Case 3
-10	6.64	6.42	3.43	6.34	6.49	5.52
10	4.99	3.44	2.24	6.33	5.47	4.74
30	4.19	2.62	2.02	5.42	5.13	4.20

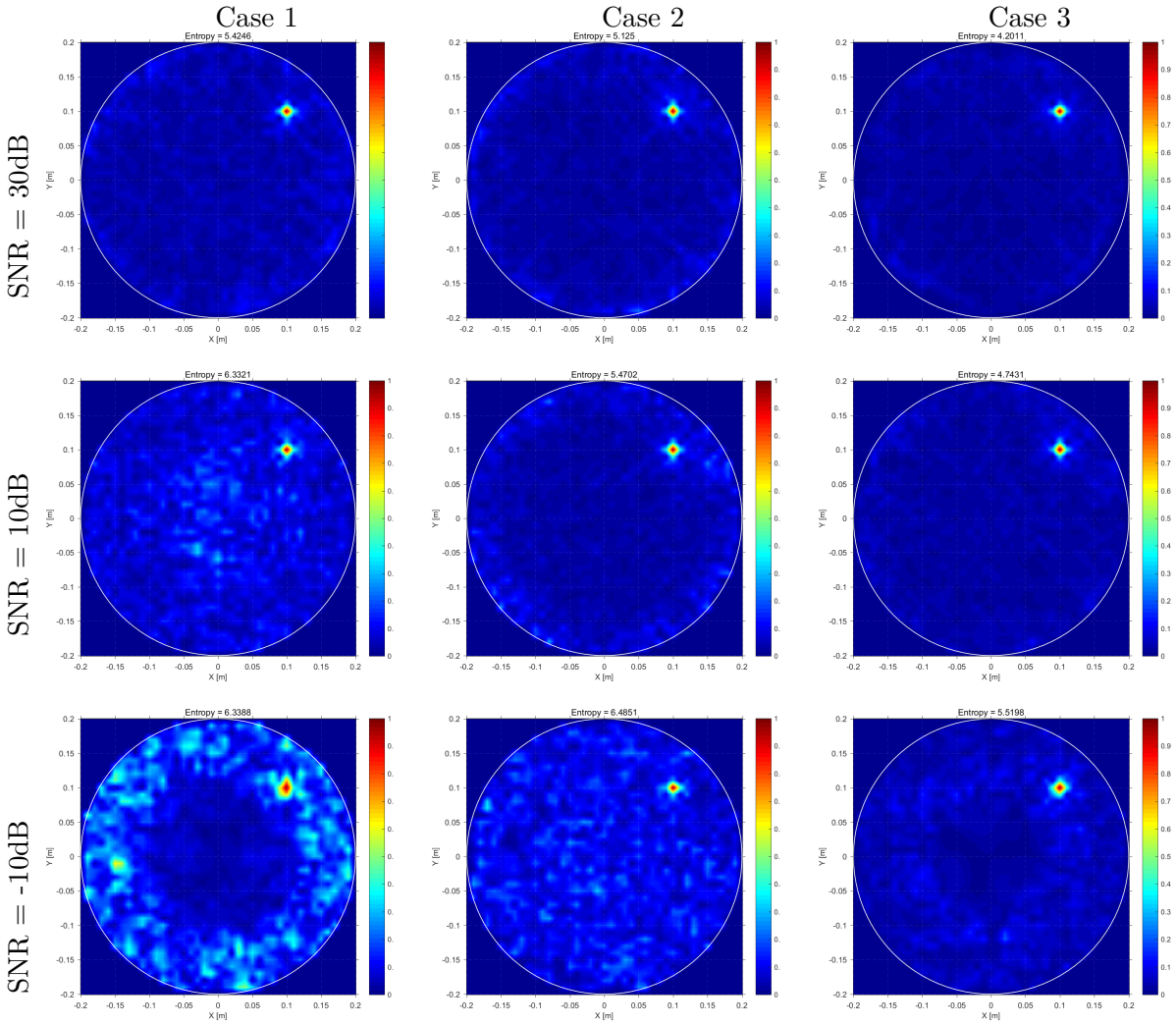

Figure 16: Point spread functions for Test 1 with inhomogeneous Green's function when AWGN of SNR = 30, 10 and -10 dB are added.

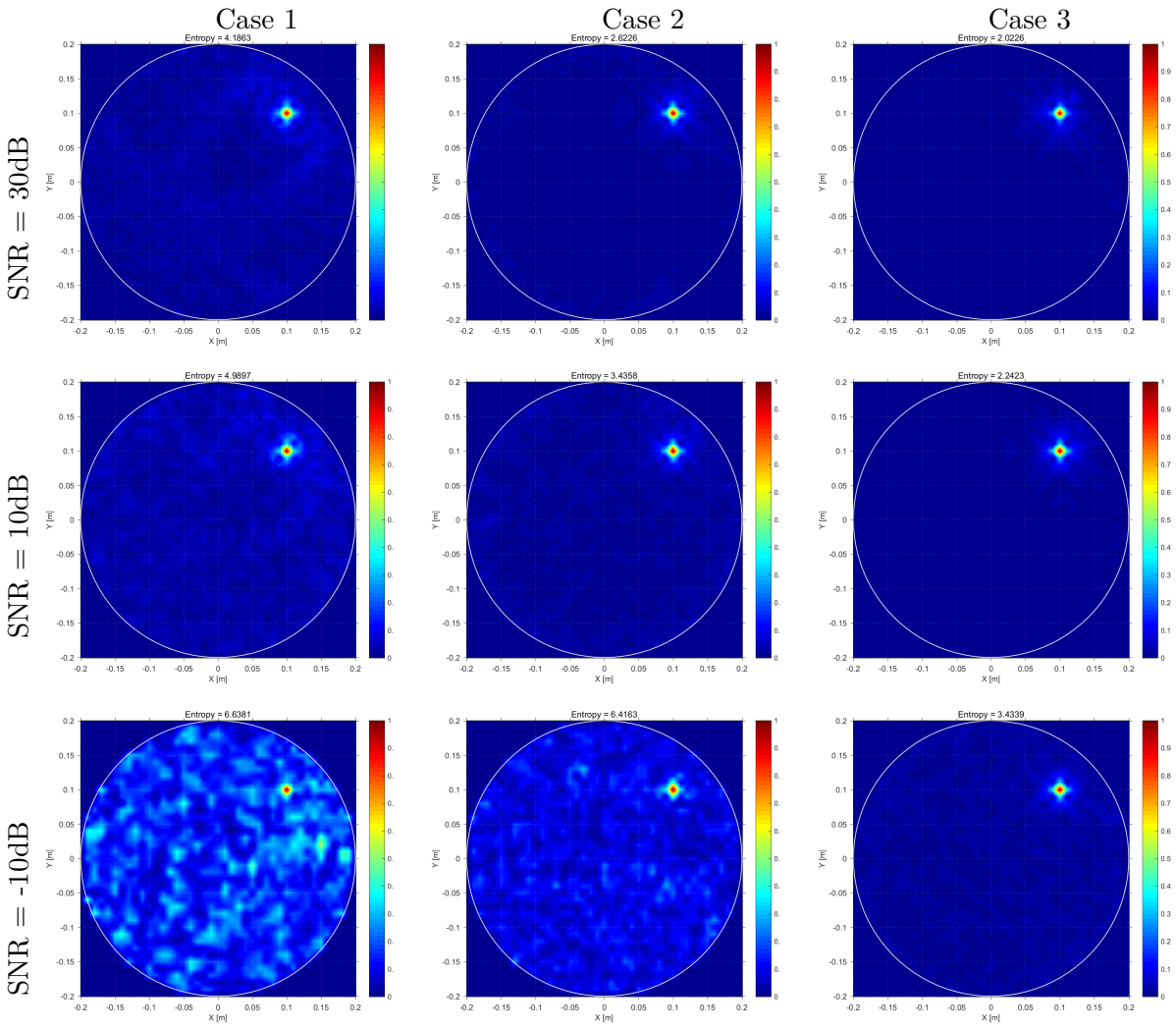

Figure 17: Point spread functions for Test 1 with homogeneous Green's function when AWGN of SNR = 30, 10 and -10 dB are added.

Spectral content

Reconstructed spectral content can be seen in analysis of the spectral content. The spectral content is computed as follow

$$SC(k_x, k_y) = \sum_{n=1}^{Nt} |v_n(k_x, k_y)|^2 \tag{4.3}$$

$$v_n(k_x, k_y) = \iint_D v_n(x, y) \exp\left[-j(k_x x + k_y y)\right] dxdy \tag{4.4}$$

where v_n is nth column vector of matrix $\mathbf{V}$, and Nt is number of singular values used in the analysis. In this thesis, Nt is optimum regularization parameter found in previous step with L-curve. Therefore, the spectral contents are directly related with analysis of point spread function shown in previous section.

Spectral contents for inhomogeneous Green's function are shown in Figure 18. In the figure, low frequency spatial component is shown in middle. In the analysis of spectral content, ideal case has uniform distribution (all in red). In fact, case of pseudo inverse use all terms $Nt \to N$, the number of unknowns, and it has uniform distribution. Truncated singular value decomposition regularization filters small singular values which is associated with high frequency spectral contents, and the other regularization methods also have the same low-pass filtering effect. The theoretical coverage of spectral content is discussed in (102), and we can see Edward's circle with radius of $2k_{b,max}$ which is

$$2k_{b,max} = 2\frac{2\pi f_{max}\sqrt{\varepsilon_b}}{c_0} = 251.3. \tag{4.5}$$

where f_{max}, ε_b and c_0 are maximum frequency 3 GHz, relative permittivity of the background medium 4, and speed of light 299792458 [m/s], respectively. For SNR = 30 and 10 dB, Case 3 has more coverage in high frequency which indicates improvement of resolution. When SNR = -10dB, the high frequency spectral content tends to contribute artifacts in reconstructed images. The high frequency component of spectral content is filtered in order to have robust reconstruction in Case 3.

As a reference, spectral content for homogeneous Green's function are also shown in Figure 19. One may immediately notice that there is a hole in low frequency component of spectral content. The behavior is inherited for inhomogeneous Green's function case as seen in Figure 18 for Case 1 and SNR = 10dB. We can see clear differences between for inhomogeneous and homogeneous Green's function of Case 1, and it can be concluded that the multi-scattering effect due to bounded medium provides more coverage in the low frequency.

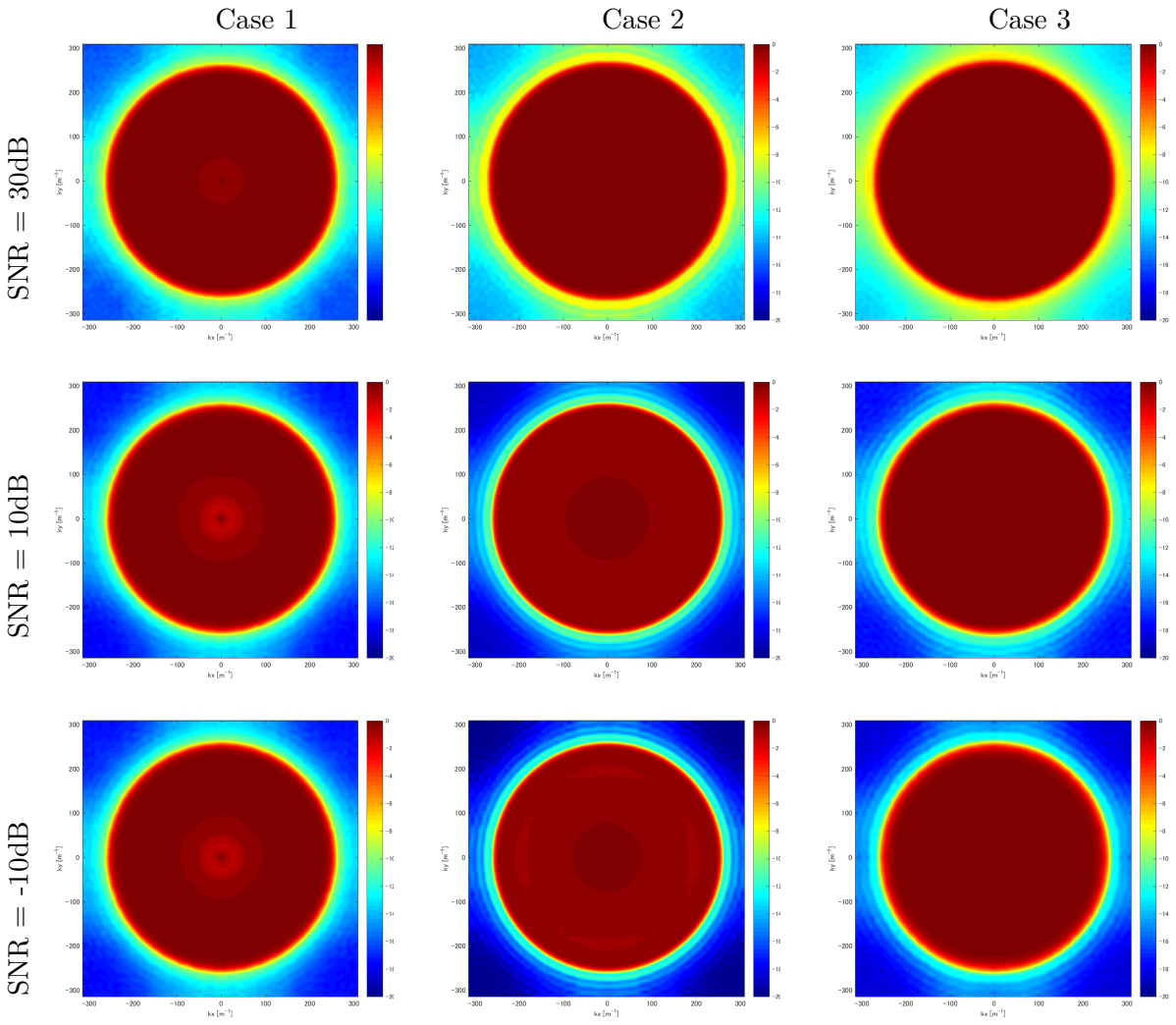

Figure 18: Spectral content for Test 1 with inhomogeneous Green's function when AWGN of SNR = 30, 10 and -10 dB are added.

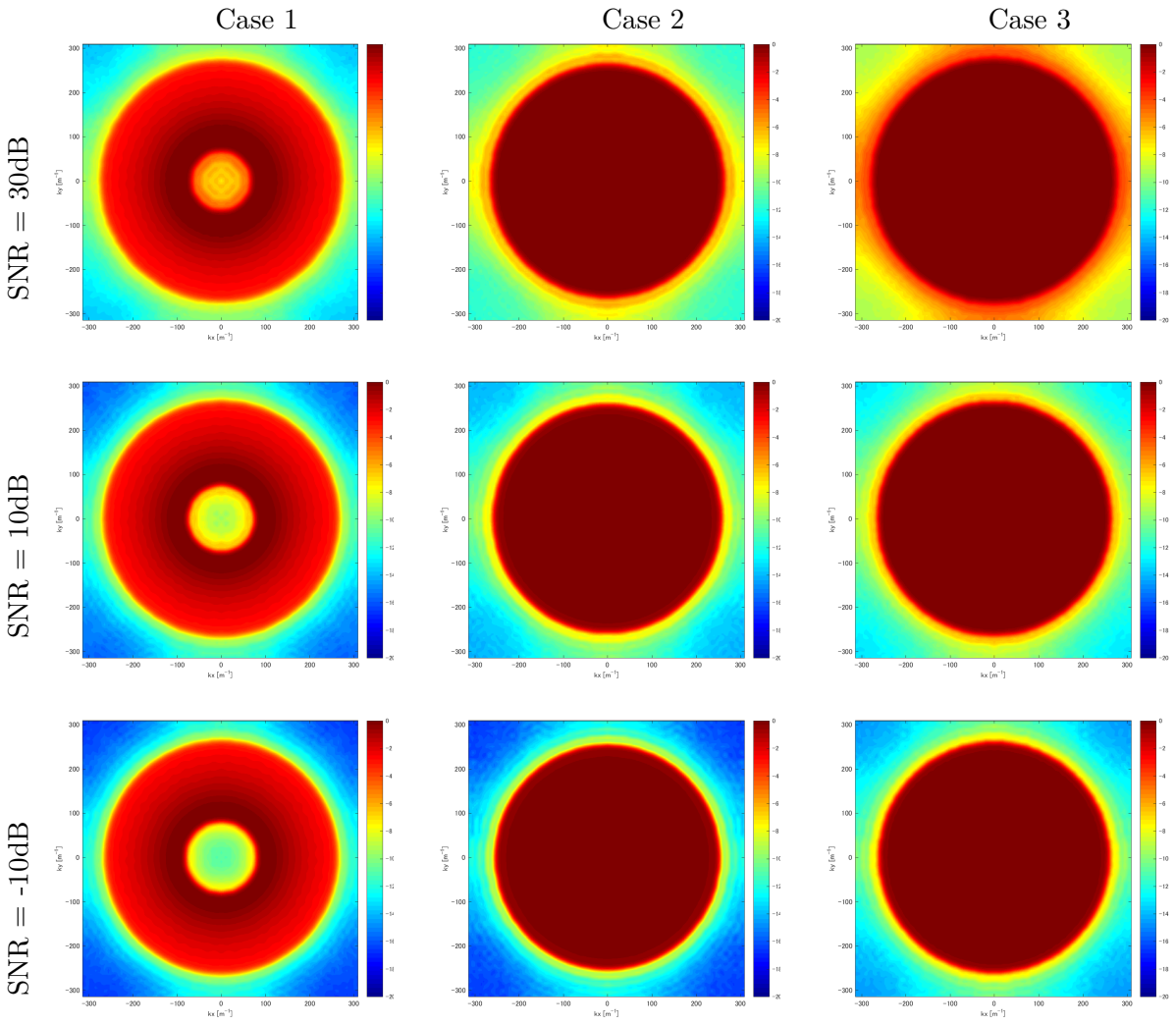

Figure 19: Spectral content for Test 1 with inhomogeneous Green's function when AWGN of SNR = 30, 10 and -10 dB are added.

4.2 Test 2: More number of frequencies values from Test 1

For Case 1 configuration, number of frequency is set to 41 points, so that dimensions of matrices are same for Cases 1 and 2. In section, number of frequencies is increased for case 1 to see if number of frequencies within the same range actually contributes to the quality of reconstruction.

In this test, number of transmitters and receivers are kept same as Test 1 while number of frequency is now changed to 201 points.

Condition number

Condition number is summarized in Table III. The condition number is increased when number of frequencies is increased. Also, recalling to Table I, the condition number is still larger than Case 2 and 3.

TABLE III: CONDITION NUMBER FOR CASE 1 OF TEST 2.

	Test 1	Test 2
Number of frequencies	41	201
Homogeneous	326 dB	317.3
Inhomogeneous	198 dB	206.6

L-curve

Normalized L-curve is shown in Figure 20. The range of L-curve is normalized to align top left and bottom right to compare three cases which has different sizes of matrices **L**. Case 1 still does not have sharp as Cases 2 and 3 even though Case 1 has more number of measurements than Case 2 has. In Truncated Singular Value Decomposition scheme, Case 1 is still more ambiguous to locate the kink of the curve and the optimum regularization parameter.

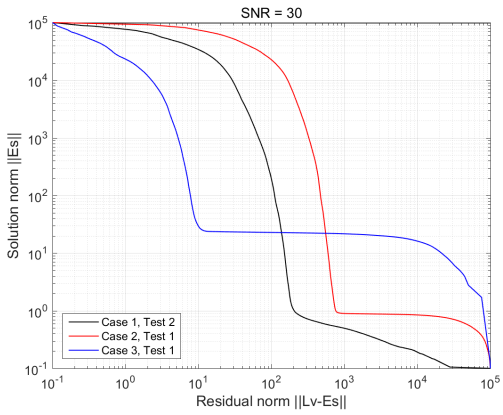

(a)

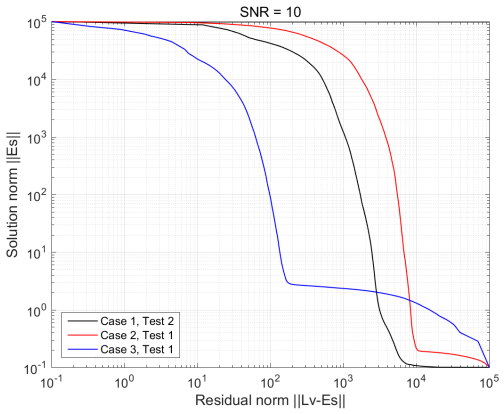

(b)

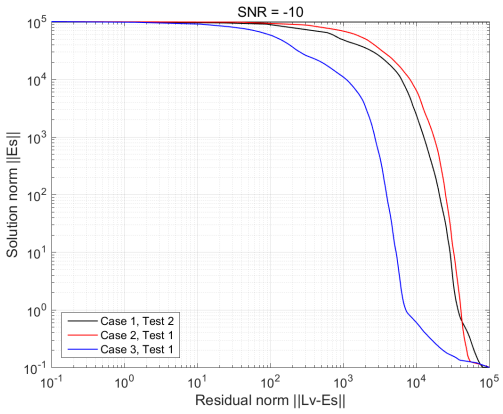

(c)

Figure 20: Comparison of normalized L-curves for Case 1 of Test 2 when AWGN of (a) SNR = 30 dB, (b) SNR = 10 dB, (c) SNR = -10 dB are added. L-curves for Case 2 and 3 of Test 1 are shown as references.

Singular values

Singular values are plotted in Figure 21. Cases 2 and 3 from Test 1 are also plotted. By coincidence, singular values for Cases 1 and 3 are very similar so that we can compare the curves. Slope of the curve for Case 1 has steeper than the Case 3 has within the range of index from 100 to 700. This means Case 3 has more independent equations available than Case 1 does, and this is the reason why Case 1 has condition number larger than Case 3 does.

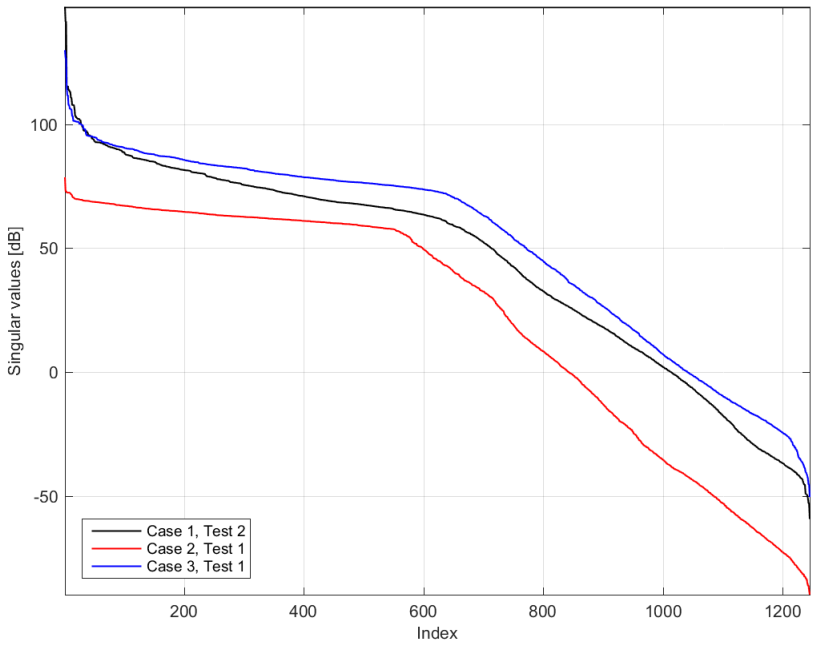

Figure 21: Singular values of Test 2.

Point spread function

Figure 22 shows point spread function for Test 2, and corresponding entropy is summarized in Table IV. While we don't see large differences when SNR = 30 dB, more artifact seen in Case 1 when SNR = 10 and -10 dB. The result tells that Case 1 still has ill conditioning even though number of frequency points is increased. Furthermore, the reconstructed point spread function for Case 1 of Test 2 is very similar to Case 1 of Test 1 Figure 16 which concludes that the increase of frequency points within the same bandwidth does not provide better quality of reconstructed images.

TABLE IV: ENTROPY OF POINT SPREAD FUNCTION FOR TEST 2.

SNR [dB]	Case 1, Test 2	Case 2, Test 1	Case 3, Test 1
-10	6.49	6.49	5.52
10	6.48	5.47	4.74
30	3.39	5.13	4.20

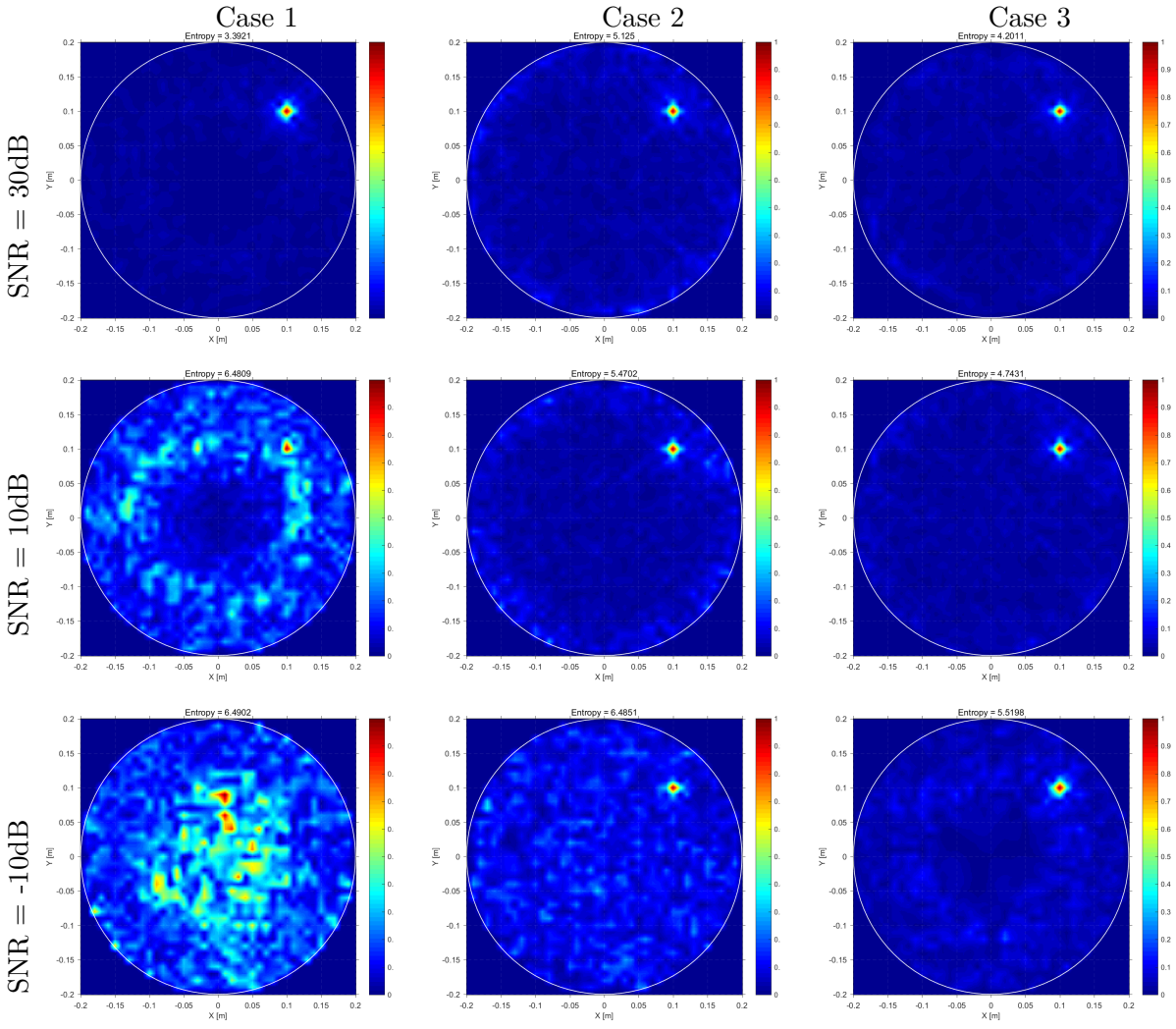

Figure 22: Point spread functions for Case 1 of Test 2 with inhomogeneous Green's function when AWGN of SNR = 30, 10 and -10 dB are added. Point spread functions for Cases 2 and 3 of Test 1 are shown as references.

Spectral content

Spectral contents for Case 1 are shown in Figure 23. Spectral content from Test 1 is also shown to see the difference due to increase of number of frequencies. Interestingly, uniformity of spectral content is sacrificed in Test 2 for SNR = 30 and 10 dB. It is probably due to worsening of ill conditioning which is observed as increase of condition number in previous analysis.

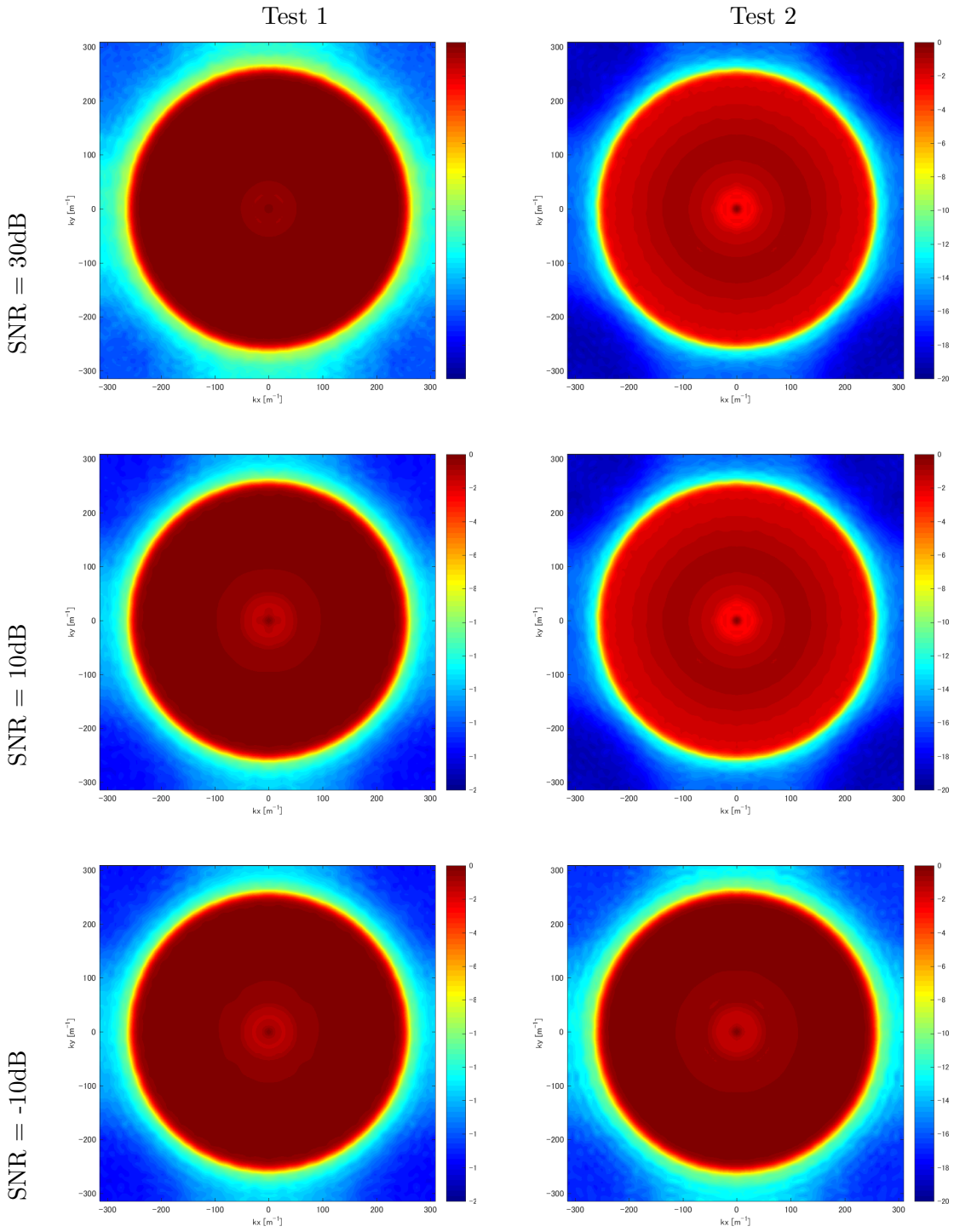

Figure 23: Spectral content for Case 1 configuration with inhomogeneous Green's function when AWGN of SNR = 30, 10 and -10 dB are added. Spectral contents for Case 1 of Test 1 is shown as references.

4.3 Test 3: Test case for tomographic reconstructions

In this section, resolution analysis for Test 3 is provided. The three configurations are produced from measurements of 50 positions of transmitters and receivers and 14 points of frequencies wchic are from 1000 MHz to 2900 MHz with increment of 150 MHz. while the geometry of dielectric cylinder is kept same as Test 1. The transmitters and receivers are located along the circumference of the dielectric cylinder at a radius of 21 cm and 20.9 cm respectively as shown in Figure 24. The test configuration is chosen very similar to (3), and used in following chapter 5.

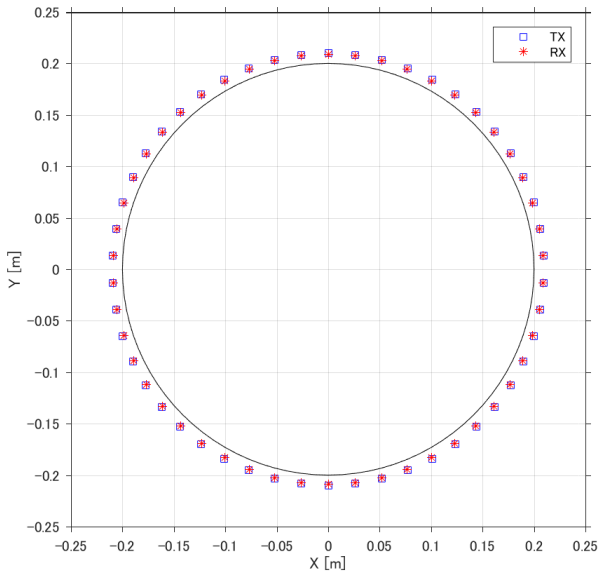

Figure 24: Locations of line source (TX) and observation (RX) for Test 3 indicated as blue squares and red stars, respectively. The black circle indicates the Domain of Investigation (DoI).

System matrices **L** are reproduced from the available measurements. Three configurations now have different dimensions as follow

Case 1: Multi-Monostatic/Muti-frequency configuration

This configuration corresponds to the typical configuration used for Ground Penetrating Radar. The measurements are limited to many mono-static measurements, which means transmitters and receivers are collocated. All available frequencies are used in this configuration. In this configuration, total number of measurements are 50 positions $\times$ 13 frequencies, 650 measurements.

Case 2: Multi-static/Single-frequency configuration

This configuration use all combination of 50 transmitters and 50 receivers, however the frequency is limited to a single frequency at 2950 MHz. In this, configuration, total number of measurements are $50 \times 50 = 2500$ measurements.

Case 3: Multi-static/Multi-frequency configuration

This configuration uses all available measurements. All combination of transmitters, receivers and frequencies are used.In this, configuration, total number of measurements are $50 \times 50 \times 13 = 32500$ measurements.

L-curve

Normalized L-curves for 3 cases are plotted for SNR =30 10, and -10 dB as shown in Figure 25. Since all three cases have different dimensions, we may not compare the curves directly. Further analysis is skipped in this section, however we may check the corner sharpness of the curve.

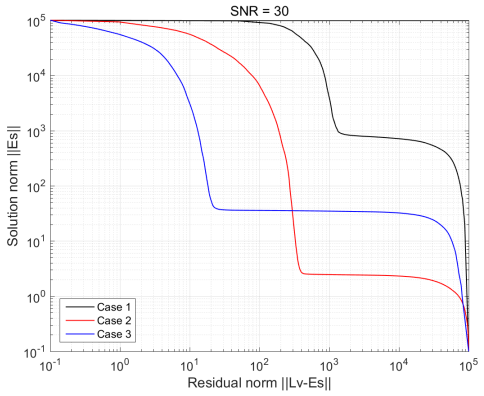

(a)

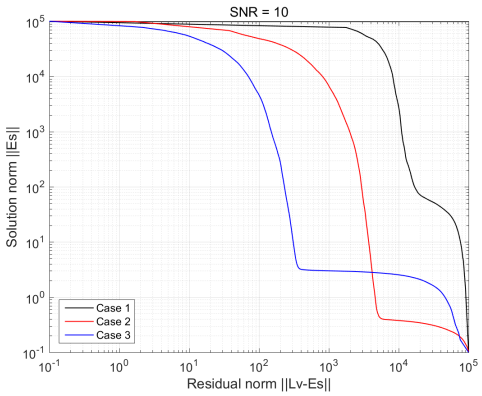

(b)

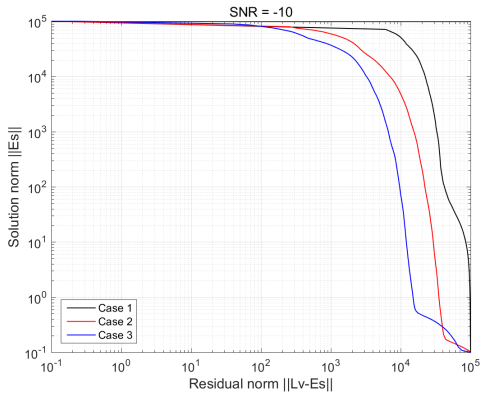

(c)

Figure 25: Comparison of normalized L-curves for Test 3 when AWGN of (a) SNR = 30 dB, (b) SNR = 10 dB, (c) SNR = -10 dB are added.

Point spread function and spectral content

Point spread functions and spectral content for optimum regularization parameter Nt are shown in Figure 26 and Figure 27. Entropy of the point spread function is summarized in Table V

TABLE V: ENTROPY OF POINT SPREAD FUNCTION FOR TEST 3.

SNR [dB]	Case 1, Test 2	Case 2, Test 1	Case 3, Test 1
-10	6.57	6.44	5.33
10	5.93	3.46	2.55
30	3.84	2.44	2.20

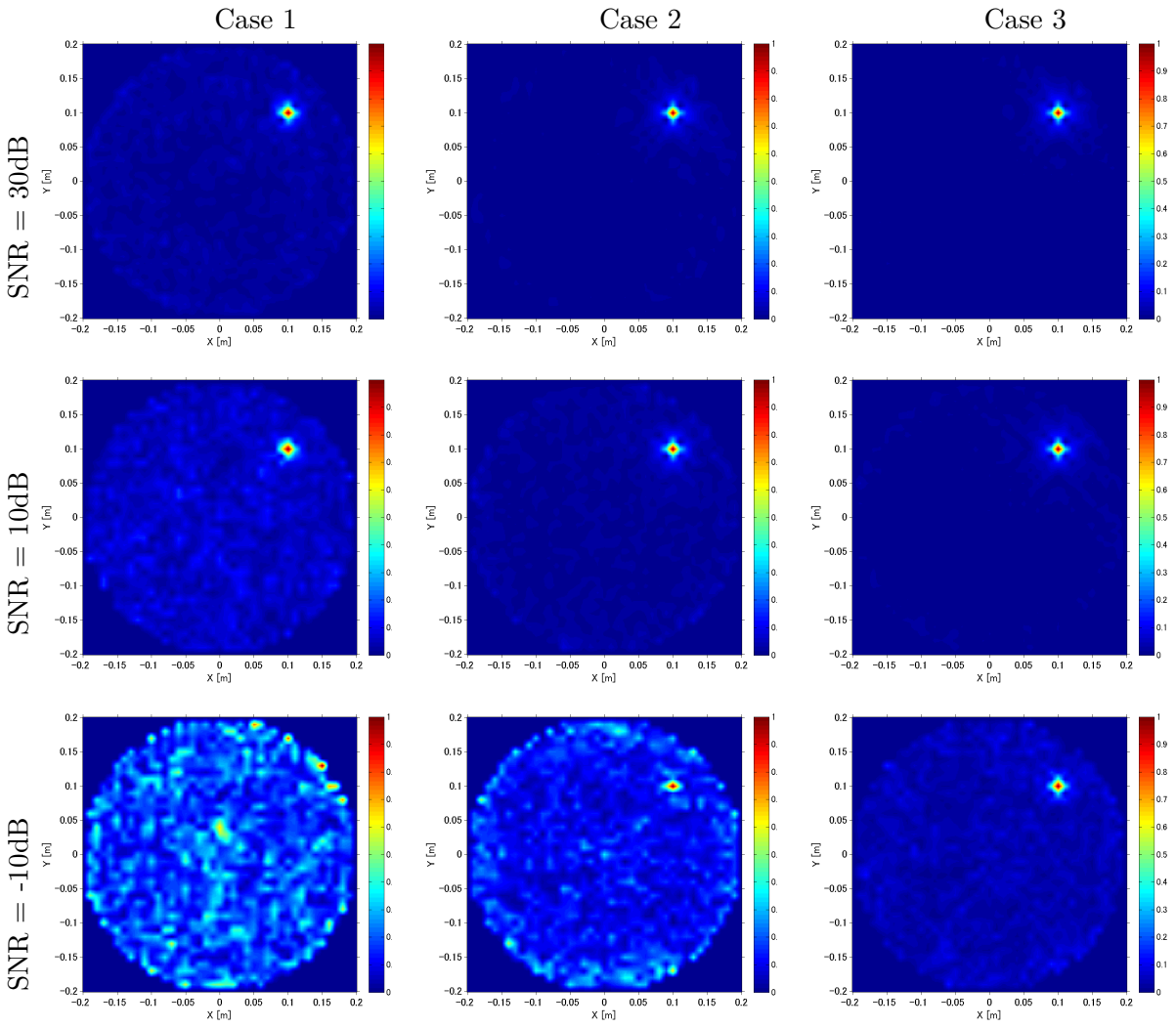

Figure 26: Spectral content for Test 3 with inhomogeneous Green's function when AWGN of SNR = 30, 10 and -10 dB are added.

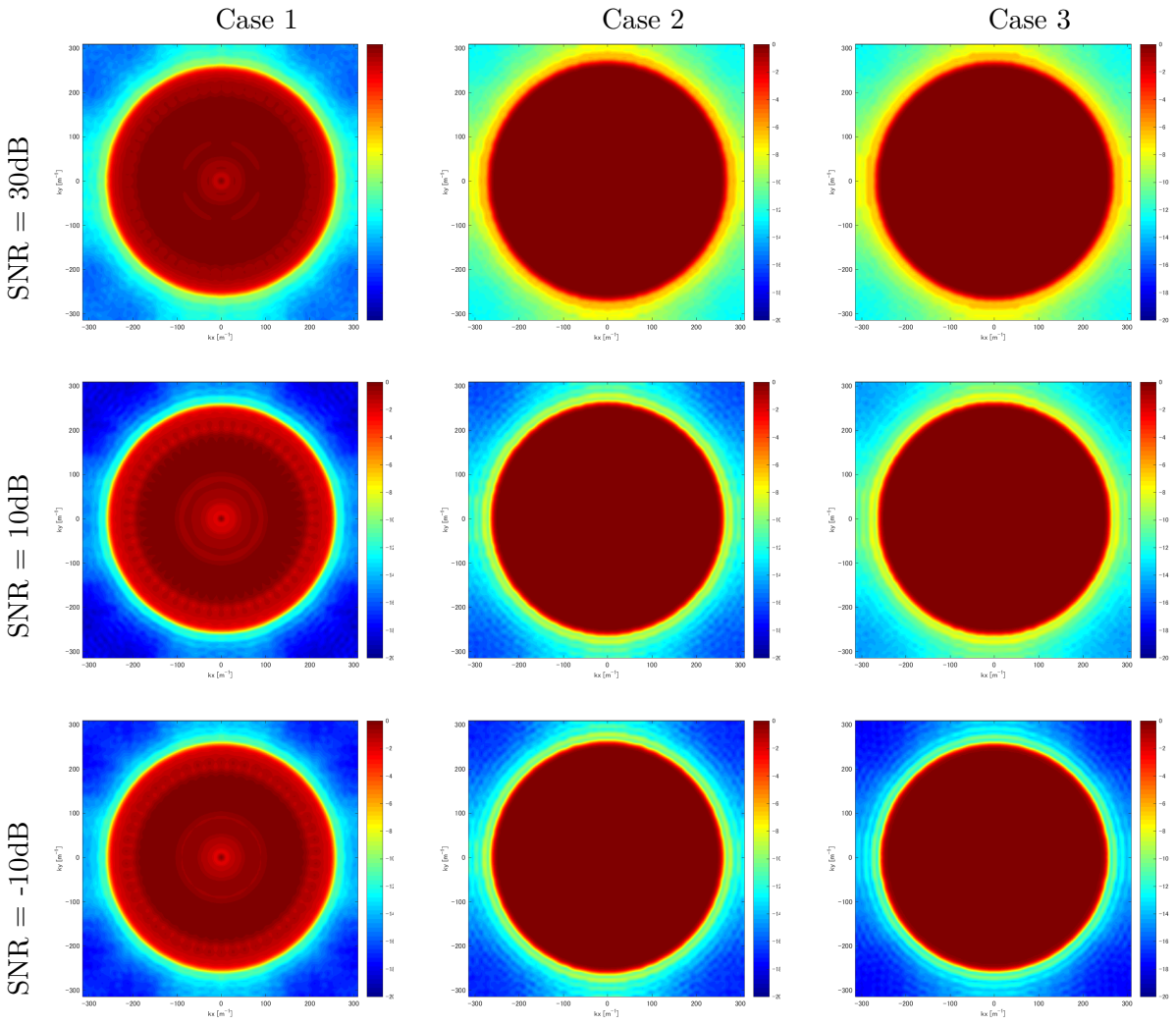

Figure 27: Spectral contents for Test 3 with inhomogeneous Green's function when AWGN of SNR = 30, 10 and -10 dB are added.

CHAPTER 5

TOMOGRAPHIC RECONSTRUCTION

Reconstructions using RF Tomography are demonstrated in this chapter. In previous chapter, resolution analysis for three configurations are compared in mathematics sense because the scattered field $\mathbf{E}^s$ is produced from the forward calculation of $\mathbf{E}^s = \mathbf{L} \cdot \mathbf{v}$. On the other hand, the electromagnetic scattered field $\mathbf{E}^s$ is produced from Method of Moment simulation and actual experiments in this chapter.

Conjugate Gradient method and Algebraic Reconstruction Technique are also used. Those inversion techniques allow us to introduce constrains, and provide improvement on resulting reconstructions and unique information of material by considering real and imaginary part of reconstructed contrast.

5.1 Numerical examples of RF Tomography

This section continues from Section 4.3 of Chapter 4, which is the resolution analysis for 50 transmitters and 50 receivers with frequencies bestween 1000 MHz and 2950MHz with 150 MHz step in Test 3 of Chapter 4. The same setup is used to produce system matrices $\mathbf{L}$ for three configurations (Case 1) Multi-monostatic/Multi-frequency, (Case 2) Multi-static/Single-frequency and (Case 3) Multi-static/Multi-frequency, however actual scattered electromagnetic field $\mathbf{E}^s$ is produced from Method of Moment simulations.

The testing geometries contains Perfect Electric Conductor (PEC) and/or hollow cylinders with a 2.5 cm radius are located for the first three geometries, and a 1×5 cm rectangular PEC and/or hollow cylinders are located between two PEC cylinders next two geometries.

The scattered field data is computed by the Method of Moment using the commercial software FEKO (103). Two-dimensional simulations in the XY-plane are implemented by setting a wire source with a periodic structure along the z direction.

First, the Method of Moment simulation and an analytical solution in a free space are compared. A normalizing constant is determined by

$$C = \frac{E^i_{Analytical}}{E^i_{FEKO}}. \tag{5.1}$$

Second, the scattered electric field is obtained through background subtraction.

1. Compute the electric fields in the presence of a PEC and/or a hollow cylinder.
2. Compute electric fields in the presence of only a dielectric cylinder. In this test, the dielectric cylinder is treated as a background medium and part of the incident field.
3. Find a scattered electric field due to irregularity by subtracting Step 2 from Step 1, and multiply the normalizing constant.
4. Corrupt the scattered electric field by adding AWGN with SNR = 10 dB and -10 dB.

Because the dielectric cylinder is treated as background and its total electric field is treated as incident field in step 2, the background dielectric cylinder won't contributes to scattered fields and the image of the cylinder won't be reconstructed.

Third, the unknown contrast **v** are inverted by the Truncated Singular Value Decomposition, the Conjugate Gradient method, and the Algebraic Reconstruction Technique, and reconstructed images are displayed. The reconstructed images are normalized to their maximum, and their entropy is evaluated for each images.

5.1.1 Tomographic examples using Truncated Singular Value Decomposition

In order to confirm the conclusion of the resolution analysis in Chapter 4, the first set of tomographic iamges are produced by TSVD. Similar to resolution analysis, the optimum regularization parameters are obtained from a kink of L-curve.

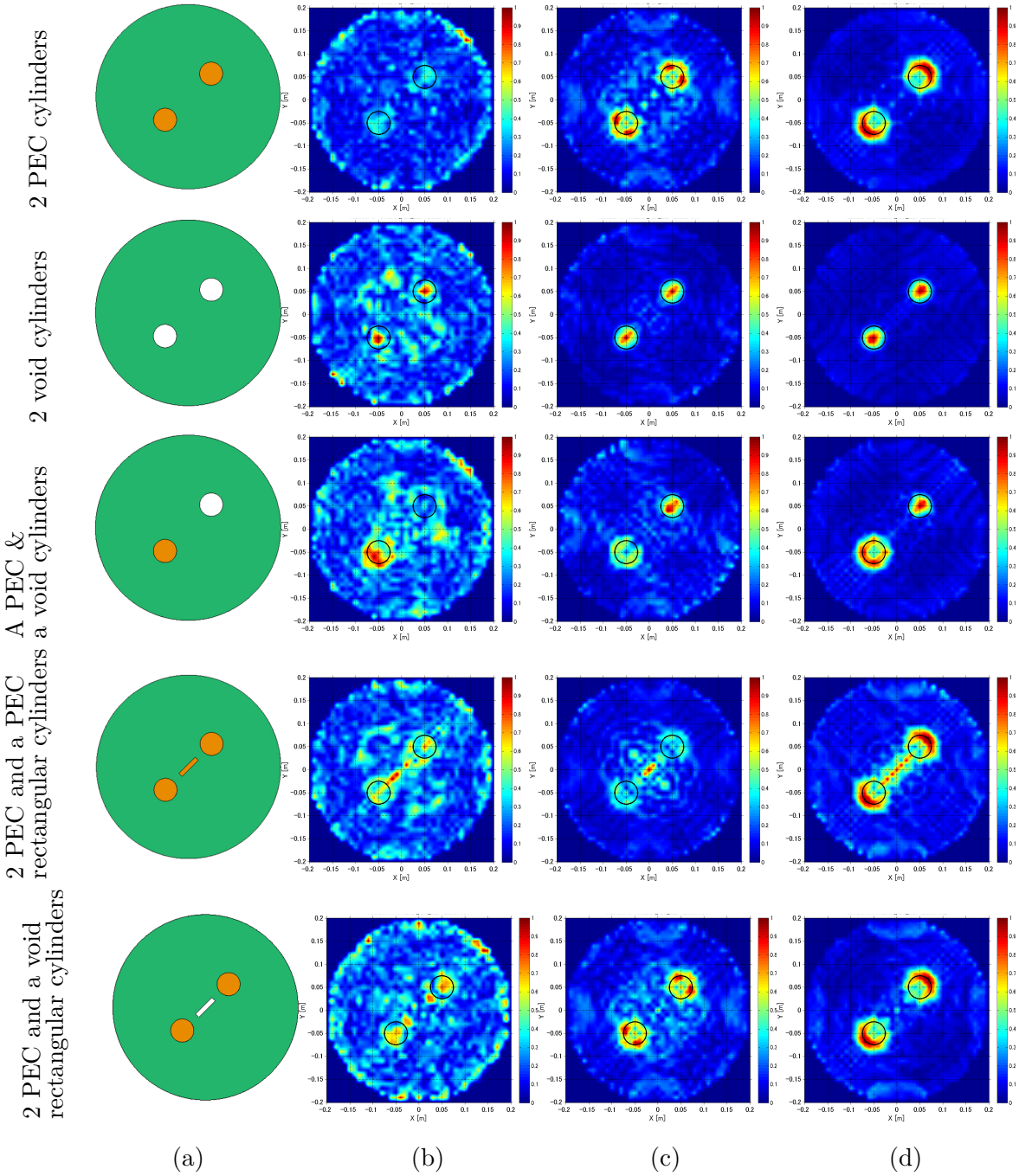

Figure 28: Tomographic images by TSVD without AWGN: (a) Geometry, (b) Multi-Monostatic Muti-frequency configuration, (c) Multi-static Single-frequency configuration and (d) Multi-static Multi-frequency configuration.

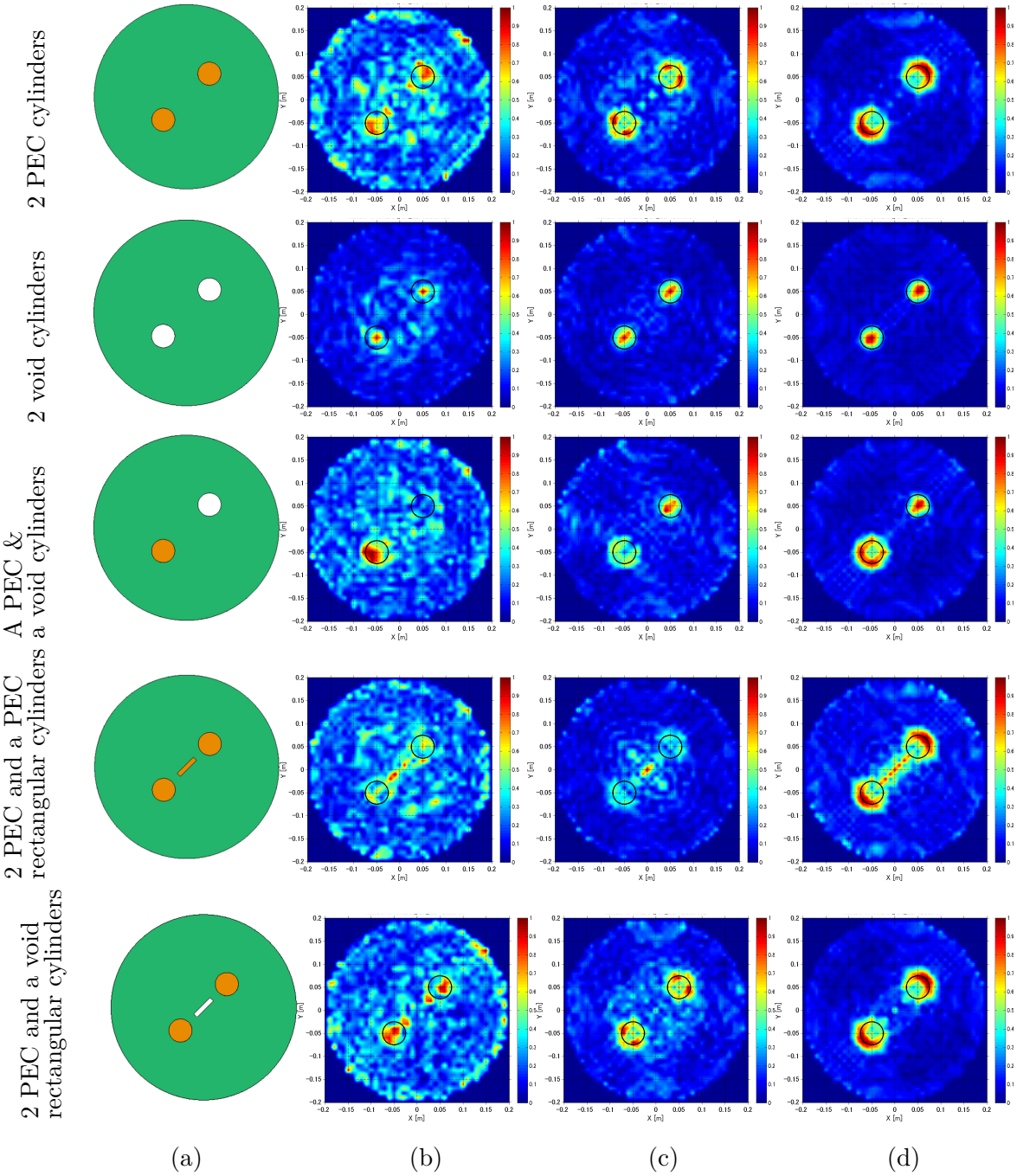

Figure 29: Tomographic images by TSVD with AWGN of SNR = 10 dB: (a) Geometry, (b) Multi-Monostatic Muti-frequency configuration, (c) Multi-static Single-frequency configuration and (d) Multi-static Multi-frequency configuration.

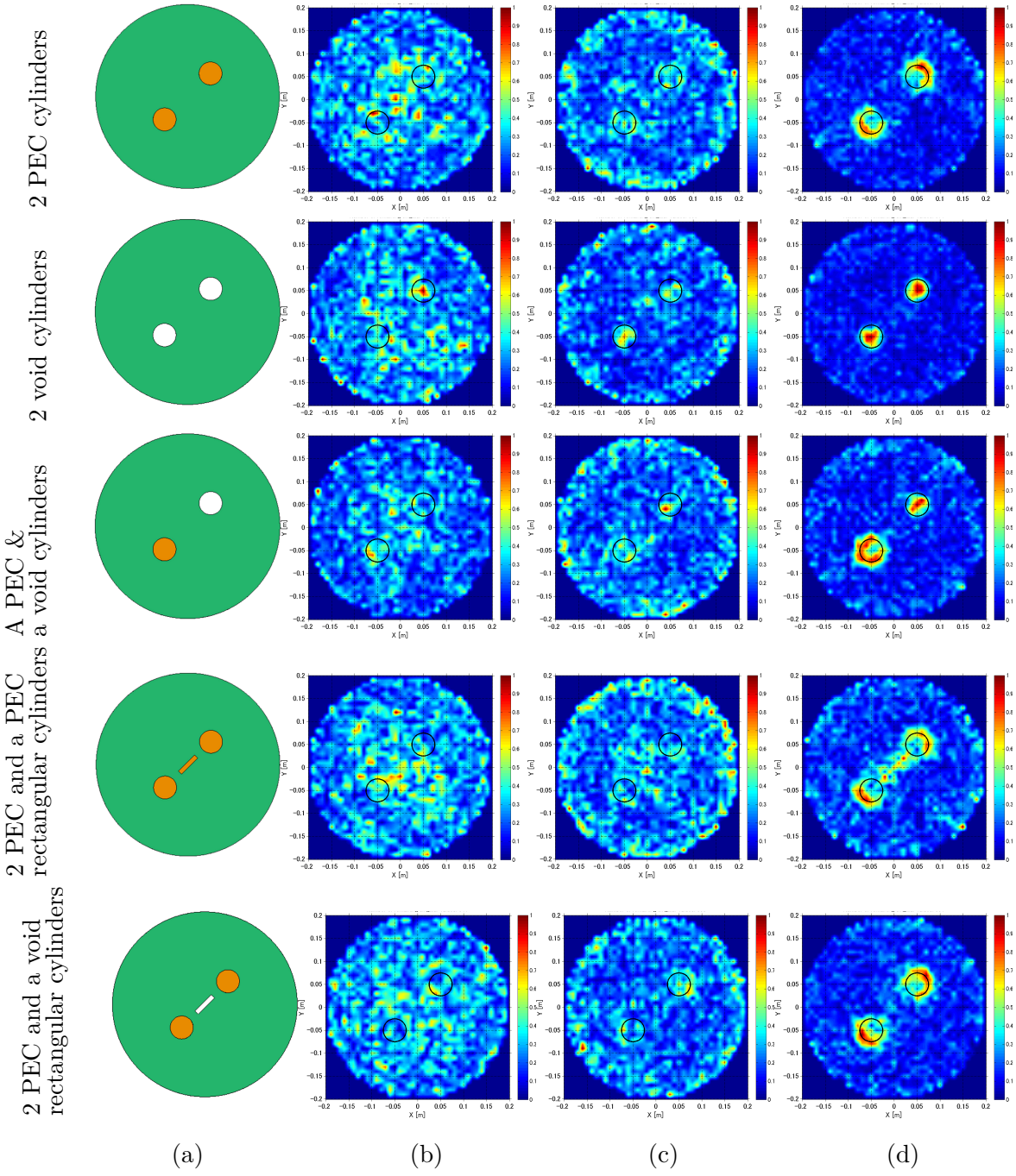

Figure 30: Tomographic images by TSVD with AWGN of SNR = -10 dB: (a) Geometry, (b) Multi-Monostatic Muti-frequency configuration, (c) Multi-static Single-frequency configuration and (d) Multi-static Multi-frequency configuration.

Tomographic images using TSVD for noiseless, AWGN of SNR = 10, and -10 dB are shown in Figure 28 through Figure 30. We may observe less artifacts in Case 3 (Multi-static/Multi-frequency configuration) in all reconstructed images. In particular, Case 3 configurations is stronger against noise as observed in Figure 30 for SNR = -10 dB.

Also, we might distinguish the type of material of the objects in the reconstructed images from the contrast. In fact, while the contrast is distributed within the hollow cylinder, in the case of metallic cylinder a contour line is observed and reconstructed. This reconstructed behavior is expected since the reconstruction behavior is related to the current distribution. In other words, in the case of a dielectric object, displacement currents exists throughout the volume of the object and so the entire volume contributes to the scattered field and the dielectric contrast. On the other hand, in the case of a metallic object, currents can only exists at its surface and so only the surface of the object contributes the creation of the scattered field and of the contrast.

A PEC with crack

Tomographic reconstruction using RF Tomography for a PEC cylinder with random a PEC cylinder is demonstrated. The test geometry contains a PEC cylinder with raduous 2.5 cm and approximately 5 cm long random shaped hollow near the PEC cylinder. The test geometry is shown in Figure 31.

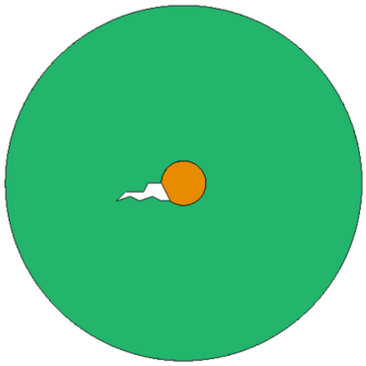

Figure 31: Geometry of a PEC cylinder with a crack.

Tomographic images using TSVD inversion for the test geometry is shown in Figure 32. This problem is challenging to identify the crack because the scattered field from the PEC cylinder is dominant which masks the scattered field due to the crack. Case 3 configuration provides the best result, and the exsistance of the crack is indicated as irregular shape in addition to the outlined PEC cylinder.

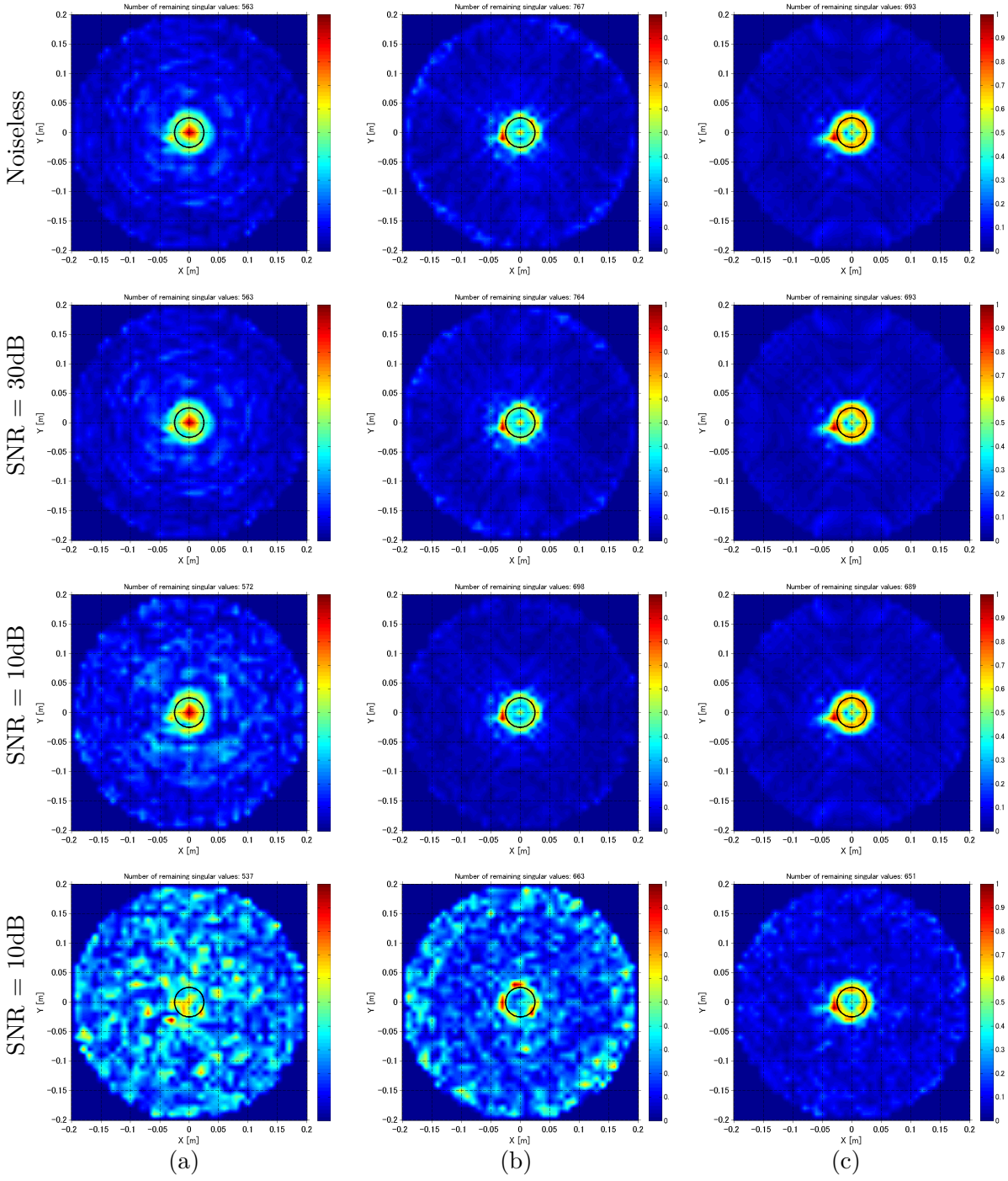

Figure 32: Tomographic images of a PEC cylinder with a crack using TSVD for (a) case 1, (b) case 2 and (c) case 3, with Noiseless, AWGN of SNR = 30, 10 and -10 dB.

Entropy of the tomographic images using TSVD without noise is summarized in Table VI. Entropy is used to compare numerically the quality of the tomographic images. Large entropy of Case 1 configuration means more artifacts spread over the entire images. Also, reconstructing images for PEC cylinder has larger entropy than the hollow cavity cylinders. Even though it is expected to have large entropy for geometries with PEC cylinders because PEC cylinder is reconstructed as contour, it also indicates noisier images of PEC objects.

TABLE VI: ENTROPY OF THE TOMOGRAPHIC IMAGES USING TSVD.

geometry	Case 1	Case 2	Case 3
2 PEC cylinders	6.5117	6.0312	5.4404
2 void cylinders	6.5399	5.5351	4.9468
A PEC & a void cylinders	6.5508	6.1368	5.4059
2 PEC & a PEC rectangular cylinders	6.5576	6.1513	5.9320
2 PEC & a void rectangular cylinders	6.5362	6.1268	5.6872
A PEC cylinder with crack	5.7659	5.4947	4.8815

5.1.2 Tomographic examples using Conjugate Gradient and Algebraic Reconstruction technique

Tomographic images using iterative regularization method are provided. Tomographic results using TSVD were provided previously. TSVD is categorized as direct regularization method since the proper images are obtained by modifying, filtering for specifically in TSVD , the ill-conditioned component of linear system matrix $\mathbf{L}$. However, TSVD requires singular value decomposition which is computationally costly. On the other hand, iterative regularization methods such as Conjugate Gradient and Algebraic Reconstruction Technique does not require large computational effort like singular value decomposition and inverse matrix operations. Also, iterative method is easy to introduce constraints in middle of process. It means the reduction of possible solutions.

The constraints are introduced based on a prior knowledge of $\varepsilon_r(\boldsymbol{\rho}') \leq \varepsilon_b$ for hollow cavities and $\sigma(\boldsymbol{\rho}') \geq 0$. Immediately after the solution is updated for each iteration, the modification of solution is applied as follows,

$$\text{if} \quad \text{Re}(\mathbf{v}) > 0 \quad \rightarrow \quad \text{Re}(\mathbf{v}) = -|\text{Re}(\mathbf{v})| \tag{5.2}$$

$$\text{if} \quad \text{Im}(\mathbf{v}) > 0 \quad \rightarrow \quad \text{Im}(\mathbf{v}) = -|\text{Im}(\mathbf{v})|. \tag{5.3}$$

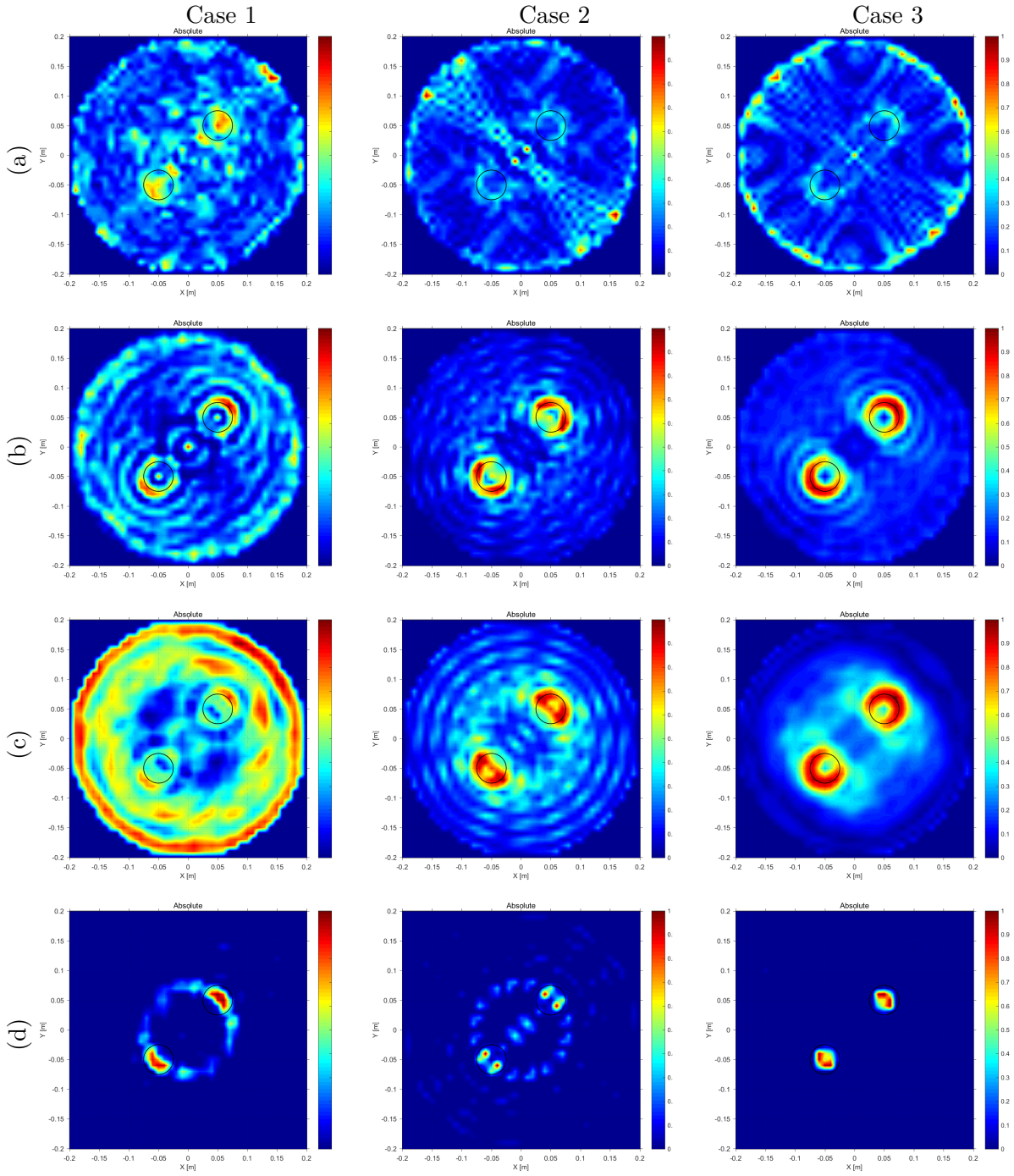

Figure 33: Tomographic images of two PEC cylinders (a) Conjugate Gradient method, (b) Conjugate Gradient method with modification (c) Algebraic Reconstruction technique (d) Algebraic Reconstruction technique with modification.

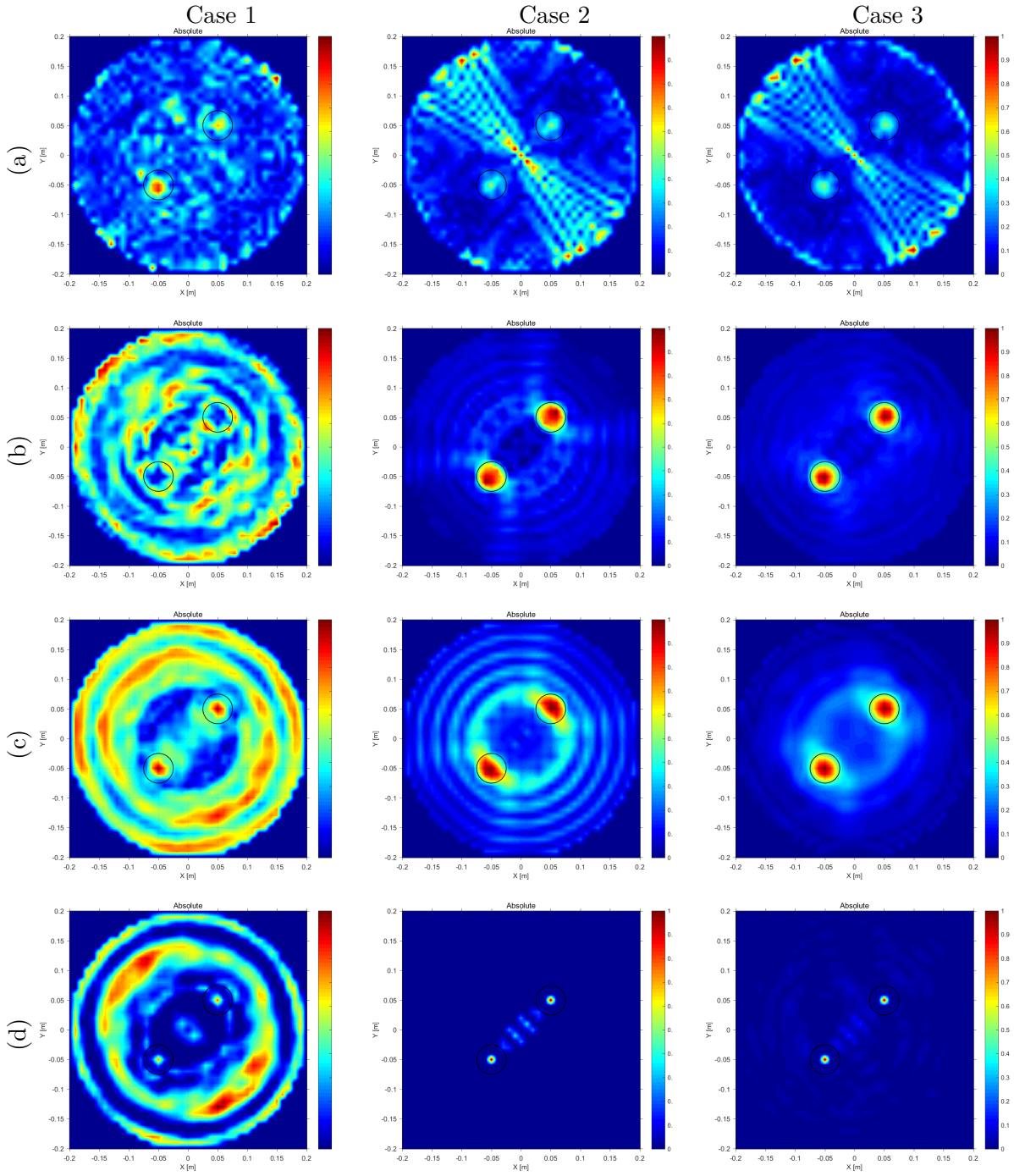

Figure 34: Tomographic images of two hollow cylinders (a) Conjugate Gradient method, (b) Conjugate Gradient method with modification (c) Algebraic Reconstruction technique (d) Algebraic Reconstruction technique with modification.

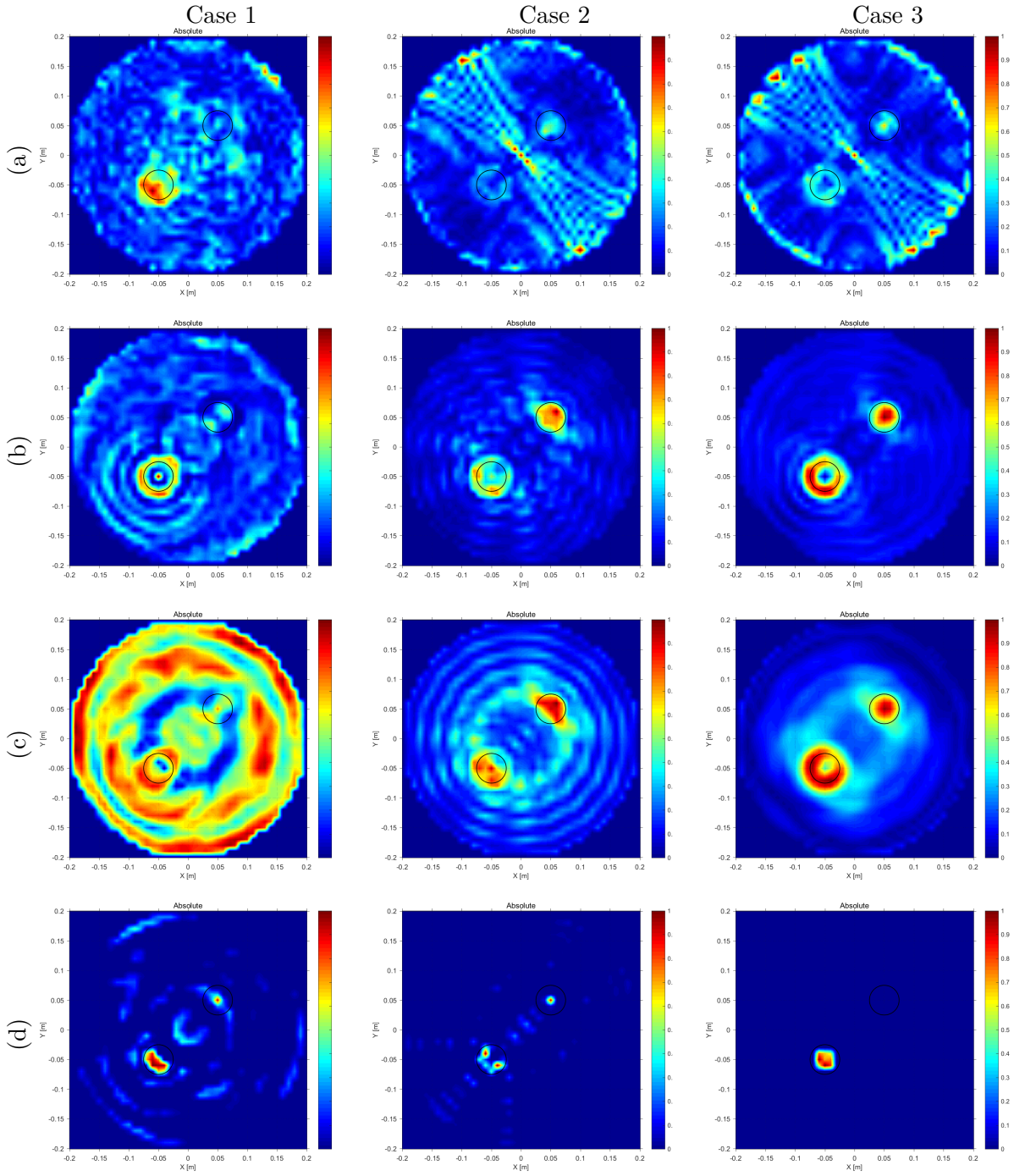

Figure 35: Tomographic images of a PEC and hollow cylinders (a) Conjugate Gradient method, (b) Conjugate Gradient method with modification (c) Algebraic Reconstruction technique (d) Algebraic Reconstruction technique with modification.

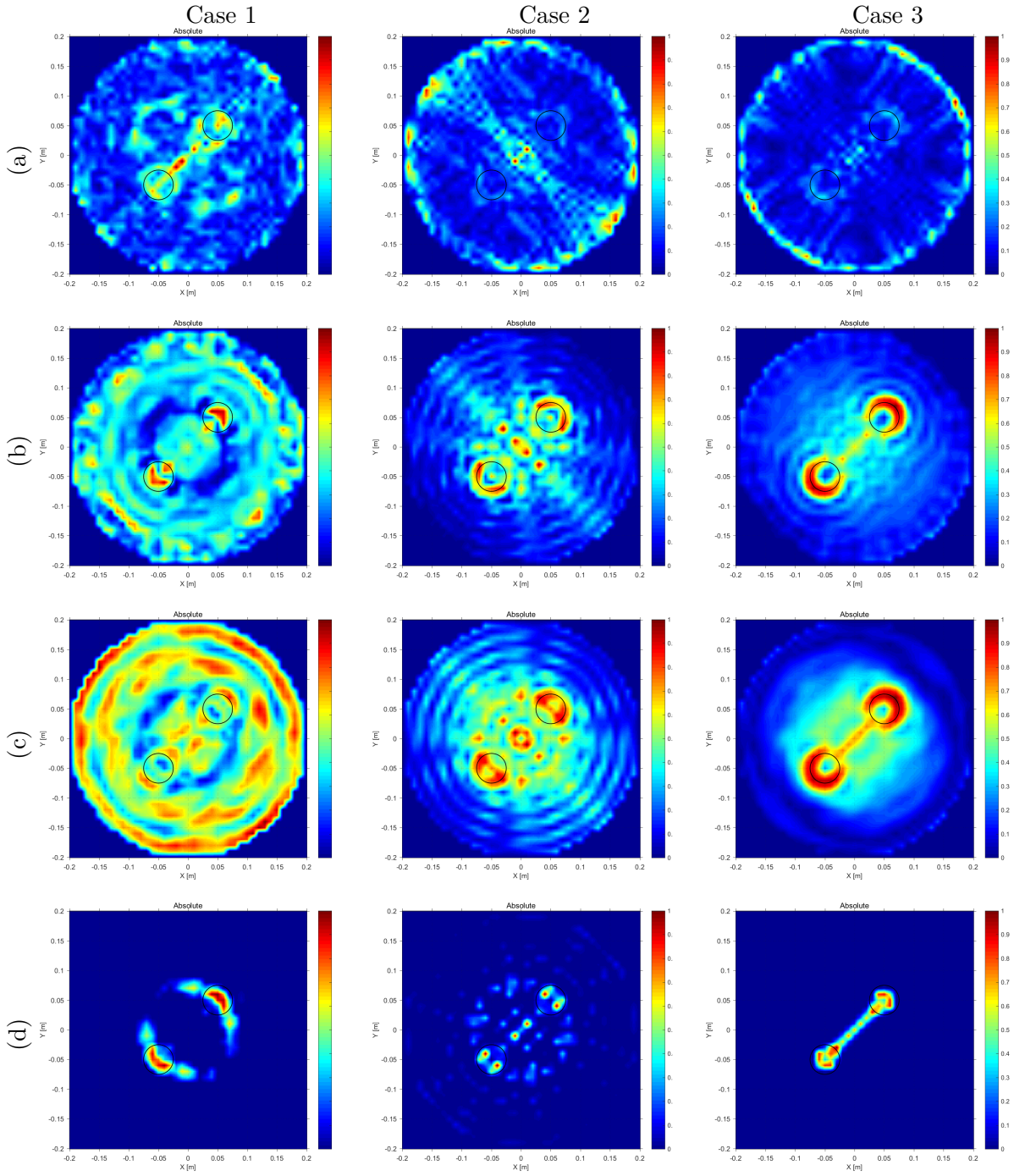

Figure 36: Tomographic images of two circular PEC cylinders with a rectangular PEC cylinder (a) Conjugate Gradient method, (b) Conjugate Gradient method with modification (c) Algebraic Reconstruction technique (d) Algebraic Reconstruction technique with modification.

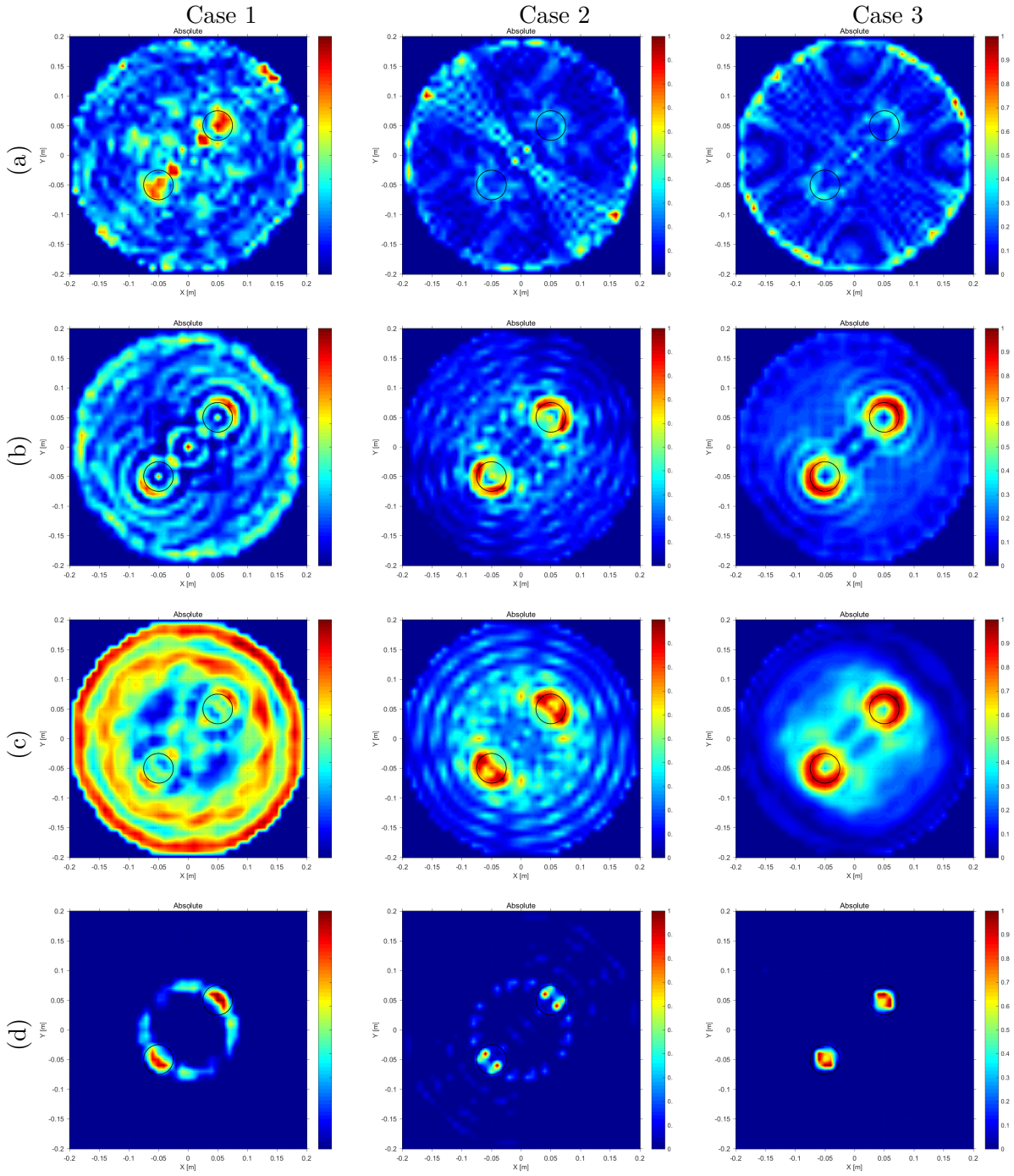

Figure 37: Tomographic images of two circular PEC cylinders with a rectangular hollow cylinder (a) Conjugate Gradient method, (b) Conjugate Gradient method with modification (c) Algebraic Reconstruction technique (d) Algebraic Reconstruction technique with modification.

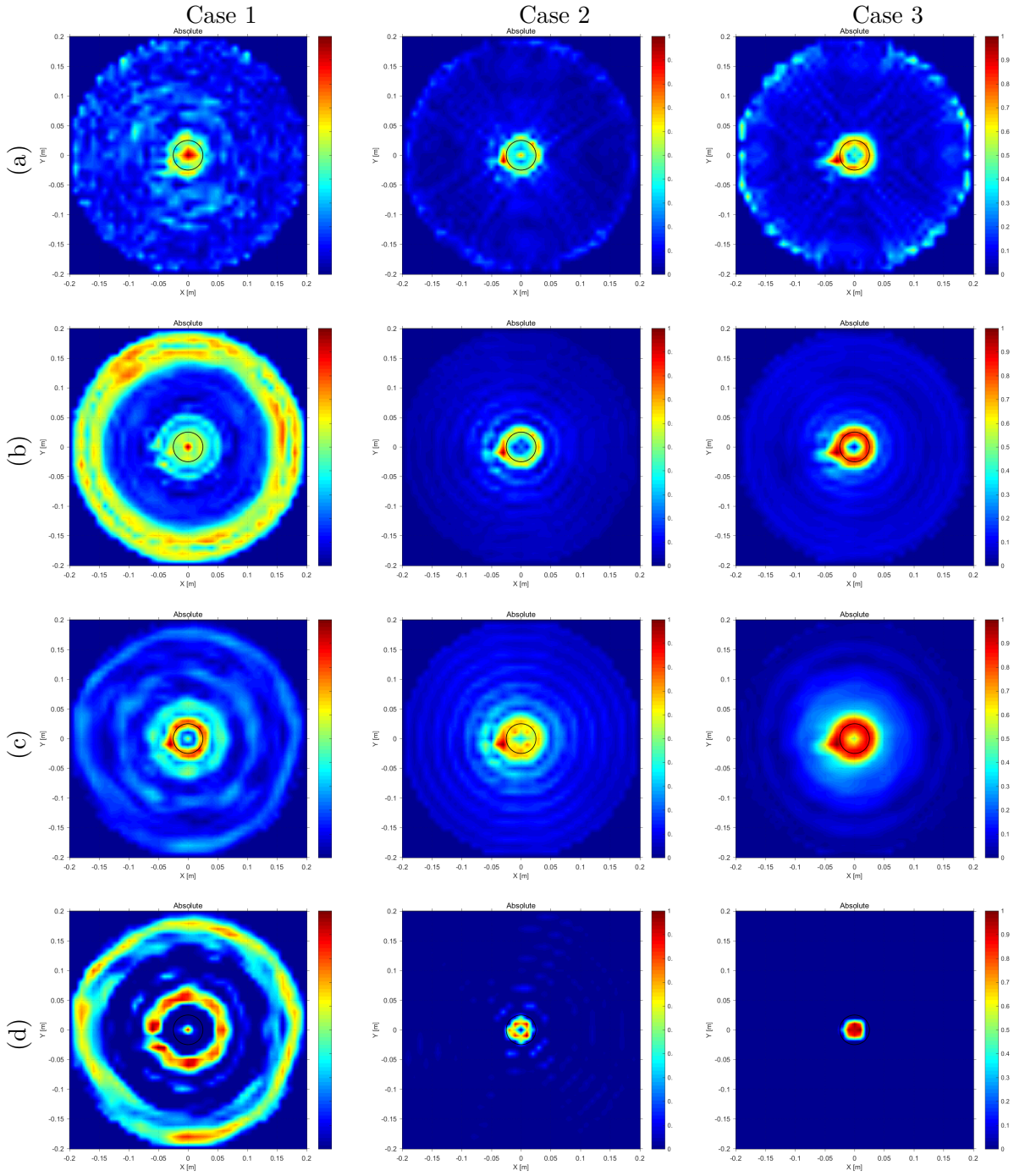

Figure 38: Tomographic images of a PEC cylinder with a crack (a) Conjugate Gradient method, (b) Conjugate Gradient method with modification (c) Algebraic Reconstruction technique (d) Algebraic Reconstruction technique with modification.

Tomographic images using Conjugate Gradient method and Algebraic Reconstruction Technique are provided in Figure 35 through Figure 38. Tomographic images with and without the constrains are also shown.

By comparison of reconstructing results in (a) and (b), we observe that the the modifications actually helps the image qualities for the Conjugate Gradient method. Conjugate Gradient method is usually stable, however it fails to reconstruct images in many test cases. It is probably because the calculation reached a solution which is the undesired solution. Inversion algorithms are often trapped by local minimum solutions, and we need a good reason to avoid such solutions. The modification introduced in (b) is rational and helped avoiding the local minimum solution.

On the other hand, reconstructing results using Algebraic Reconstruction Technique are shown in in (c) and (d). Because the iteration step is necessary to be small, the iteration step is chosen as $\alpha = 10^{-4}$ for this test. The modification in the Algebraic Reconstruction Technique tends to provide very unique result with severe reduction of artifacts. Even though we often must be careful with the results, it could be useful to identify largest scatter in the scene.

5.2 Experimental examples of RF Tomography

RF Tomography using experimental data is provided in this section. The RF Tomography measuring system as shown in Figure 39 is designed by Dr. Vittorio Picco (1), and the setup is extended to use of a box filled with sand or gravel in this thesis. The positioning system allow movements of transmitting (TX) and receiving (RX) halfwave dipoles of frequncy 3.14 GHz independently in circular paths as two arms are controlled by two stepper motors and a controller. The A Vector Network Analyzer (HP 8753ES) collects the scattering parameter S_{21}. Automatic meaurements are programmed using LabVIEW (104), and the controller for motor and the Network Analyzer are controlled by a computer.

As shown in Figure 40 (a), a supporting structure made of Polyvinyl chloride (PVC) is placed from axis of the positioning system. A wooden box is settled on top the supporting structure. TX, RX antennas and half the height of the box are carefully adjusted at the same height. During a measurement, TX and RX antennas move around the box while the box stays at same position.

Scattered field is extracted from background subtraction procedure in the experiment. The procedure is following.

1. Place copper cylinders or Styrofoam blocks in the box and cover them with sand or gravel as shown in Figure 40 (a).

2. Perform first set of measurements are performed by the RF Tomography measuring system. The corresponding measured S_{21}^t has meaning of total field.

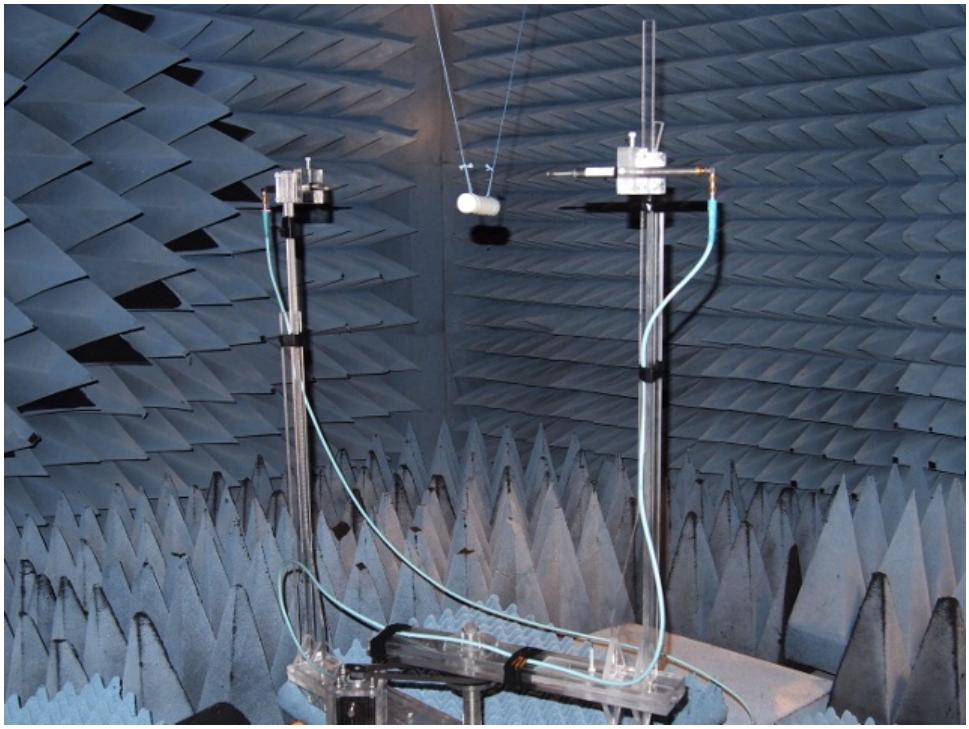

Figure 39: Picture of RF Tomography measuring system. ©2014 by Vittorio Picco (1).

3. Remove only the buried objects, copper cylinders or Styrofoam blocks while the background medium, sand or gravel stays filled. The corresponding measured S_{21}^{i} has meaning of incident field which contains also scattered field from the box. The strings are used to pull out only objects in Figure 40.

4. Find scattering parameter associated with scattered field S_{21}^{s} by subtracting scattering parameters S_{21}^{i} from S_{21}^{t}.

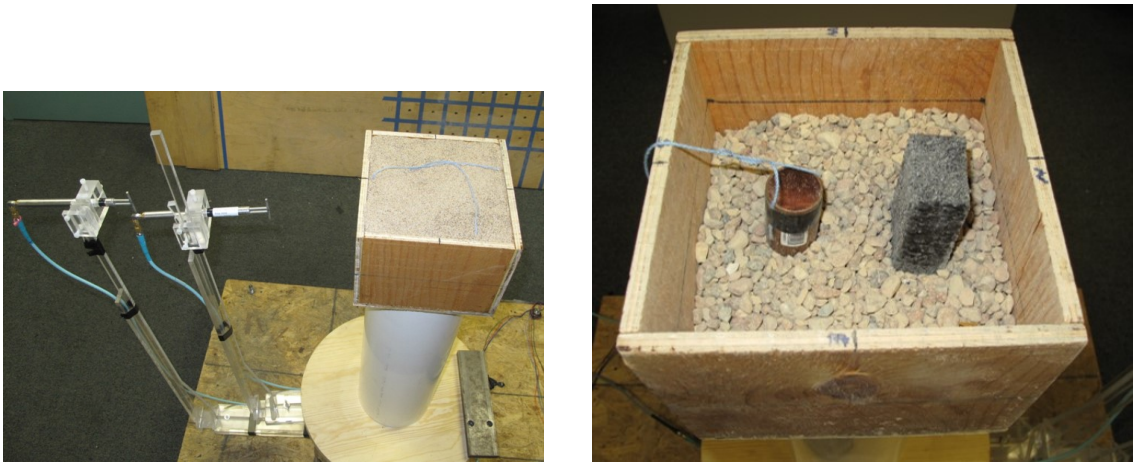

(a) (b)

Figure 40: Experimental setup.

5. Normalize the extracted scattering parameter S^s_{21} by ratio of $S^i_{21,\text{Freespace}}$ and analytical solution $E^i_{\text{Freespace}}$ of freespace. The reference measurement of freespace for $S^i_{21,\text{Freespace}}$ is performed by removing the box from the scene.

The procedure turns into the equation of

$$E^s = \frac{E^i_{\text{Freespace}}}{S^i_{21,\text{Freespace}}}(S^t_{21} - S^i_{21}). \tag{5.4}$$

The box filled with sand or gravel is treated as background and part of incident field, also forward model is constructed for the background. Method of Moment simulations by FEKO are used to produce Green's functions and forward model. In the simulations, ideal dipoles

are located at TX and RX positions, and a forward model is constructed from meaning of reciprocity for RX side.

Procedure to produce forward model is as follows.

1. Place a block of dielectric cube with size of the box in FEKO simulation, and compute electric fields within the dielectric medium due to the TXs.This provide $\mathbf{E}^{\mathrm{i}}(\mathbf{r}', \mathbf{r}^{\mathrm{t}})$ in 2.28.

2. Compute electric fields within the dielectric medium the from RXs are computed, and converted into Green's function. The conversion is perfomed by

$$\mathbf{a}^{\mathrm{r}} \cdot \underline{\underline{\mathbf{G}}}(\mathbf{r}^{\mathrm{r}}, \mathbf{r}') = \frac{j}{\omega \mu_0} \mathbf{E}^{\mathrm{i}}(\mathbf{r}', \mathbf{r}^{\mathrm{r}}) \tag{5.5}$$

   where $\mathbf{r}^{\mathrm{r}}$ and $\mathbf{r}'$ are exchanged by meaning of reciprocity.

3. Construct a forward model for the background medium of dielectric block by implementing

$$E^s(\mathbf{r}^{\mathrm{r}}, \mathbf{r}^{\mathrm{t}}) = k_0^2 \iiint_D \mathbf{a}^{\mathrm{r}} \cdot \underline{\underline{\mathbf{G}}}(\mathbf{r}^{\mathrm{r}}, \mathbf{r}') \cdot \mathbf{E}^{\mathrm{i}}(\mathbf{r}', \mathbf{r}^{\mathrm{t}}) \varepsilon_\delta \mathbf{r}'. \tag{5.6}$$

   System matrix $\mathbf{L}$ is produced by partitioning the region D into voxels.

The wooden box has outer to outer size of 20×20 in xy-plane, and height of 15 cm with 1 cm thickness of walls. Hollow copper cylinders of radius 1 cm and height 5 cm or blocks of Styrofoam with size of 2×3 cm with height of 5 cm are used in the experiments. Those objects are completely covered.

The RF Tomography measuring system collects 220 measurements of scattering parameter for 11 TXs and 20 RXs. The TX half-wave dipole is located at 44.5 cm ($\approx 4.7\lambda$) away from center of movement, and the RX half-wave dipole is located 23.1 cm ($\approx 2.4\lambda$) away from center of movement. The positioning system is allowed to move arms of 360° and 280° angles for TX and RX. Figure 41 indicates the locations of TX and RX antennas for the measurement as red circles and blue diamonds, respectively. The antennas are located at TX (0, 44.5) cm and RX (0, 23.1) cm at beginning, and they move clockwise during the measurements.

The scattered field and forward model are prepared by a procedure as mentioned before. When the forward model is constructed, a block of dielectric medium is assumed with relative permittivity of 2.5 for sand and 2 for gravel, and size of the box which is 20×20 in xy-plane and height of 15 cm.

Tomographic images are produced for eight cases of geometries, a copper cylinder, two copper cylinders, a block of Styrofoam, and two blocks of Styrofoam buries in each which are covered with sand or gravel. After the reconstruction, tomographic images are normalized to its maximum.

5.2.1 Styrofoam blocks buried in a medium

Tomographic example of Styrofoam blocks are provided. Since the forward model corresponds to Born approximation, we expect artifact due to multiple scattering. However, sand and Styrofoam must have similar properties of permittivity, so the Born approximation could be a good approximation for this case.

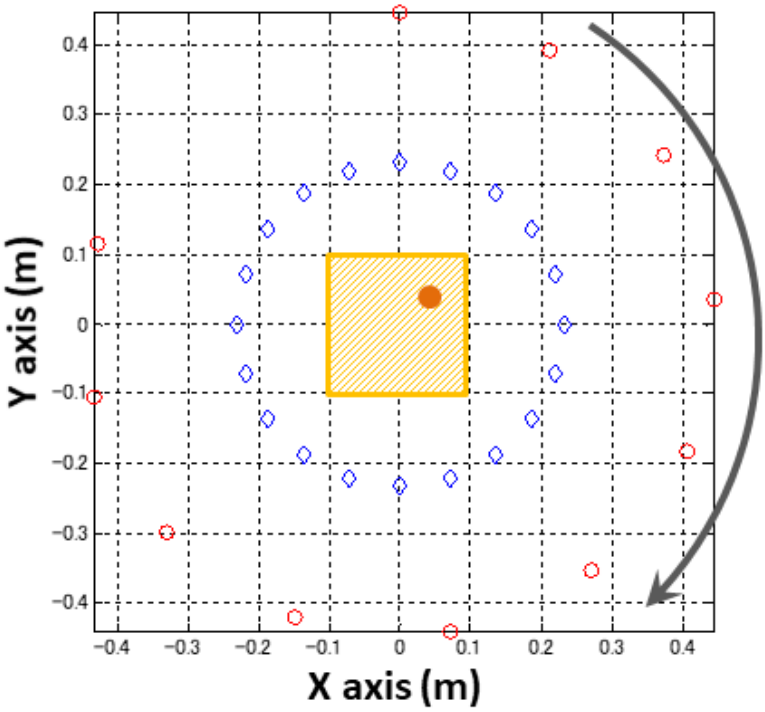

Figure 41: TX (red circle), RX (blue diamonds) antenna and the box (Yellow square) locations in xy-plane for the experiment.

Figure 42 through Figure 45 show reconstructing tomographic results using Conjugate Gradient and Algebraic Reconstruction Technique. Styrofoam blocks are well reconstructed in overall. In particular,

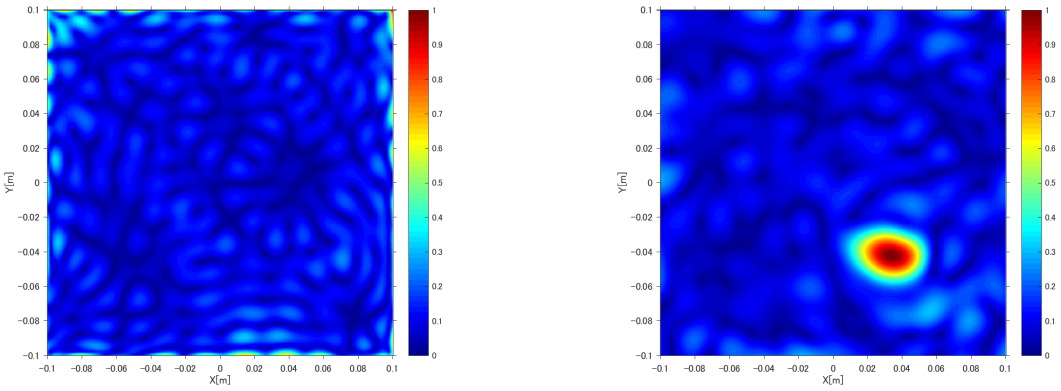

(a)

(b)

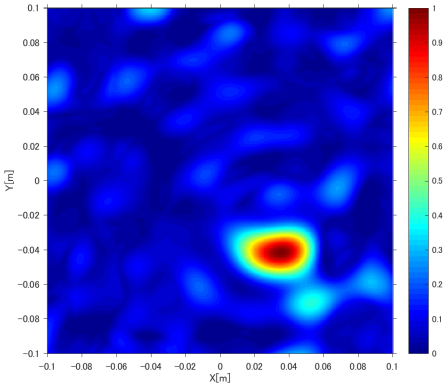

(c)

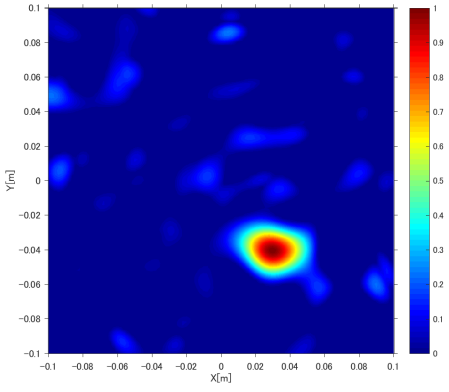

(d)

Figure 42: A Styrofoam block buried in sand using (a) Conjugate Gradient method, (b) Conjugate Gradient method with modification (c) Algebraic Reconstruction technique (d) Algebraic Reconstruction technique with modification ©2016 IEEE (6).

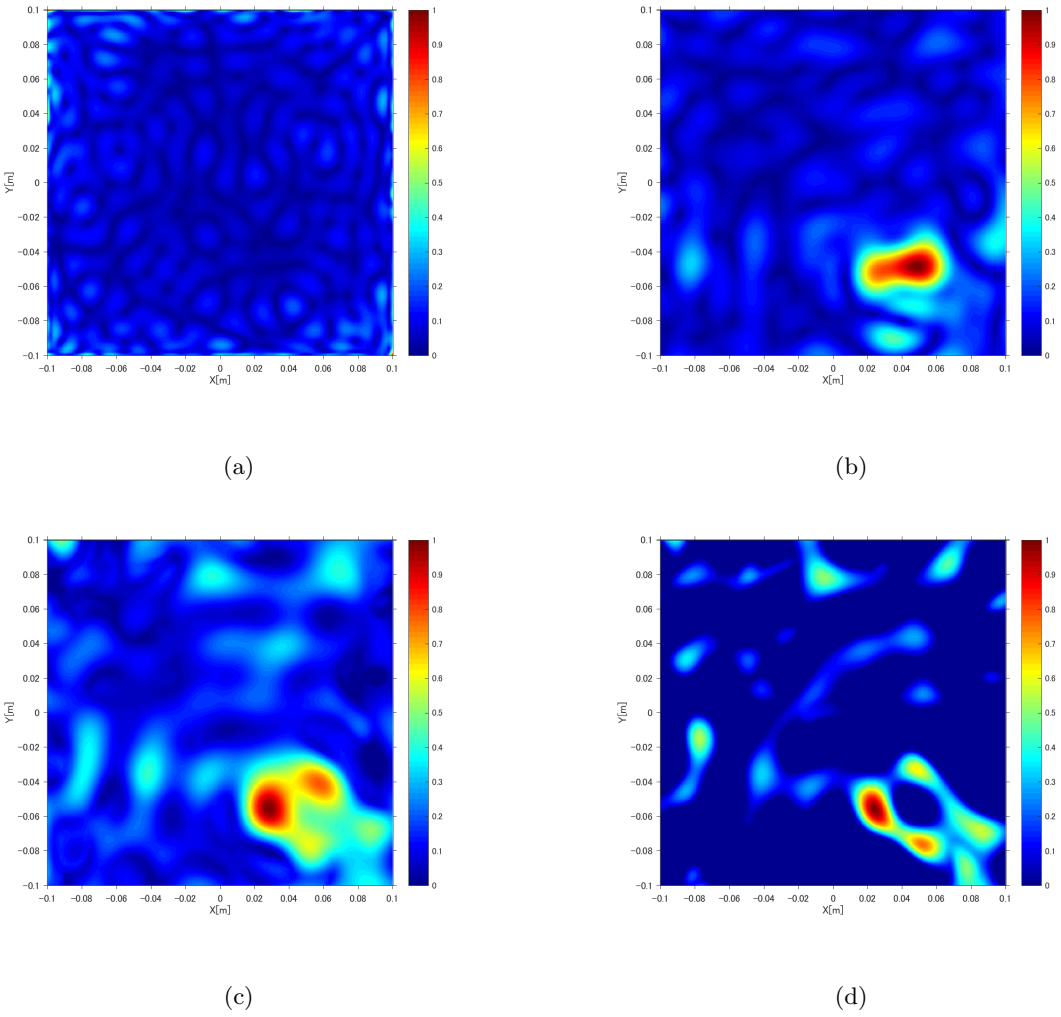

Figure 43: A Styrofoam block buried in gravel using (a) Conjugate Gradient method, (b) Conjugate Gradient method with modification (c) Algebraic Reconstruction technique (d) Algebraic Reconstruction technique with modification ©2016 IEEE (6).

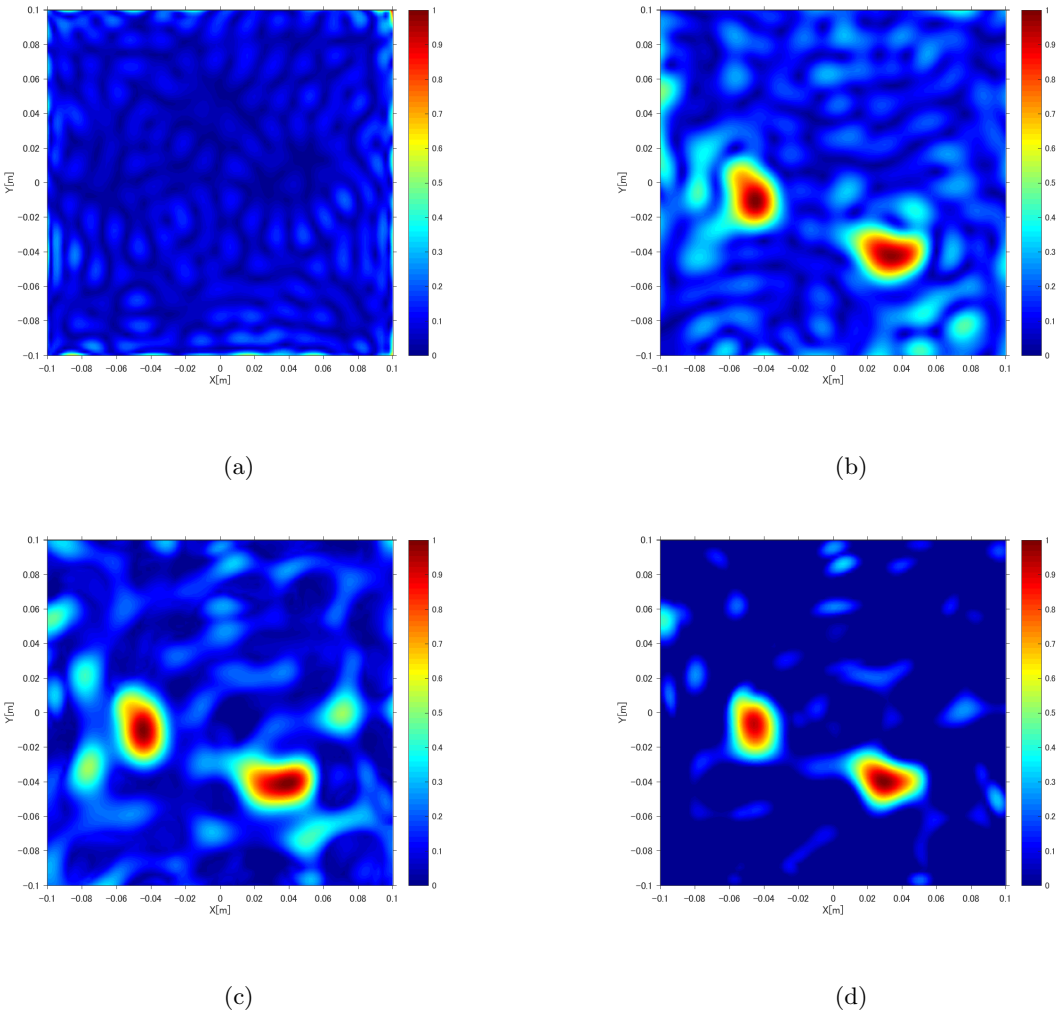

Figure 44: Two Styrofoam blocks buried in sand using (a) Conjugate Gradient method, (b) Conjugate Gradient method with modification (c) Algebraic Reconstruction technique (d) Algebraic Reconstruction technique with modification ©2016 IEEE (6).

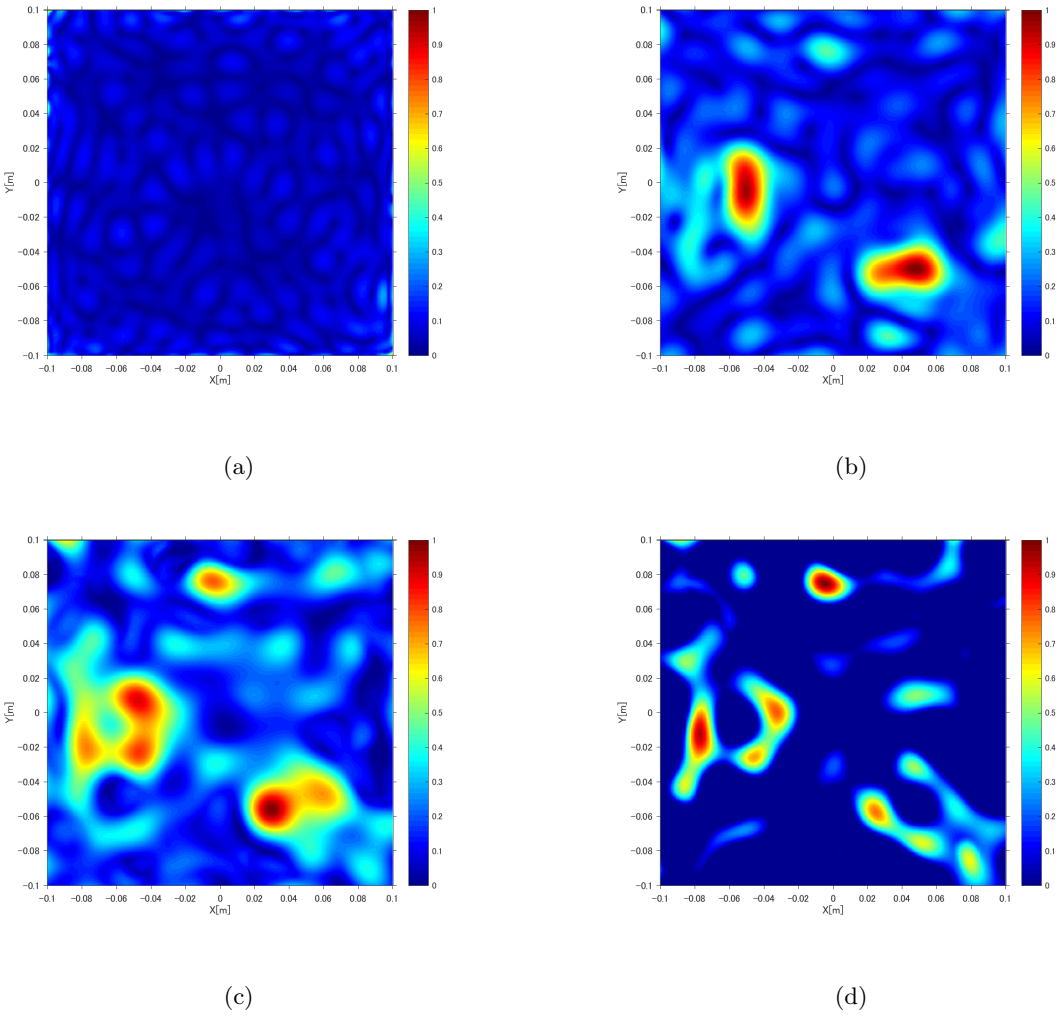

Figure 45: Two Styrofoam block buried in gravel using (a) Conjugate Gradient method, (b) Conjugate Gradient method with modification (c) Algebraic Reconstruction technique (d) Algebraic Reconstruction technique with modification ©2016 IEEE (6).

5.2.2 Copper cylinders buried in a medium

Figure 46 through Figure 49 show reconstructing tomographic images using Conjugate Gradient and Algebraic Reconstruction Technique. Reconstruction of metallic objects are more challenging in RF Tomography because large scatterer does not satisfy Born approximation, and usually requires more accurate forward model such as quadratic model to take into account multiple scattering phenomenon.

Even though there are artifacts in the scene, we are still able to identify locations of copper cylinders. The artifact tends to appear between the actual locations of cylinders and wall of wooden box.

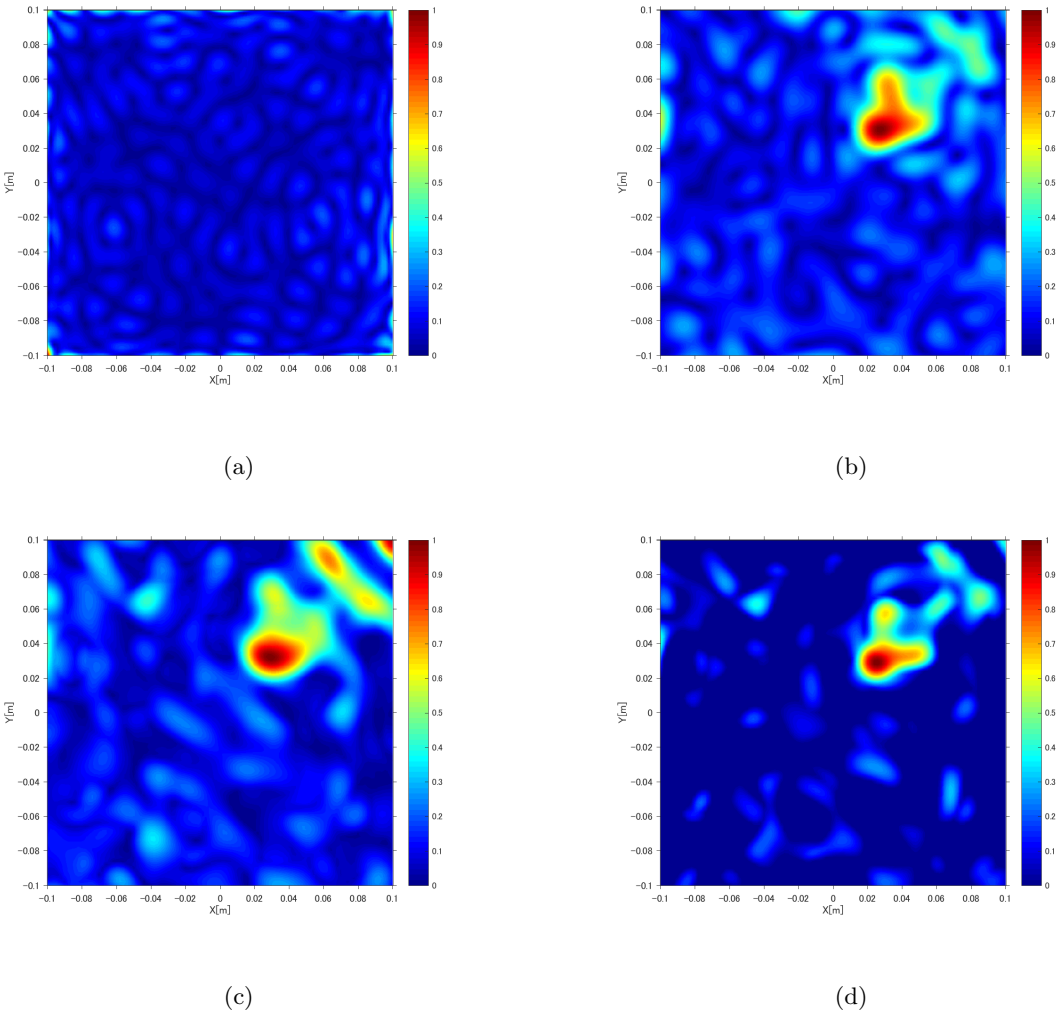

Figure 46: A copper cylinder buried in sand using (a) Conjugate Gradient method, (b) Conjugate Gradient method with modification (c) Algebraic Reconstruction technique (d) Algebraic Reconstruction technique with modification ©2016 IEEE (6).

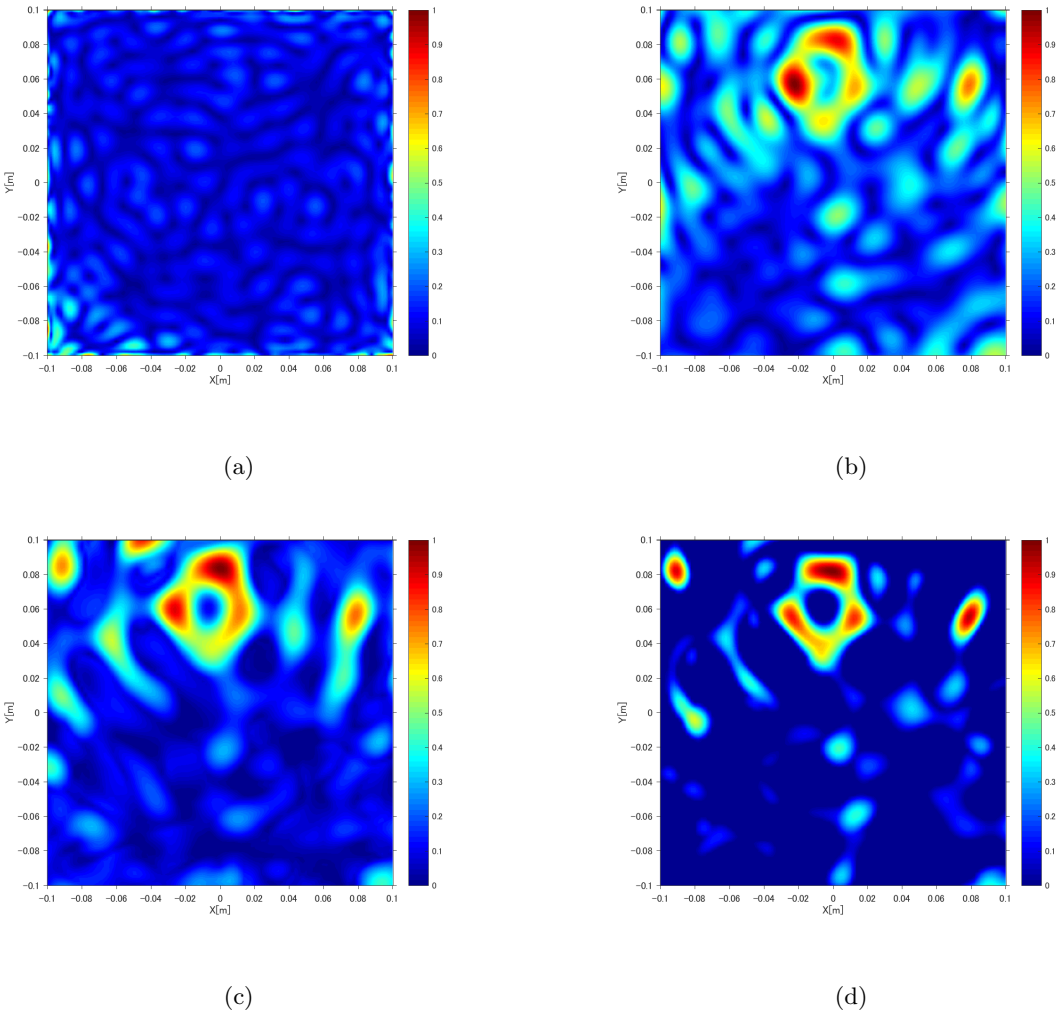

Figure 47: A copper cylinder buried in gravel using (a) Conjugate Gradient method, (b) Conjugate Gradient method with modification (c) Algebraic Reconstruction technique (d) Algebraic Reconstruction technique with modification ©2016 IEEE (6).

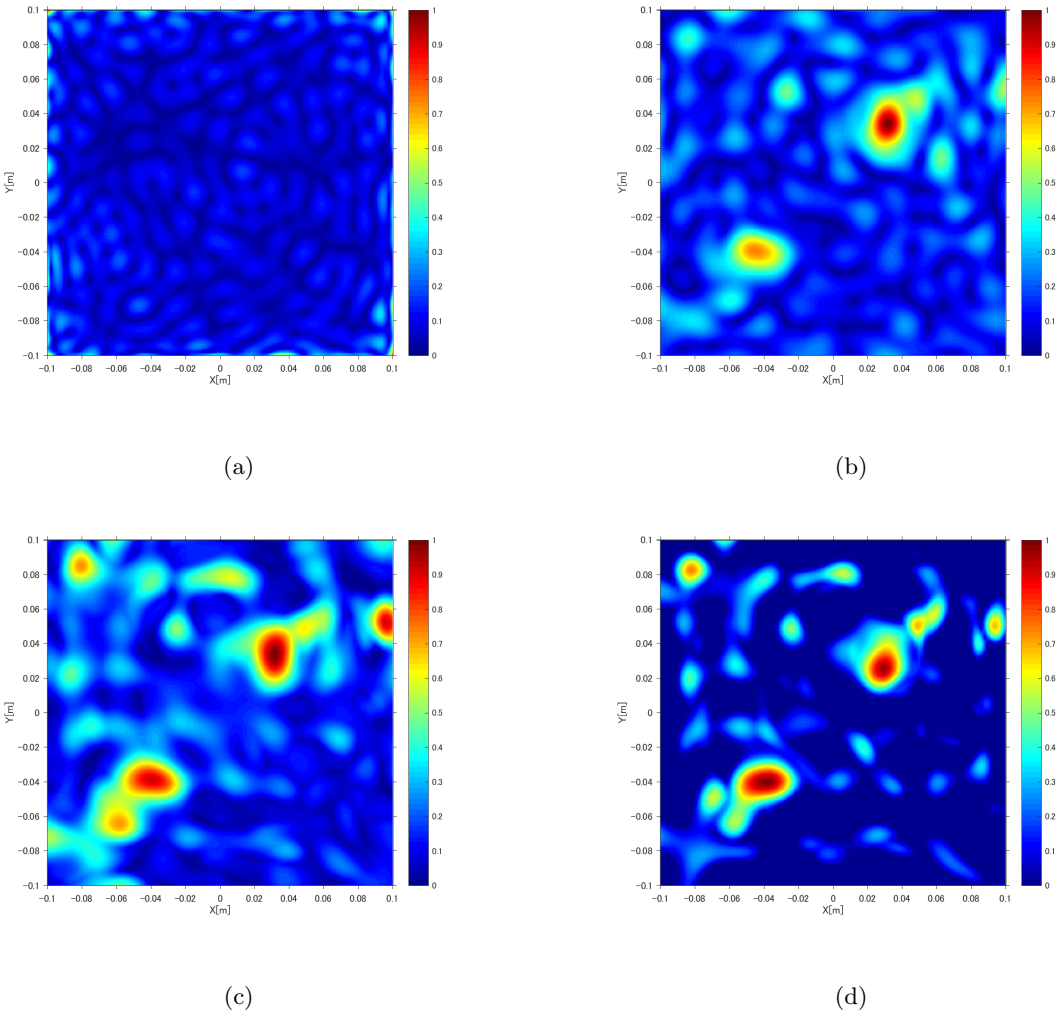

Figure 48: Two copper cylinders buried in sand using (a) Conjugate Gradient method, (b) Conjugate Gradient method with modification (c) Algebraic Reconstruction technique (d) Algebraic Reconstruction technique with modification ©2016 IEEE (6).

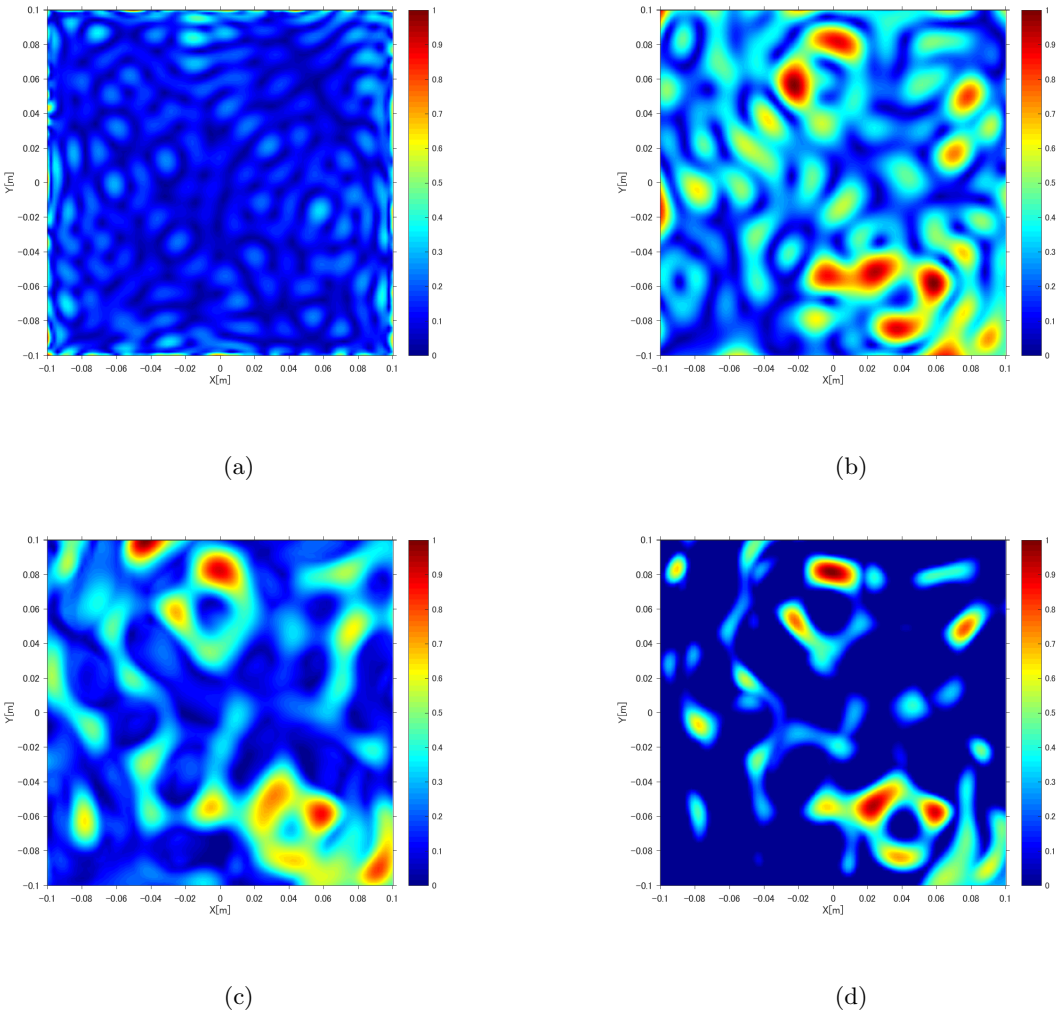

Figure 49: Two copper cylinders buried in gravel using (a) Conjugate Gradient method, (b) Conjugate Gradient method with modification (c) Algebraic Reconstruction technique (d) Algebraic Reconstruction technique with modification ©2016 IEEE (6).

5.2.3 Material recognition by real and imaginary part of reconstructed contrast

The reconstructed images provide potential usage of identifying object type between metallic and dielectric contrast. Resulting reconstructed contrast $\mathbf{v}$ is normalized in the range between 0 and 1 in absolute values, but also real and imaginary part of the contrast are in the range between -1 and 0 by modification used in Algebraic Reconstruction Technique.

Figure 50 and Figure 51 shows images of real part of the resulting contrast $\mathbf{v}$ in addition to its absolute quantity. The range of plot are fixed between 0 and 1 for absolute value $\mathbf{v}$ and -1 and 0 for real Re($\mathbf{v}$) and imaginary part Im($\mathbf{v}$) of the reconstructed contrast. Recalling the contrast as

$$v(\mathbf{r}') = \varepsilon_r(\mathbf{r}') - \varepsilon_b + j\frac{(\sigma(\mathbf{r}') - \sigma_b)}{2\pi f \varepsilon_0}, \tag{5.7}$$

where I assumed $\varepsilon_b \approx 2.5$ and $\sigma_b \approx 0$, the contrast must have real quantity for Styrofoam objects and imaginary for copper objects. One may observe the expected behavior in reconstructed images. If further development of RF Tomography is achieved to reduce the artifacts, we may use the phenomenon to distinguish between crack and reinforcing bars. RF Tomography may provide unique information to inspection of reinforced concrete, potentially finding internal crack and associated corrosion.

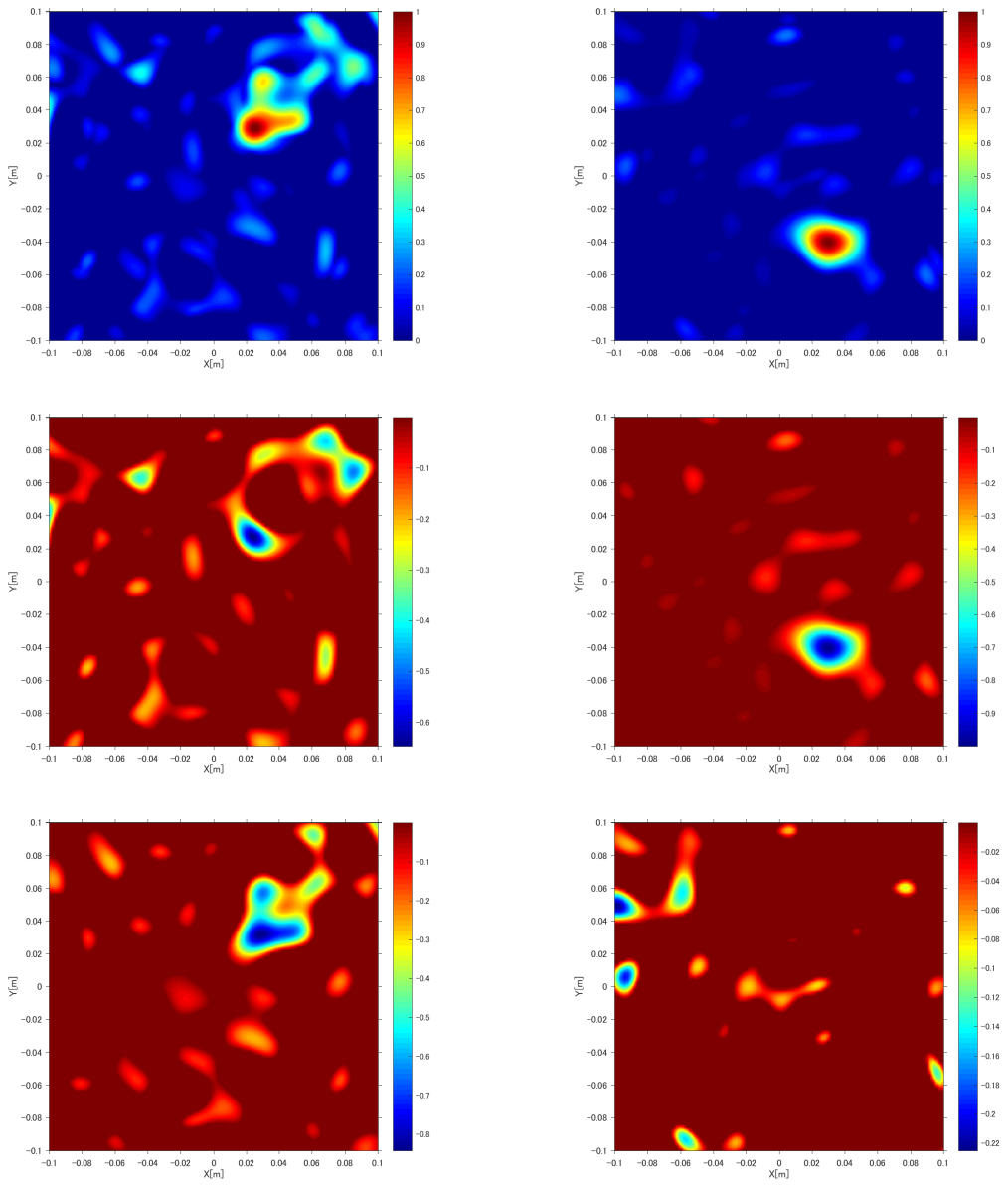

Figure 50: Reconstructed images of a copper cylinder (left) and a block of Styrofoam (right) using Algebraic Reconstructions Technique with physical constraints, for (top) absolute quantity $|\mathbf{v}|$, (middle) real quantity $\mathrm{Re}(\mathbf{v})$, (bottom) imaginary quantity $\mathrm{Im}(\mathbf{v})$ (6).

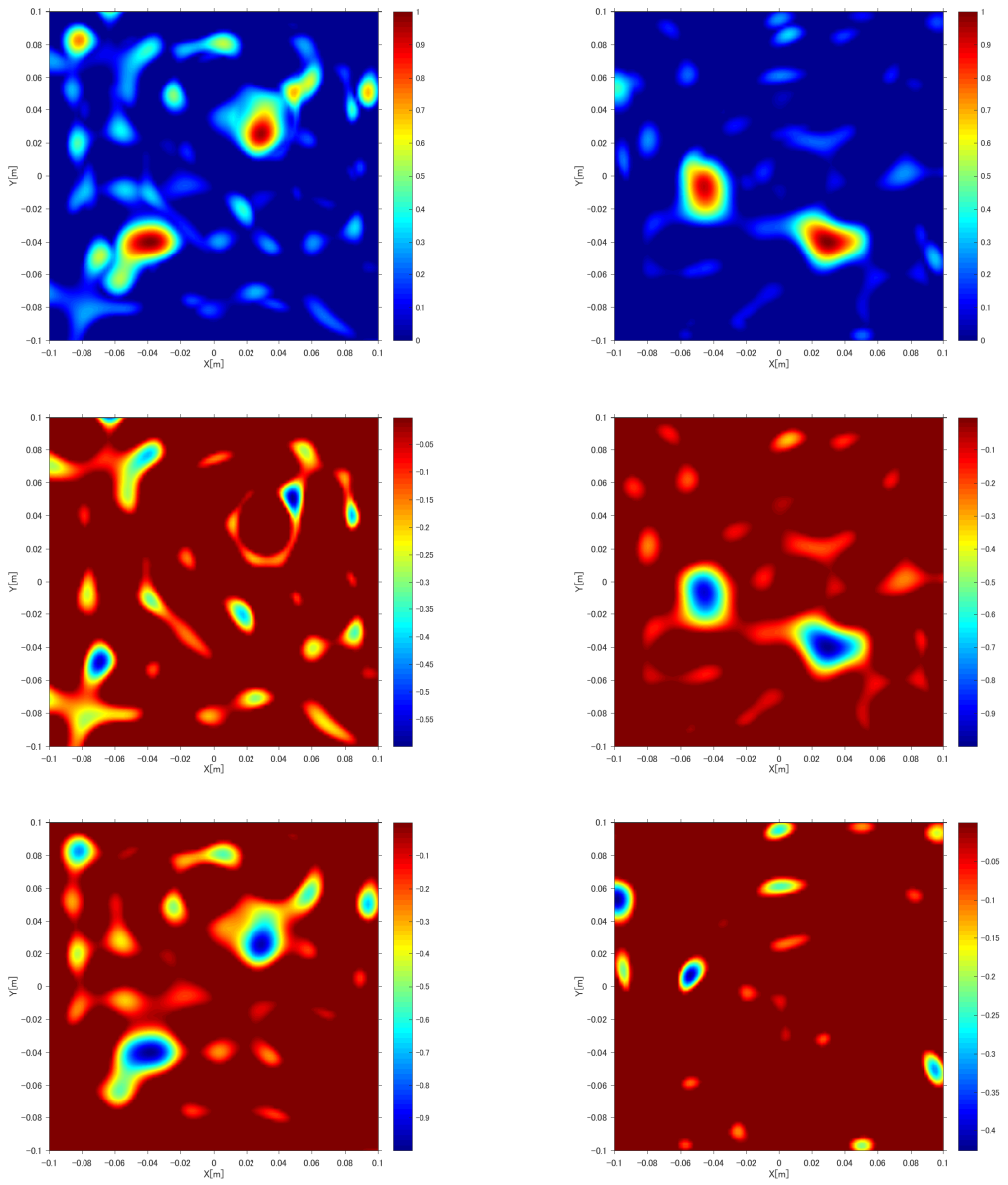

Figure 51: Reconstructed images of two copper cylinders (left) and two blocks of Styrofoam (right) using Algebraic Reconstructions Technique with physical constraints, for (top) absolute quantity $|\mathbf{v}|$, (middle) real quantity $\mathrm{Re}(\mathbf{v})$, (bottom) imaginary quantity $\mathrm{Im}(\mathbf{v})$ ©2016 IEEE (6).

CHAPTER 6

CONCLUSION

Chapter 1 introduced technical challenges of monitoring bridges and provided review of existing diagnostic techniques for structural health of bridge.

Chapter 2 reviewed the theoretical background of RF Tomography and inversion techniques. The forward models are derived starting from a set of Maxwell equations. In particular, it covered implementation of the forward models in two and three dimensional geometries using Born approximation, which produced linear system matrices. Inversion techniques such as Truncated Singular Value Decomposition, Conjugate Gradient method, and Algebraic Reconstruction Technique were introduced as regularized inverse techniques which are used in later chapters.

Chapter 3 developed forward model for reinforced concrete structure. A reinforced concrete structure is modeled as a two dimensional dielectric cylinder. The analytical solution for a dielectric cylinder due to a line source is derived, and used to form the forward model.

Chapter 4 was dedicated to analyze the resolutions of the three configurations, Case 1: Multi-Monostatic/Muti-frequency, Case 2: Multi-static/Single-frequency, and Case 3: Multi-static/Multi-frequency configurations. While system matrices were produced from forward models based on Born approximation, the resolution analysis was performed to examine how well the system matrices were able to produce. In order to achieve this purpose, scattered field

data sets were produced from the forward calculation of the system matrices with the Born approximation other than solving real full wave electromagnetic scattered fields.

First, justification of operating frequency for case 2 was provided. Condition number, electric field distribution, L-curve, and point spread function were discussed to justify selected operating frequency for the case 2 configuration. The reconstructed results for some frequencies failed to reconstruct images which implied importance of using multi-frequencies.

Second, resolution analyses for three configurations were provided. Test 1 was made of same size of system matrices for case 1 and case 2 configurations so that they could avoid a problem of normalization for comparison. The comparison of case 1 and case 2 gave a comparison of multi-monostatic and muti-static configurations, equivalently Ground Penetrating Radar and RF Tomography configurations. It concluded that multi-static configurations had superior reconstructing results.

Third, the number of frequencies for the Case 1 configuration was increased. More equations for its system matrix were produced than the Case 2 had in the previous test. It confirmed that more numbers of frequencies within the same range of the frequency band actually did not provide improvements. Therefore, it justified that muti-static configuration is the key to improve image qualities.

Finally, resolution analyses for tomographic example was provided in Chapter 5.

Chapter 5 provided tomographic examples of RF Tomography with inhomogeneous background medium from numerical and experimental scattered fields.

First section used Method of Moment simulations to produce scattered field for RF Tomography. Test setups were chosen as same as Section 4.3 of Chapter 4. PEC and hollow cavity cylinders were placed on the xy-plane, and commercial software FEKO computed electromagnetic fields in two dimensions by the feature of periodic structure. Reconstructed images for three case configurations defined in Chapter 4 were presented, and their image qualities are compared. The multi-static/multi-frequency configurations provide less artifacts and clearer images. In particular, it is critical when the noise is added to scattered field. It also provided reconstructed images by iterative regularization inverse methods, Conjugate Gradient method, and Algebraic Reconstruction Technique. Constraints based on physics were introduced in iterative methods which helped to obtain favorable results.

Second section used experimentally obtained scattered fields for RF Tomography. Experiments were conducted by RF Tomography measuring system at the Andrew Electromagnetics Laboratory of University of Illinois at Chicago. The measuring system was upgraded to use a wooden box that could set up experiments for buried objects within a medium. The test cases involved copper cylinders or Styrofoam blocks buried in sand or gravel. While clearer images were achieved in reconstructing Styrofoam, many artifacts are produced in reconstructing copper cylinders. It is expected because the forward model corresponded to the Born approximation, and multiple scattering due to wooden wall are ignored.

Future work

Quadratic model with inhomogeneous Green's function We have observed that some reconstructed images for metallic objects had larger artifacts than the images for dielectric

objects had. In this thesis, it focused on the forward models using Born approximation which ignored multiple scattering due to the metallic objects. One suggests to implement the quadratic forward model to consider the multiple scattering phenomenon in the inverse problem, and preliminary results are shown in (43). In order to obtain improve the reconstructed images comparing to the Born approximation forward model, following consideration must be overcome.

- Computational resource for the quadratic forward model: A quadratic forward model takes into account double scattering phenomena. The phenomenon can be included by internal operator explained in (1). The internal operator has square matrix of number of unknown contrast. The internal operator could be large matrix and time costly, in particular when multiple frequencies are used. In Chapter 3, analytical solution due to a line source located within a dielectric cylinder which can be used to produce the internal operator for the background medium.
- Regularized inversion for quadratic model: Quadratic model is more accurate forward model, however no longer any regularized inverse techniques are available. Even though the forward model would be more accurate, not regularized solutions would provide poor image reconstructions.

Method of background subtraction: One of the technical challenge is to extract scattered electric field from experimental measurement setup which provide total electric field. In Ground Penetrating Radar, we may use time gating technique to remove the first refection. In RF Tomography, this thesis used method of background subtraction, however incident field must be estimated numerically inspection in real world.

Appendices

Appendix A

COPYRIGHT PERMISSIONS

In this appendix we present the copyright permissions for the articles and contents that were used in this thesis. Some experiments and reconstructed images are published in 2016 URSI International Symposium on Electromagnetic Theory (EMTS)(6), and that copyright belongs to IEEE. The statement of the copyright permission is in following page.

Title: Experimental validation of Radio Frequency Tomography for an inhomogeneous medium

Conference Proceedings: Electromagnetic Theory (EMTS), 2016 URSI International Symposium on

Author: Tadahiro Negishi

Publisher: IEEE

Date: Aug. 2016

Thesis / Dissertation Reuse

The IEEE does not require individuals working on a thesis to obtain a formal reuse license, however, you may print out this statement to be used as a permission grant:

Requirements to be followed when using any portion (e.g., figure, graph, table, or textual material) of an IEEE copyrighted paper in a thesis:

1) In the case of textual material (e.g., using short quotes or referring to the work within these papers) users must give full credit to the original source (author, paper, publication) followed by the IEEE copyright line © 2011 IEEE.
2) In the case of illustrations or tabular material, we require that the copyright line © [Year of original publication] IEEE appear prominently with each reprinted figure and/or table.
3) If a substantial portion of the original paper is to be used, and if you are not the senior author, also obtain the senior author's approval.

Requirements to be followed when using an entire IEEE copyrighted paper in a thesis:

1) The following IEEE copyright/ credit notice should be placed prominently in the references: © [year of original publication] IEEE. Reprinted, with permission, from [author names, paper title, IEEE publication title, and month/year of publication]
2) Only the accepted version of an IEEE copyrighted paper can be used when posting the paper or your thesis on-line.
3) In placing the thesis on the author's university website, please display the following message in a prominent place on the website: In reference to IEEE copyrighted material which is used with permission in this thesis, the IEEE does not endorse any of [university/educational entity's name goes here]'s products or services. Internal or personal use of this material is permitted. If interested in reprinting/republishing IEEE copyrighted material for advertising or promotional purposes or for creating new collective works for resale or redistribution, please go to http://www.ieee.org/publications_standards/publications/rights/rights_link.html to learn how to obtain a License from RightsLink.

If applicable, University Microfilms and/or ProQuest Library, or the Archives of Canada may supply single copies of the dissertation.

CITED LITERATURE

1. Picco, V.: Dyadic Contrast Function And Quadratic Forward Model For Radio Frequency Tomography. Doctoral dissertation, University of Illinois at Chicago, Chicago, IL, May 2014.

2. Persico, R., Bernini, R., and Soldovieri, F.: The role of the measurement configuration in inverse scattering from buried objects under the Born approximation. IEEE Transactions on Antennas and Propagation, 53(6):1875–1887, 2005.

3. Persico, R., Gennarelli, G., and Soldovieri, F.: GPR prospecting on circular surfaces: preliminary results. In Proceedings of the 15th International Conference on Ground Penetrating Radar, pages 79–82, June 2014.

4. Gennarelli, G., Catapano, I., Soldovieri, F., and Persico, R.: On the Achievable Imaging Performance in Full 3-D Linear Inverse Scattering. IEEE Trans. Antennas Propag., 63(3):1150–1155, March 2015.

5. Gennarelli, G. and Soldovieri, F.: Performance analysis of incoherent RF tomography using wireless sensor networks. IEEE Transactions on Geoscience and Remote Sensing, 54(5):2722–2732, May 2016.

6. Negishi, T., Liu, Y., Picco, V., Erricolo, D., Gennarelli, G., Soldovieri, F., and L.E. Uslenghi, P.: Experimental validation of radio frequency tomography for an inhomogeneous medium. In URSI Commission B International Symposium on Electromagnetic Theory, pages 5–8, Espoo, Finland, August 2016.

7. U. S. Department of Transportation, Federal Highway Administration: Deficient bridges by year built 2016. `https://www.fhwa.dot.gov/bridge/nbi/no10/yrblt16.cfm`. updated: 06-27-2017.

8. U. S. Department of Transportation, Federal HighwayAdministration: Deficient bridges by highway system. `https://www.fhwa.dot.gov/bridge/deficient.cfm`. updated: 06-27-2017.

9. National Transportation Safety Board: Collapse of a suspended span of interstate route 95 highway bridge over the mianus river. `https://www.ntsb.gov/investigations/AccidentReports/Pages/HAR8403.aspx`. updated: 07-19-1984.

10. U. S. Department of Transportation: The collapse of the interstate 35 west bridge over the mississippi river. https://www.transportation.gov/content/collapse-interstate-35-west-bridge-over-mississippi-river-0. updated: 09-20-2007.

11. New York Post: Collapse at brooklyn bridge injures 5 people. http://nypost.com/2014/07/02/collapse-at-brooklyn-bridge-injures-5-people/. updated: 07-03-2014.

12. U. S. Department of Transportation, Federal Highway Administration: China earthquake reconnaissance report: Performance of transportation structures during the may 12, 2008, m7.9 wenchuan earthquake observed damage to bridges. https://www.fhwa.dot.gov/publications/research/infrastructure/structures/11029/003.cfm. updated: 03-08-2016.

13. McCann, D. M. and Forde, M. C.: Review of ndt methods in the assessment of concrete and masonry structures. NDT & E International, 34(2), 2001.

14. Gucunski, N., National Research Council, et al.: Nondestructive testing to identify concrete bridge deck deterioration. Transportation Research Board, 2013.

15. Lichtenstein, A., Bakht, B., and Moses, F.: Bridge rating through nondestructive load testing-technical report: Supplement to NCHRP research results digest No. 234. NCHRP Research Results Digest, (234), 1998.

16. Saraf, V., Sokolik, A., and Nowak, A.: Proof load testing of highway bridges. Transportation Research Record: Journal of the Transportation Research Board, 1541:51–57, 1996.

17. Colla, C., Das, P. C., McCann, D., and Forde, M.: Sonic, electromagnetic and impulse radar investigation of stone masonry bridges. NDT & E International, 30(4):249–254, 1997.

18. Zhang, J.-K., Yan, W., and Cui, D.-M.: Concrete condition assessment using impact-echo method and extreme learning machines. Sensors, 16(4):447, 2016.

19. Zaki, A., Chai, H. K., Aggelis, D. G., and Alver, N.: Capability of acoustic emission technique. 15(8):19069–19101, 2015.

20. Song, H.-W. and Saraswathy, V.: Corrosion monitoring of reinforced concrete structures-a. International Journal of Electrochemical Science, 2:1–28, 2007.

21. Verma, K. S., Bhadauria, S. S., and Akhtar, S.: Monitoring corrosion of steel bars in reinforced concrete structures. The Scientific World Journal, 2014, 2014.

22. Elsener, B., Andrade, C., Gulikers, J., Polder, R., and Raupach, M.: Hall-cell potential measurements - potential mapping on reinforced concrete structures. Materials and Structures, 36(7):461–471, 2003.

23. Bagavathiappan, S., Lahiri, B., Saravanan, T., Philip, J., and Jayakumar, T.: Infrared thermography for condition monitoring–a review. Infrared Physics & Technology, 60:35–55, 2013.

24. Monica, P., Bavusi, M., Bernini, R., Bigagli, L., Bost, M., Bourquin, F., Cottineau, L.-M., Cuomo, V., Vecchia, P. D., Dolce, M., Dumoulin, J., Eppelbaum, L., Fornaro, G., Gustafsson, M., Hugenschmidt, J., Kaspersen, P., Kim, H., Lapenna, V., Leggio, M., Loperte, A., Mazzetti, P., Moroni, C., Nativi, S., Nordebo, S., Pacini, F., Palombo, A., Pascucci, S., Perrone, A., Pignatti, S., Ponzo, F. C., Rizzo, E., Soldovieri, F., and Taillade, F.: Transport infrastructure surveillance and monitoring by electromagnetic sensing: The ISTIMES project, deliverable 5.8. 10(12):10620–10639, 2010.

25. Kobayashi, K. and Banthia, N.: Corrosion detection in reinforced concrete using induction heating and infrared thermography. Journal of Civil Structural Health Monitoring, 1(1-2):25–35, 2011.

26. Solla, M., Caamaño, C., Riveiro, B., and Lorenzo, H.: GPR analysis of a masonry arch for structural assessment. In Advanced Ground Penetrating Radar (IWAGPR), 2011 6th International Workshop on, pages 1–6. IEEE, 2011.

27. Saarenketo, T. and Scullion, T.: Road evaluation with ground penetrating radar. Journal of Applied Geophysics, 43(2-4):119–138, 2000.

28. GSSI Geophysical Survey Systems Inc: What is GPR? `https://www.geophysical.com/whatisgpr`, 2018.

29. Hugenschmidt, J.: Concrete bridge inspection with a mobile GPR system. Construction and Building Materials, 16(3):147–154, 2002.

30. Wang, Y. M. and Chew, W. C.: An iterative solution of the two-dimensional electromagnetic inverse scattering problem. International Journal of Imaging Systems and Technology, 1(1):100–108, 1989.

31. Chew, W. C. and Wang, Y. M.: Reconstruction of two-dimensional permittivity distribution using the distorted Born iterative method. IEEE Transactions on Medical Imaging, 9(2):218–225, 1990.

32. Bojarski, N. N.: The k-space formulation of the scattering problem in the time domain. The Journal of the Acoustical Society of America, 72:570, 1982.

33. Bojarski, N. N.: A survey of the near-field far-field inverse scattering inverse source integral equation. IEEE Transactions on Antennas and Propagation, 30(5):975–979, 1982.

34. Devaney, A. J.: Inversion formula for inverse scattering within the Born approximation. Optics Letters, 7(3):111–112, 1982.

35. Langenberg, K.: Introduction to the special issue on inverse problems. Wave Motion, 11(2):99–112, 1989.

36. Wicks, M. C.: RF tomography with application to ground penetrating radars. In Proc. IEEE 41st Asilomar Conference ACSSC 2007, pages 2017–2022, Nov 2007.

37. Soumekh, M.: Synthetic aperture radar signal processing, volume 7. New York: Wiley, 1999.

38. Yamaguchi, Y., Sato, A., Boerner, W.-M., Sato, R., and Yamada, H.: Four-component scattering power decomposition with rotation of coherency matrix. IEEE Transactions on Geoscience and Remote Sensing, 49(6):2251–2258, 2011.

39. Singh, G., Yamaguchi, Y., Boerner, W.-M., and Park, S.-E.: Monitoring of the march 11, 2011, off-tohoku 9.0 earthquake with super-tsunami disaster by implementing fully polarimetric high-resolution polsar techniques. Proceedings of the IEEE, 101(3):831–846, 2013.

40. Leone, G., Brancaccio, A., and Pierri, R.: Linear and quadratic inverse scattering for angularly varying circular cylinders. Journal of the Optical Society of America A, 16(12):2887–2895, 1999.

41. Pierri, R., Soldovieri, F., Liseno, A., and De Blasio, F.: Dielectric profiles reconstruction via the quadratic approach in 2-d geometry from multifrequency and multifrequency/multiview data. IEEE Transactions on Geoscience and Remote Sensing, 40(12):2709–2718, Dec 2002.

42. Picco, V., Gennarelli, G., Negishi, T., Soldovieri, F., and Erricolo, D.: Experimental validation of the quadratic forward model for RF tomography. IEEE Geoscience and Remote Sensing Letters, 12(7):1461–1465, March 2015.

43. Negishi, T., Farzami, F., Picco, V., Erricolo, D., Gennarelli, G., Soldovieri, F., Monte, L. L., Wicks, M. C., and Ansari, F.: Detection and imaging of cracks in reinforced concrete structures using RF tomography: Quadratic forward model approach. In 2015 IEEE International Geoscience and Remote Sensing Symposium (IGARSS), pages 3552–3555, July 2015.

44. Picco, V., Gennarelli, G., Negishi, T., Soldovieri, F., and Erricolo, D.: A quadratic inverse model for RF tomography. In 8th International Workshop on Advanced Ground Penetrating Radar (IWAGPR 2015), pages 1–4, Florence, Italy, July 2015.

45. Lo Monte, L.: Radio Frequency Tomography For Underground Void Detection. Doctoral dissertation, 2009.

46. Lo Monte, L., Soldovieri, F., Erricolo, D., and Wicks, M. C.: Radio frequency tomography for below ground imaging and surveillance of targets under cover. In Effective Surveillance for Homeland Security: Balancing Technology and Social Issues, eds. F. Flammini, R. Setola, and G. Franceschetti. Taylor & Francis/CRC Press, 2013.

47. Lo Monte, L., Erricolo, D., and Inan, U. S.: Radio frequency tomography for tunnel detection: principles and inversion schemes. In American Geophysical Union Fall Meeting, San Francisco, CA, Dec. 15-19, 2008.

48. Lo Monte, L. and Erricolo, D.: Distributed RF tomography for voids detection. In 2008 Meeting of the Military Sensing Symposia Specialty Group on Battlespace Acoustic & Seismic Sensing, Magnetic & Electric Field Sensors, The Johns Hopkins University Applied Physics Laboratory, Laurel, MD, August 19-21, 2008.

49. Lo Monte, L., Hayvaci, H. T., and Erricolo, D.: Propagation Model for RF Geotomography. In XXIX General Assembly of the International Union of Radio Science, Chicago, IL, Aug. 7-17, 2008.

50. Lo Monte, L., Bagci, A. M., Erricolo, D., and Ansari, R.: Spatial Resolution in Tomographic Imaging with Diffracted Fields. In XXIX General Assembly of the International Union of Radio Science, Chicago, IL, Aug. 7-17, 2008.

51. Lo Monte, L. and Erricolo, D.: Receiving Antenna Design for Ground Penetrating Tomographic Imaging. In IEEE AP-S International Symposium on Antennas and Propagation and USNC/URSI National Radio Science Meeting, San Diego, CA, July 5-12, 2008.

52. Lo Monte, L., Erricolo, D., and Wicks, M. C.: Propagation Model and Receiver Design for RF Geotomography. In 2008 IEEE Radar Conference, Rome, Italy, May 26-30, 2008.

53. Lo Monte, L., Erricolo, D., Soldovieri, F., and C. Wicks, M.: Underground Imaging of Irregular Terrains Using RF Tomography. In The Third International Workshop on Computational Advances in Multi-Sensor Adaptive Processing, Aruba, Dutch Antilles, December 13-16, 2009.

54. Lo Monte, L., Erricolo, D., Ansari, R., Soldovieri, F., and Wicks, M. C.: Underground Imaging Using RF Tomography: The Effect of Lateral Waves. In International Conference on Electromagnetics in Advanced Applications ICEAA, Turin, Italy, Sept. 14-18, 2009.

55. Lo Monte, L., Erricolo, D., Picco, V., Soldovieri, F., and Wicks, M. C.: Distributed RF Tomography for Tunnel Detection: Suitable Inversion Schemes. In National Aerospace & Electronics Conference, Dayton, OH, July 21-23, 2009.

56. Lo Monte, L., Erricolo, D., Soldovieri, F., and Wicks, M. C.: Imaging of Underground Anomalies using RF Tomography and Lateral Waves. In IEEE International Geoscience & Remote Sensing Symposium, Cape Town, South Africa, July 12-17, 2009.

57. Lo Monte, L., Erricolo, D., Soldovieri, F., and Wicks, M. C.: RF Tomography for Underground Target Detection in a Lossy and Cluttered Environment. In IEEE AP-S International Symposium on Antennas and Propagation and USNC/URSI National Radio Science Meeting, Charleston, SC, June 1-5, 2009.

58. Lo Monte, L., Ansari, R., Erricolo, D., and Wicks, M. C.: The Use of Geometric Diversity for Spectral Dominance in Underground Imaging. In Waveform Diversity Design

Conference, Orlando, FL, February 8-13, 2009.

59. Lo Monte, L., Erricolo, D., Soldovieri, F., and Wicks, M. C.: Radio frequency tomography for tunnel detection. IEEE Transaction on Geoscience and Remote Sensing, 48(3):1128–1137, Mar 2010.

60. Lo Monte, L., Erricolo, D., Soldovieri, F., and Wicks, M. C.: RF tomography for below-ground imaging of extended areas and close-in sensing. IEEE Geoscience and Remote Sensing Letters, 7(3):496–500, Jul 2010.

61. Picco, V., Erricolo, D., and Lo Monte, L.: Experimental validation of RF tomography. In International Union of Radio Science Commission B Electromagnetic Theory Symposium, Berlin, Germany, August 16-19, 2010.

62. Lo Monte, L., Erricolo, D., Soldovieri, F., and Wicks, M. C.: Recent advances in RF tomography for underground imaging. In XIII International Conference on Ground Penetrating Radar, Lecce, Italy, June 21-25, 2010.

63. Lo Monte, L., Picco, V., and Erricolo, D.: Image Formation in RF Tomography Using Compressive Sensing. In SIAM Conference on Imaging Science (IS10), Chicago, IL USA, Apr. 12-14 2010.

64. Lo Monte, L., Soldovieri, F., Erricolo, D., and Wicks, M. C.: Imaging below irregular terrain using RF tomography. IEEE Transaction on Geoscience and Remote Sensing, 50(9):3364–3373, Sep 2012.

65. Picco, V., Negishi, T., Stephens, M., Nishikata, S., and Erricolo, D.: Experiments for RF Tomography. In USNC-URSI National Radio Science Meeting, Boulder, CO, USA, Jan. 4-7 2012.

66. Nishikata, S., Picco, V., Negishi, T., and Erricolo, D.: Imaging of dielectric targets using RF Tomography. In IEEE International Symposium on Antennas and Propagation/USNC-URSI National Radio Science Meeting, Chicago, IL, USA, July 8-14 2012.

67. Negishi, T., Nishikata, S., Picco, V., and Erricolo, D.: Advantages of Polarization Diversity in Microwave Tomography. In IEEE International Symposium on Antennas and Propagation/USNC-URSI National Radio Science Meeting, Chicago, IL, USA, July 8-14 2012.

68. Picco, V., Negishi, T., Nishikata, S., and Erricolo, D.: Comparison of reconstruction algorithms for Microwave Tomography. In IEEE International Symposium on Antennas and Propagation/USNC-URSI National Radio Science Meeting, Chicago, IL, USA, July 8-14 2012.

69. Negishi, T., Picco, V., and Erricolo, D.: The use of the Algebraic Reconstruction Technique (ART) for imaging of dielectric targets in Radio Frequency Tomography. In IEEE International Conference on Wireless Information Technology and Systems, pages 1–4, Maui, HI, Nov. 11-16 2012.

70. Soldovieri, F., Lo Monte, L., and Erricolo, D.: Tunnel detection and localization via multi-monostatic rf tomography using magnetic sources. IET Radar, Sonar & Navigation, 6(9):834–845, December 2012.

71. Lo Monte, L., Soldovieri, F., Erricolo, D., Giannopoulos, A., and Wicks, M. C.: A comprehensive forward model for imaging under irregular terrain using rf tomography. International Journal of Antennas and Propagation, Special Issue on Propagation Models and Inversion Approaches for Subsurface and Through-Wall Imaging, 2012, 2012. doi:10.1155/2012/735414.

72. Negishi, T., Picco, V., and Erricolo, D.: Challenge on dielectric and metallic recognition for Radio Frequency Tomography. In USNC-URSI National Radio Science Meeting, Boulder, CO, USA, Jan. 9-12 2013.

73. Picco, V., Negishi, T., and Erricolo, D.: Resolution Analysis of a Radio Frequency Tomography System. In USNC-URSI National Radio Science Meeting, Boulder, CO, USA, Jan. 9-12 2013.

74. Negishi, T., Picco, V., Nishikata, S., and Erricolo, D.: Numerical Green's Function for Radio Frequency Tomography with Complex Geometry (invited). In URSI Commission B International Symposium on Electromagnetic Theory, Hiroshima, Japan, May 20-24 2013.

75. Negishi, T., Picco, V., Spitzer, D., Erricolo, D., and Lo Monte, L.: Imaging Behind Obstacles Using Only Diffracted Fields. In IEEE Antennas and Propagation Society International Symposium/USNC-URSI National Radio Science Meeting, Orlando, FL, USA, July 9-13 2013.

76. Picco, V., Negishi, T., Nishikata, S., and Erricolo, D.: RF Tomography in Free Space: Experimental Validation of the Forward Model and of a Conjugate Gradient In-

version Algorithm. In International Conference on Electromagnetics in Advanced Applications, ICEAA, Torino, Italy, September 9-13 2013.

77. Picco, V., Negishi, T., Nishikata, S., Spitzer, D., and Erricolo, D.: RF Tomography in Free Space: Experimental Validation of the Forward Model and an Inversion Algorithm Based on the Algebraic Reconstruction Technique. International Journal of Antennas and Propagation, 2013. Article ID 528347, doi:10.1155/2013/528347.

78. Picco, V., Soldovieri, F., Negishi, T., and Erricolo, D.: Quadratic Forward Model for RF Tomography: preliminary Results. In USNC-URSI National Radio Science Meeting, Boulder, CO, Jan. 8-11 2014.

79. Negishi, T., Picco, V., Spitzer, D., and Erricolo, D.: Buried Objects and Void Detection Using RF Tomography. In USNC-URSI National Radio Science Meeting, Boulder, CO, Jan. 8-11 2014.

80. Negishi, T., Picco, V., Lo Monte, L., and Erricolo, D.: Anisotropic model for RF Tomography. In IEEE Antennas and Propagation Society International Symposium/USNC-URSI National Radio Science Meeting, Memphis, TN, USA, July 6-11 2014.

81. Picco, V., Gennarelli, G., Negishi, T., Erricolo, D., and Soldovieri, F.: RF Tomography Under the Quadratic Approximation. In IEEE Antennas and Propagation Society International Symposium/USNC-URSI National Radio Science Meeting, Memphis, TN, USA, July 6-11 2014.

82. Almutiry, M., Wicks, M. C., Negishi, T., Erricolo, D., and Lo Monte, L.: Exploitation of dominant scatterers for sidelobe suppression in radar tomography. In Signal Processing Symposium, pages 1 – 4, Debe, Poland, June 2015.

83. Nassib, A., Negishi, T., Erricolo, D., Lo Monte, L., and Wicks, M. C.: A dyadic target model for multistatic sar/isar imaging. In 2015 IEEE International Radar Conference, pages 1509 – 1514, Arlington, VA, May 2015.

84. Negishi, T., Picco, V., Lo Monte, L., and Erricolo, D.: Dyadic contrast function for the forward model of diffraction tomography of thin cylindrical objects. IEEE Antennas and Wireless Propagation Letters, 16:991– 94, October 2016.

85. Negishi, T., Gennarelli, G., Soldovieri, F., and Erricolo, D.: Radio frequency tomography for the investigation of cracks in reinforced concrete structures. In European Geosciences Union General Assembly, page 1, Vienna, Austria, April 2016.

86. Negishi, T., Gennarelli, G., Liu, Y., Erricolo, D., and Soldovieri, F.: Imaging performance comparison in reinforced concrete pillars using ground penetrating radar and radio frequency tomography. In USNC-URSI National Radio Science Meeting, Boulder, CO, Jan. 4-7 2017.

87. Liu, Y., Negishi, T., and Erricolo, D.: Radio frequency tomography for a reinforced concrete cylinder by genetic algorithm. In IEEE Antennas and Propagation Society International Symposium/USNC-URSI National Radio Science Meeting, Boston, MA, July 8-13 2018.

88. Chew, W. C.: Waves and fields in inhomogeneous media. IEEE Press, 1995.

89. Balanis, C.: Advanced Engineering Electromagnetics. CourseSmart Series. Wiley, 2012.

90. Richmond, J.: Scattering by a dielectric cylinder of arbitrary cross section shape. IEEE Transactions on Antennas and Propagation, 13(3):334–341, 1965.

91. Hayes, M. H.: Statistical digital signal processing and modeling. John Wiley & Sons, 1996.

92. Hansen, P. C.: The truncated svd as a method for regularization. BIT Numerical Mathematics, 27(4):534–553, Dec 1987.

93. Hansen, P. C.: Analysis of discrete ill-posed problems by means of the l-curve. SIAM review, 34(4):561–580, 1992.

94. Mitra, S. K. and Kuo, Y.: Digital signal processing: a computer-based approach, volume 2. McGraw-Hill Higher Education New York, 2006.

95. Hansen, P.: Regularization tools version 4.0 for matlab 7.3. Numerical Algorithms, 46:189–194, 2007.

96. Shewchuk, J. R.: An introduction to the conjugate gradient method without the agonizing pain, 1994.

97. Haykin, S. S.: Adaptive filter theory. Pearson Education India, 2008.

98. Daniel, J. W., Gragg, W. B., Kaufman, L., and Stewart, G.: Reorthogonalization and stable algorithms for updating the gram-schmidt qr factorization. Mathematics of Computation, 30(136):772–795, 1976.

99. Kaczmarz, S.: Angenaherte auflosung von systemen linearer gleichungen. Bulletin International de l'Academie Polonaise des Sciences et des Lettres, 35:355–357, 1937. http://jasonstockmann.com/Jason_Stockmann/Welcome_files/kaczmarz_english_translation_1937.pdf.

100. Uslenghi, P.: Electromagnetic Scattering. New York: Academic Press, 1978.

101. Harrington, R.: Time-Harmonic Electromagnetic Fields. IEEE Press Series on Electromagnetic Wave Theory. Wiley, 2001.

102. Kak, A. C. and Slaney, M.: Principles of computerized tomographic imaging. Society for Industrial and Applied Mathematics, 2001.

103. Altair Engineering, Inc.: Feko - em simulation software. https://www.feko.info/. updated: 01-11-2011.

104. Natinal Instruments: What is LabVIEW? http://www.ni.com/en-us/shop/labview.html.

VITA

NAME: Tadahiro Negishi

EDUCATION:
B.S, Electrical and Electronics Engineering
Nippon Institute of Technology, Japan, 2003 – 2007

M.S., Electrical and Computer Engineering
University of Illinois at Chicago, 2009 – 2011

Ph.D., Electrical and Computer Engineering
University of Illinois at Chicago, 2011 – 2018

EXPERIENCE:
Summer Intern, Mitsubishi Electric Corporation
Kamakura, Japan, 06/2015 – 07/2015

Summer & Fall Intern, ANSYS
Evanston, IL, 05/2017 – 12/2017

Research and Teaching Assistant
Department of Electrical and Computer Engineering
University of Illinois at Chicago, IL, 08/2011 – 05/2017

AWARDS:
The National Academies Travel Fellowship, 2013 – 2014
Travel fellowship to support conference attendance

PUBLICATIONS:
D. Erricolo, T. Negishi, "Symmetry properties of spheroidal functions with respect to their parameter," IEEE Transactions on Antenna and Propagation, Vol. 65, Issue 9, Sept. 2017, pp. 4947 - 4951.

T. Negishi, V. Picco, L. Lo Monte and D. Erricolo, "Dyadic contrast function for the forward model of diffraction tomography of thin cylindrical objects," IEEE Antennas and Wireless Propagation Letters, Vol. 16, Oct. 2016, pp. 991 - 994.

T. Negishi, D. Erricolo, P.L.E. Uslenghi, "Metamaterial spheroidal cavity to enhance dipole radiation," IEEE Transactions on Antenna and Propagation, Vol. 63, Issue 6, June 2015, pp. 2802 - 2807.

V. Picco, G. Gennarelli, **T. Negishi**, F. Soldovieri, D. Erricolo, "Experimental Validation of the Quadratic Forward Model for RF Tomography," IEEE Geoscience and Remote Sensing Letters, Vol. 12, No. 7, March 2015, pp. 1461 - 1465.

T. Negishi, V. Picco, D. Spitzer, D. Erricolo, G. Carluccio, F. Puggelli, M. Albani," Measurements to Validate the UTD Triple Diffraction Coefficient," IEEE Transactions on Antenna and Propagation, vol. 62, Issue 7, pp. 3723 - 3730, July 2014, DOI: 10.1109/TAP.2014.2318334

P. Setlur, **T. Negishi**, N. Devroye, D. Erricolo, "Multipath Exploitation in Non-LOS Urban Synthetic Aperture Radar," IEEE Journal of Selected Topics in Signal Processing, Special Issue on Non-cooperative Localization Networks, Vol. 8, No. 1, pp. 137 - 152, Feb. 2014, doi 10.1109/JSTSP.2013.2287185

V. Picco, **T. Negishi**, S. Nishikata, D. Spitzer, and D. Erricolo, "RF Tomography in Free Space: Experimental Validation of the Forward Model and an Inversion Algorithm Based on the Algebraic Reconstruction Technique," International Journal of Antennas and Propagation, vol. 2013, Article ID 528347, 9 pages, 2013. doi:10.1155/2013/528347

S. Theerawisitpong, T. Suzuki, **T. Negishi**, and Y. Watanabe, "Near-field transmission imaging by 60GHz band waveguide-type microscopic aperture probe," IEICE Transactions on Communications, Vol.E90-B, No.9, pp.2387 - 2393 Sept. 2007. ISSN: 09168516

T. Negishi, V. Picco, D. Erricolo, G. Gennarelli, F. Soldovieri and P. L.E Uslenghi, "Experimental Validation of Radio Frequency Tomography for an Inhomogeneous Medium" URSI Commission B International Symposium on Electromagnetic Theory, pp. 5 - 8, Espoo, Finland, August 14 - 18, 2016.

D. Erricolo, **T. Negishi**, P.L.E. Uslenghi, "Radiation from an Axial Electric Dipole with Oblate Spheroidal Metamaterial Cloak Cover," International Symposium on Antennas and Propagation (ISAP2015), pp. 1 - 4, Hobart, Tasmania, Australia, Nov. 9 - 12, 2015.

T. Negishi, D. Erricolo, P. L. E. Uslenghi, "Radiation from an Axial Electric Dipole with Prolate Spheroidal Metamaterial Cloak Cover," International Conference on Electromagnetics in Advanced Applications (ICEAA), pp. 403 - 406, Torino, Italy, Sept. 7 - 11, 2015.

T. Negishi, F. Farzami, V. Picco, D. Erricolo, G. Gennarelli, F. Soldovieri, L. Lo Monte, M. C. Wicks, F. Ansari, "Detection and imaging of cracks in reinforced concrete structures using RF Tomography: quadratic forward model approach," International Geoscience and Remote Sensing Symposium (IGARSS 2015), pp. 3552 - 3555, Milan, Italy, July 26 - 31, 2015.

V. Picco, G. Gennarelli, **T. Negishi**, F. Soldovieri, D. Erricolo, "A quadratic inverse model for RF Tomography," 8th International Workshop on Advanced Ground Penetrating Radar (IWAGPR 2015), pp. 1 - 4, Florence, Italy, July 7 - 10, 2015.

M. Almutiry, M. C. Wicks, **T. Negishi**, D. Erricolo, L. Lo Monte, "Exploitation of Dominant Scatterers for Sidelobe Suppression in Radar Tomography," Signal Processing Symposium, pp. 1 - 4, Debe, Poland, June 10 - 12, 2015.

A. Nassib, **T. Negishi**, D. Erricolo, L. Lo Monte, M. C. Wicks, "A Dyadic Target Model for Multistatic SAR/ISAR Imaging," 2015 IEEE International Radar Conference, pp. 1509 - 1514, Arlington, VA, May 11 - 15, 2015

T. Negishi, V. Picco, D. Spitzer, D. Erricolo, G. Carluccio, F. Puggelli, M. Albani, "Electromagnetic scattering measurements for the validation of the UTD triple diffraction coefficient in an imperfect anechoic environment: analysis of spurious ray contributions," 2014 IEEE International Conference on Antenna Measurements & Applications, pp. 1 - 4, Antibes Juan-les-Pins, France, Nov. 16 - 19, 2014.

V. Picco, **T. Negishi**, D. Erricolo, L. Lo Monte, "Dyadic Contrast Function for RF Tomography: Preliminary Results," 2014 IEEE International Conference on Antenna Measurements & Applications, pp. 1 - 4, Antibes Juan-les-Pins, France, Nov. 16 - 19, 2014.

P. L.E. Uslenghi, D. Erricolo, and **T. Negishi**, "Radiation by a Dipole Antenna on the Axis of a Semi-spheroidal Cavity Partially Filled with DNG Metamaterials," The International Workshop on Antenna Technology (iWAT), pp. 266 - 267, Sydney, Australia, Mar. 4 - 6 2014

V. Picco, **T. Negishi**, S. Nishikata, and D. Erricolo, "RF Tomography in Free Space: Experimental Validation of the Forward Model and of a Conjugate Gradient Inversion Algorithm," International Conference on Electromagnetics in Advanced Applications, pp.1361 - 1364, Torino, Italy, Spt. 9 - 13 2013

T. Negishi, V. Picco, S. Nishikata, and D. Erricolo, "Numerical Green's Function for Radio Frequency Tomography with Complex Geometry" URSI Commission B International Symposium on Electromagnetic Theory, pp. 1113 - 1116, Hiroshima, Japan, May 20 - 24 2013

T. Negishi, V. Picco, and D. Erricolo, "The use of the Algebraic Reconstruction Technique (ART) for imaging of dielectric targets in Radio Frequency Tomography," IEEE International Conference on Wireless Information Technology and Systems, pp.1 - 4, Maui, HI, Nov. 11 - 16 2012.

T. Suzuki, S. Theerawisitpong, **T. Negishi**, Y. Watanabe, and N. Morita, "Microscopic Structure Imaging with Phase Analysis at 60GHz band," International Conference on Infrared, Millimeter and THz Waves 2008, T2G5, pp.1 - 3, Pasadena, CA, Sept. 2008.

S. Theerawisitpong, T. Suzuki, **T. Negishi**, T. Shibahara, and Y. Watanabe, "Void and Pore Detections by the Scanning near-field millimeter-wave microscopy Aperture Probe," Asia-Pacific Microwave Conference 2007, pp. 1 - 4, Bangkok, Thailand, Dec. 2007.

S. Theerawisitpong, T. Suzuki, **T. Negishi**, T. Shibahara, and Y. Watanabe, "In-depth measurement of 60GHz band near-field and transmission mode microscopy," International Conference on Infrared, Millimeter and THz Waves 2007, TueA4-6, pp.362 - 363, Cardiff, UK, Sept. 2007.

T. Negishi, T. Suzuki, K. Mitsurugi, S. Theerawisitpong, and Y. Watanabe, "Imaging by V-band waveguide-type microscopic aperture probe," Institute of Electronics, Information and Communication Engineers-Space, Aeronautical and Navigational Electronics, pp. 55 - 60, Saitama, Japan, Feb. 2007.

T. Negishi, T. Suzuki, K. Mitsurugi, and Y. Watanabe, "Imaging by 60GHz Band Waveguide-Type Microscopic Aperture Probe," International Symposium on Antennas and Propagation 2006, Singapore, no.FC2, pp. 1 - 4, Nov. 2006

T. Suzuki, K. Sugimoto, Y. Yamagami, **T. Negishi** and Y. Watanabe," Local Dielectric Measurement by Waveguide-type Microscopic Aperture Probe" Progress in Electromagnetics Research Symposium 2006, pp. 13 - 14, Cambridge, USA, March 2006.

Y. Liu, **T. Negishi**, D. Erricolo, "Radio Frequency Tomography for a Reinforced Concrete Cylinder by Genetic Algorithm," IEEE Antennas and Propagation Society International Symposium/USNC-URSI National Radio Science Meeting, Boston, MA, July 8 - 13, 2018.

T. Negishi, G. Gennarelli, Y. Liu, D. Erricolo and F. Soldovieri, "Imaging performance comparison in reinforced concrete pillars using Ground Penetrating Radar and Radio Frequency Tomography," USNC-URSI National Radio Science Meeting, Boulder, CO, Jan. 4 - 6, 2017.

D. Erricolo, **T. Negishi**, G. Gennarelli and F. Soldovieri, "Effect of Green's function choice in Radio Frequency Tomography to investigate reinforced concrete structures," IEEE Antennas and Propagation Society International Symposium/USNC-URSI National Radio Science Meeting, Fajardo, Puerto Rico , June 26 - July 1, 2016.

T. Negishi, G. Gennarelli, F. Soldovieri, D. Erricolo, "Radio Frequency Tomography for the investigation of cracks in reinforced concrete structures," European Geosciences Union General Assembly, Vienna, Austria, April 17–22, 2016.

F. Farzami, **T. Negishi**, D. Erricolo, "Numerical results for the radiation by a dipole antenna on the axis of a circular hole in a metallic plane covered by DPS and DNG oblate spheroidal lenses," USNC-URSI National Radio Science Meeting, Boulder, CO, Jan. 6 - 9, 2016.

Y. Liu, **T. Negishi**, D. Erricolo, "Exact electromagnetic scattering from a dipole antenna located inside a multilayer metamaterial oblate spheroidal cavity" USNC-URSI National Radio Science Meeting, Boulder, CO, Jan. 6 - 9, 2016.

B. Feyissa, D. Erricolo, **T. Negishi**, "Numerical results for the radiation by a line source in the presence of a slotted metallic plane covered by DPS and DNG elliptical lenses," USNC-URSI National Radio Science Meeting, Boulder, CO, Jan. 6 - 9, 2016.

S. Ghurye, **T. Negishi**, D. Erricolo, "Exact scattering for a metallic spheroid at the interface between anti-isorefractive half-spaces," USNC-URSI National Radio Science Meeting, Boulder, CO, Jan. 6 - 9, 2016.

S. Khaledian, **T. Negishi**, D. Erricolo, "Exact scattering for an elliptic metal cylinder at the interface between antiisorefractive half-spaces," USNC-URSI National Radio Science Meeting, Boulder, CO, Jan. 6 - 9, 2016.

T. Negishi, F. Farzami, V. Picco, D. Erricolo, G. Gennarelli, F. Soldovieri, L. Lo Monte, M. C. Wicks, F. Ansari, "Evaluation of concrete structures using RF Tomography techniques," IEEE Antennas and Propagation Society International Symposium and North American Radio Science Meeting, Vancouver, British Columbia, Canada, July 19 - 25, 2015.

F. Soldovieri, G. Gennarelli, I. Catapano, D. Erricolo, V. Picco, **T. Negishi**, "A quadratic RF Tomography inverse model for reflection configuration," 1st URSI Atlantic Radio Science Conference (URSI AT-RASC), Gran Canaria, Spain, May 18 - 22, 2015.

V. Picco, G. Gennarelli, **T. Negishi**, D. Erricolo, and F. Soldovieri, "RF Tomography Under the Quadratic Approximation," IEEE International Symposium on Antennas and Propagation and USNC-URSI National Radio Science Meeting, Memphis, TN, July 6 - 11 2014

T. Negishi, V. Picco, L. Lo Monte, and D. Erricolo, "Anisotropic model for RF Tomography," IEEE International Symposium on Antennas and Propagation and USNC-URSI National Radio Science Meeting, Memphis, TN, July 6 - 11 2014

P. L.E. Uslenghi, D. Erricolo, and **T. Negishi**, "Radiation by a Dipole Antenna on the Axis of a Semi-spheroidal Cavity Partially Filled with DNG Metamaterials," The International Workshop on Antenna Technology (iWAT), pp. 266 - 267, Sydney, Australia, Mar. 4 - 6 2014

V. Picco, F. Soldovieri, **T. Negishi**, and D. Erricolo, "Quadratic Forward Model for RF Tomography: Preliminary Results," URSI National Radio Science Meeting, Boulder, CO, Jan. 8 - 11 2014

T. Negishi, V. Picco, D. Spitzer, and D. Erricolo "Buried objects and void detection using RF Tomography," URSI National Radio Science Meeting, Boulder, CO, Jan. 8 - 11 2014

V. Picco, **T. Negishi**, D. Spitzer, D. Erricolo, G. Carluccio, F. Puggelli, M. Albani, "Experimental Validation of the UTD Third Order Diffraction Coefficient," IEEE Antennas and Propagation Society International Symposium/USNC-URSI National Radio Science Meeting, Orlando, FL, USA, July 7 - 13, 2013.

T. Negishi, V. Picco, D. Spitzer, D. Erricolo, L. Lo Monte, "Imaging Behind Obstacles Using Only Diffracted Fields," IEEE Antennas and Propagation Society International Symposium/USNC-URSI National Radio Science Meeting, Orlando, FL, USA, July 7 - 13, 2013.

V. Picco, **T. Negishi**, and D. Erricolo, "Resolution Analysis of a Radio Frequency Tomography System," URSI National Radio Science Meeting, Boulder, CO, Jan. 9 - 12 2013

T. Negishi, V. Picco, and D. Erricolo, "Challenge on Dielectric and Metallic Targets Recognition for Radio Frequency Tomography," URSI National Radio Science Meeting, Boulder, CO, Jan. 9 - 12 2013

V. Picco, **T. Negishi**, S. Nishikata, and D. Erricolo, "Comparison of reconstruction algorithms for Microwave Tomography, with applications to experimental data," IEEE International Symposium on Antennas and Propagation and USNC-URSI National Radio Science Meeting, Chicago, IL, July 8 - 14 2012

T. Negishi, S. Nishikata, V. Picco, and D. Erricolo, "Advantages of Polarization Diversity in Microwave Tomography," IEEE International Symposium on Antennas and Propagation and USNC-URSI National Radio Science Meeting, Chicago, IL, July 8 - 14 2012

S. Nishikata, V. Picco, **T. Negishi**, and D. Erricolo, "Imaging of dielectric targets using RF Tomography," IEEE International Symposium on Antennas and Propagation and USNC-URSI National Radio Science Meeting, Chicago, IL, July 8 - 14 2012

V. Picco, **T. Negishi**, M. Stephens, S. Nishikata, and D. Erricolo, "Experiments for RF Tomography", URSI National Radio Science Meeting, Boulder, CO, Jan. 4 - 7 2012